Growth, structure and lattice dynamics of epitaxial europium oxide thin films

Zur Erlangung des akademischen Grades eines

DOKTORS DER NATURWISSENSCHAFTEN

von der Fakultät für Physik des

Karlsruher Instituts für Technologie (KIT)

genehmigte

DISSERTATION

von

Ramu Pradip
aus Mavelikara/Indien

Tag der Mündlichen Prüfung: 13.01.2017

Referent: Prof. Dr. rer. nat. T. Baumbach
Korreferent: Prof. Dr. rer. nat. W. Wulfhekel
zusätzlicher Referent: Dr. rer. nat. S. Stankov

Contents

List of figures

Chapter 1

Introduction

Lattice dynamics describes the vibrations of atoms about their equilibrium positions in a crystal lattice and its implications on the physical properties of a material. The atomic vibrations carry quantized energy and the portion of vibration is called a phonon. Phonons are quasiparticles that obey the Bose-Einstein statistics and are fully described by their material-specific phonon dispersion relations in the reciprocal space. Integrating the phonon dispersions over the momentum space results in the phonon density of states (DOS), or the phonon spectrum of a material. Many thermodynamic and elastic properties such as vibrational entropy, lattice specific heat, mean force constant, mean speed of sound and others can be precisely calculated from the phonon DOS. Apart from the most obvious role for the thermal transport (in semiconductors and insulators), via complex interactions with other particles and quasiparticles, phonons participate in many physical phenomena such as phase transitions [1], ferroelectricity [2], superconductivity [3], thermoelectricity [4] to name a few.

The lattice dynamics of nanoscale materials has attracted a lot of attention in the last decades due to the rapid progress of nanotechnology. The continuous downscaling of electronic circuits has enabled enormous integration levels. Presently a square centimeter of silicon chip contains approximately 1.5 billion transistors. Further downscaling needs to address new phenomena that are posed by the reduced dimensions. In the nanoscale regime, the physical properties of materials differ drastically from their bulk counterparts. In particular this applies for the thermal lattice excitations and has strong implications in the heat dissipation in nanodevices. Self-heating of devices occurs by the scattering of electrons from lattice vibrations. Without efficient thermal management the near-future devices will be short lived and energy inefficient. On the contrary, in the important field of thermoelectrics, which deals with converting heat into electricity, nanoscaling is an important approach to lower the thermal conductivity [5] by introducing grain boundaries and interfaces. The novel field of phonon nanoengineering that aims at controlling the thermal and sound transport via nanostructuring is already rapidly developing [6, 7, 8, 9,

10]. The ultimate goal is to design phononic devices, analogous to that of diodes and transistors in electronics, that will allow for a full control over the thermal and acoustic properties. Therefore, reaching a comprehensive understanding of the effects of nanostructuring on material's phonon dispersions and phonon DOS is a topic of general interest for nanotechnology. This calls for a systematic study of phonons and their modifications as a function of size, shape, epitaxial strain and chemical state.

A complete determination of the lattice dynamics of materials require measuring either the phonon dispersion relations or the phonon DOS. For large crystals, inelastic neutron scattering (INS) remains as a *status quo* for probing phonon dispersion relations. The advent of third generation synchrotron sources like ESRF-The European Synchrotron, APS and Spring-8 established inelastic x-ray scattering (IXS) as a primary technique for mapping phonon dispersions in small crystals. The advantage of IXS over INS is essentially the access to smaller scattering volumes, thereby making it applicable to thin films and nanostructures, or samples under extreme conditions, such as high pressures. Other methods like Brillioun and Raman scattering offer high energy resolution up to 10^{-8} eV, however, they probe only very small momentum transfers that are close to zero. Helium atoms scattering and electron energy loss spectroscopy are examples for phonon spectroscopy methods that are extremely surface sensitive. Another phonon spectroscopy technique is nuclear inelastic scattering (NIS) that is based on the Mössbauer effect and gives direct access to the partial phonon DOS of the Mössbauer-active element in the solid. While the high penetration depth of the x-rays ensures bulk sensitivity, the large crossection due to the resonant nature of the Mössbauer effect, makes this method applicable to extremely small amounts of material such as mono- and even sub-monolayers. Another unique feature of nuclear inelastic scattering, in comparison to other phonon spectroscopy methods, is that it is element and even isotope specific. Therefore, even if the target material is buried or sandwiched by other materials, only the Mössbauer-active isotope in the sample contributes, in a background-free fashion, to the measured signal.

This thesis focuses on a combined experimental and theoretical study of lattice dynamics of rare earth oxides, in particular europium monoxide and europium sesquioxide. These two compounds have the same constituent elements, namely europium and oxygen that are differently arranged and chemically bonded, consequently, imparting contrasting physical properties. Therefore, the comparison of lattice dynamics of these two materials is expected to shed light on how chemical coordination, stoichiometry, and crystal structure influence thermodynamic and elastic properties of europium oxides. EuO is a rare semiconducting ferromagnet with a Curie temperature of 69 K and is considered as a model system for Heisenberg ferromagnets [11]. Initially known for its giant magneto-optic Kerr [12] and

Faraday [13] effects, this fascinating oxide reveals a rich variety of other physical phenomena, such as metal-to-insulator transition with colossal magnetoresistance under doping [14, 15], strain-induced manipulation of T_C [16], and anomalous Hall effect [17]. Presently, it is one of the favoured candidates for the application as a spin filter in future spintronic devices due to the large exchange splitting of its conduction band [18]. Indeed, EuO based tunnel junctions have already demonstrated very high spin polarization efficiency, that along with the recent integration on Si, classified EuO as a potential workhorse in the Si-based spintronics [19]. However, the lattice dynamics of EuO remained unknown except for few early Raman scattering experiments [20, 21, 22]. Despite that these early Raman scattering experiments suggested the presence of temperature-dependent coupling between lattice vibrations and spin waves, a comprehensive understanding of the strength and nature of this phenomenon, that is important for the proposed application of EuO, has not been provided.

Eu_2O_3 belongs to the technologically important family of rare earth sesquioxides RE_2O_3 that have been considered as gate materials for nanotransistors due to their very high dielectric constants. SiO_2 is the dielectric material of choice for complementary metal oxide semiconductor technology down to 0.1 μm. Below this threshold a drastic reduction of insulating properties of SiO_2 are observed. The replacement candidates are metal oxides, perovskite type metal oxides, and rare earth oxides. However, a large fraction of these metal oxides are unstable on Si. Currently Hf oxide based alloy that exhibits a lower dielectric value compared to RE_2O_3 is used as substitute. Several RE_2O_3, including Eu_2O_3, show small lattice mismatch and augmented thermodynamic stability on Si and other semiconductors such as GaAs and Ge that promotes them as prospective materials for ultrathin CMOS technology [23]. In addition to the questions related to heat dissipation, recent studies have demonstrated the role that phonons of the dielectric layer play on transport properties of a semiconductor via 'remote phonon scattering' [24]. All these make lattice dynamics investigations in thin and ultrathin rare earth oxide films very important and timely.

The thesis is based on a comprehensive experimental and theoretical investigation of thickness- and temperature-dependence of lattice dynamics of epitaxial EuO films, and of bulk Eu_2O_3. The lattice dynamics of EuO is experimentally determined by a combination of nuclear inelastic scattering and inelastic x-ray scattering in a temperature range between 30 K and 300 K using a 100 nm thick EuO(0 0 1) film grown on ytrria-stabilised zirconia YSZ(0 0 1) and capped with niobium protective layer. The capping layer protects the reactive EuO film from further oxidation and mimics the proposed spin-filter device architecture. The thickness-dependent lattice dynamics investigation was performed using *in situ* nuclear inelastic scattering on EuO(0 0 1) ultrathin films of thickness 1, 2 and 45 MLs (a monolayer ML = 1.71 Å)

grown on yttrium aluminate YAO(1 1 0). The samples were prepared by molecular beam epitaxy and precisely characterised both chemically and structurally to ensure perfect stoichiometry, single crystalinity and phase purity. The lattice dynamics of Eu_2O_3 was experimentally determined by nuclear inelastic scattering on a commercially available Eu_2O_3 powder shaped into a pellet. The experimental results are compared to the *ab initio* calculations performed by a collaboration partner. Such benchmarking of advanced *ab initio* methods by experimental results advances the field of computational modelling of solids.

The thesis is organised as follows: After a general introduction given in the first chapter, in the second chapter the theoretical background on lattice dynamics, experimental techniques for sample preparation, characterization, and lattice dynamics study are presented. The third chapter gives an overview of the crystal structure, physical properties and applications of the investigated europium oxides, namely EuO and Eu_2O_3. Chapters 4 and 5 deal with the lattice dynamics of bulk-like and ultrathin EuO films, respectively, while the lattice dynamics of Eu_2O_3 is presented in chapter 6. Each of these chapters gives a detailed description of the sample preparation and characterisation, theoretical and experimental determination of lattice dynamics, thermodynamic and elastic properties and their comparison. The conclusions are presented in chapter 7. The Matlab codes used for the data analysis are listed in the appendix.

All lattice dynamics calculations presented in this thesis were performed by Dr. hab. Przemysław Piekarz and Dr. hab. Małgorzata Sternik from the Institute of Nuclear Physics, Polish Academy of Sciences, Krakow, Poland.

Chapter 2

Theoretical background and experimental techniques

The aim of this chapter is to give an overview of the theoretical aspects of lattice dynamics as well as the experimental methods used in this thesis. The chapter begins by giving an introduction to the concepts of lattice dynamics such as phonons, phonon dispersion relations and phonon density of states. In the second part, the experimental techniques used for the preparation, and structural and chemical characterization of the samples are discussed. This is followed by a detailed description of x-ray scattering techniques such as nuclear inelastic scattering and inelastic x-ray scattering that were extensively used in this thesis.

2.1 Lattice dynamics

The history of lattice dynamics begins in the early 20th century with the conformation of Einstein's theory of Brownian motion that confirmed that atoms exist. In a short time from then, the temperature dependence of the heat capacity of solids was explained by the concept of quantisation of atomic vibrations. However, the vibrations were considered simple and treated with a single average frequency until (Einstein's model) 1912 when Born and von Karman introduced the modern model of lattice dynamics. In similar time period Debye and Waller had shown the effect of atomic vibrations on intensity of Bragg reflections in x-ray diffractograms. The field remained to a certain extent inactive primarily due to lack of experiments until the introduction of triple axis spectrometer in the 60s. Since then the field had remained exciting with constant development of powerful computational infrastructure as well as neutron sources and new generation synchrotron x-ray sources dedicated to theoretical and experimental lattice dynamics studies.

The focus of lattice dynamics is to describe the vibration of atoms about their equilibrium positions in the crystal lattice. Understanding the lattice dynamics has

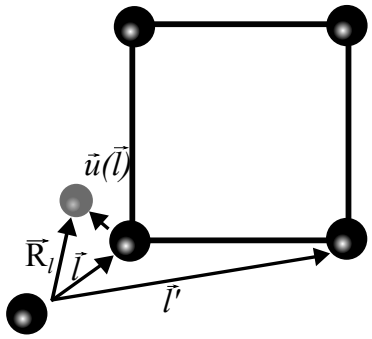

Figure 2.1: The displacement of l^{th} atom from its equilibrium position by $\vec{u}(\vec{l})$.

many important applications. In particular, the propagation of heat and sound in materials is a subject of great interest for micro and nanotechnology. The interaction of atomic vibrations with other quasi particles such as magnons, plasmons and electron-holes is known to bring about unique thermal and electronic characteristics. Lattice dynamics also plays an important role in phase transitions and many thermodynamic and elastic properties of materials.

The lattice dynamics is essentially a many body problem considering the nucleus and the electron cloud around it placed in an energetically favoured fashion. The adiabatic or Born-Oppenheimer theorem can be safely assumed in a generic case as the nucleus is approximately at least 10^3 times heavier than the electron cloud, essentially making it easy to decouple the electronic and nuclear motions.

The properties of the crystal can be derived from the solution for the Schrödinger equation:

$$\mathcal{H}\Psi(\vec{r},\vec{R}) = \epsilon\Psi(\vec{r},\vec{R}), \tag{2.1}$$

where $\vec{r}$ and $\vec{R}$ represent the coordinates of valence electrons and nuclei, respectively. Using the adiabatic approximation and neglecting the electron-nucleus interaction term, the total wave function can be expressed as:

$$\Psi(\vec{r},\vec{R}) = \psi(\vec{r},\vec{R})\chi(\vec{R}), \tag{2.2}$$

where ψ and χ are the wave functions for the entire system of electrons and nucleus, respectively. The Schrödinger equation for $\chi(\vec{R})$, that determines the lattice dynamics of the solid is given by the expression:

$$\left(\sum \frac{-\hbar^2}{2M_l}\nabla^2_{R_l} + V(\vec{R})\right)\chi(\vec{R}) = \epsilon\chi(\vec{R}), \tag{2.3}$$

$$V(\vec{R}) = V_{nn}(\vec{R}) + E_e(\vec{R}), \tag{2.4}$$

where M_l is the mass of the nucleus described by the position vector $\vec{l}$, ∇^2 is the Laplace operator, $V(\vec{R})$ is the effective potential consisting of the interatomic potential V_{nn} and the electron eigenvalue E_e.

Due to thermal motion, the atoms move away from their equilibrium positions and restoring forces proportional to the amplitude of their displacements act on the displaced atoms. Since we are interested in small displacements relative to the interatomic distances, the method of small oscillations could be applied. Let $\vec{l} = l_1\hat{a_1}+l_2\hat{a_2}+l_3\hat{a_3}$ be the equilibrium position of an atom in a Bravais lattice where $\hat{a_1}$, $\hat{a_2}$, $\hat{a_3}$ are the primitive lattice vectors and l_1, l_2, l_3 are integers. Suppose that the l^{th} atom deviates from the equilibrium position by $\vec{u}(\vec{l})$ and it is now described by the position vector $\vec{R_l} = \vec{l} + \vec{u}(\vec{l})$, see figure 2.1. The total kinetic energy T of the crystal is:

$$T = \frac{1}{2}\sum_{\alpha,l} M\dot{\vec{u}}^2_\alpha(\vec{l}), \tag{2.5}$$

where $\vec{\alpha} = x, y, z$. Since $V(R)$ is a function of atomic positions, the small atomic displacement $\vec{u_\alpha}(\vec{l})$ changes the effective potential and can be expressed as Taylor series:

$$V = V_0 + \sum \Phi_\alpha(\vec{l})\vec{u}_\alpha(\vec{l}) + \frac{1}{2}\sum_{\alpha,l}\sum_{\beta,l'} \Phi_{\alpha,\beta}(\vec{l},\vec{l'})\vec{u}_\alpha(\vec{l})\vec{u}_\beta(\vec{l'}) + ... \tag{2.6}$$

where,

$$\Phi_\alpha(\vec{l}) = \frac{\partial V}{\partial \vec{u}_\alpha(\vec{l})}\Big|_0 \qquad\qquad \Phi_{\alpha,\beta}(\vec{l},\vec{l'}) = \frac{\partial^2 V}{\partial \vec{u}_\alpha(\vec{l})\partial \vec{u}_\beta(\vec{l'})}\Big|_0. \tag{2.7}$$

When the atom is at equilibrium, the potential energy is chosen to be zero, i.e., V_0=0, the net forces acting are also zero ($\Phi_\alpha(l,l') = 0$). Assuming harmonic approximation in this small oscillation regime allows to neglect second and higher order terms. Thus the vibrational Hamiltonian and net forces become:

$$\mathcal{H} = \frac{1}{2}\sum_{\alpha,l} M\dot{\vec{u}}^2_\alpha(\vec{l}) + \frac{1}{2}\sum_{\alpha,l}\sum_{\beta,l'} \Phi_{\alpha,\beta}(\vec{l},\vec{l'})\vec{u}_\alpha(\vec{l})\vec{u}_\beta(\vec{l'}) \tag{2.8}$$

$$F_\alpha(\vec{l}) = -\frac{\partial V}{\partial \vec{u}_\alpha(\vec{l})} = -\sum_{\beta,l'} \Phi_{\alpha\beta}(\vec{l},\vec{l'})\vec{u}_\beta(\vec{l'}). \tag{2.9}$$

This implies that the net force on an atom $\vec{l}$ is a linear function of displacement $\vec{u_\beta}(\vec{l'})$ and coefficients $\Phi_{\alpha\beta}(\vec{l},\vec{l'})$ are the atomic force constants. Consequently, the equation of motion for the l^{th} atom in the direction $\vec{\alpha}(x, y, z)$ becomes:

$$M\ddot{\vec{u}}_\alpha = -\sum_{\beta,l'} \Phi_{\alpha\beta}(\vec{l},\vec{l'})\vec{u_\beta}(\vec{l'}). \tag{2.10}$$

The potential energy term contains a cross product of atomic displacements, resulting in coupled equations of motion, making it difficult to solve. A solution of the equation of motion can be obtained by converting the Cartesian coordinates into a new coordinate system called the *normal* coordinates, where the equation of motion becomes decoupled. A *normal* mode vibration is a collective vibration of all atoms that forms a lattice wave. Upon solving, the general expression for the displacement of atoms can be written as [25]:

$$u_\alpha(\vec{l}) = \frac{1}{\sqrt{NM}} \sum_{j,\vec{k}_j} A(\vec{k}_j) e_\alpha(\vec{k}_j) e^{i[\vec{k}\vec{l} - \omega_j(\vec{k})t]}, \tag{2.11}$$

where N is the number of atoms, M is the mass, $A(\vec{k}_j)$ is the amplitude of vibration depending on the average energy of mode $\vec{k}_j$. The lattice wave in a crystal displaces the neighbouring atoms, that differ by a phase factor $\vec{k}.\vec{l}$.

Phonons

Phonons are non-localised quasi-particles. Atoms are the real particles that vibrate in a crystal lattice while the energy quanta of their collective motion is described by the phonons. A phonon in a crystal does possess a momentum, when it interacts with other particles such as photons, it behaves as if it had a momentum equal to $\hbar\vec{k}$. Phonons are bosons i.e. they are identical particles with integer spin. The amplitude of atomic vibration is directly proportional to the temperature. At higher temperatures, the amplitude of the lattice waves is bigger, therefore the average energy and number of phonons increase. At thermal equilibrium, the average phonon number $< n(\vec{k}_j) >$ is given by the Bose-Einstein statistics. The average phonon energy for a mode $\vec{k}_j$ is:

$$< E(\omega_j(\vec{k}), T) >= \left(< n(\vec{k}_j) > + \frac{1}{2} \right) \hbar\omega_j(\vec{k}). \tag{2.12}$$

The total energy can be calculated by summing the above for all the vibrational modes:

$$< E(T) >= \sum_{\vec{k},j} < E(\omega_j(\vec{k}), T) >= \sum_{\vec{k},j} \frac{\hbar\omega_j(\vec{k})}{exp[\hbar\omega_j(\vec{k})k_B T] - 1} + \frac{1}{2} \sum_{\vec{k},j} \hbar\omega_j(\vec{k}). \tag{2.13}$$

The second term in the equation 2.13 is temperature independent and refers to the zero point energy of the system at $T = 0\,\mathrm{K}$.

2.1.1 Phonon dispersion relations

The relationship between the phonon frequency ω and the wave vector $\vec{k}$ is called phonon dispersion relation. These relations can be directly obtained as a solution of the Schrödinger wave equation given in equation 2.1. For simpler systems it can be also obtained using a semiclassical approach assuming atoms as point masses that are connected by springs that obey Hooke's law. For example, figure 2.2 shows the calculated dispersion relations for one dimensional diatomic chain with a lattice parameter a consisting of atoms with masses M_1 and M_2. For every $\vec{k}$ there are 2 values of ω and $2N$ waves in total. The upper branch is called optic branch and the lower branch is called acoustic branch.

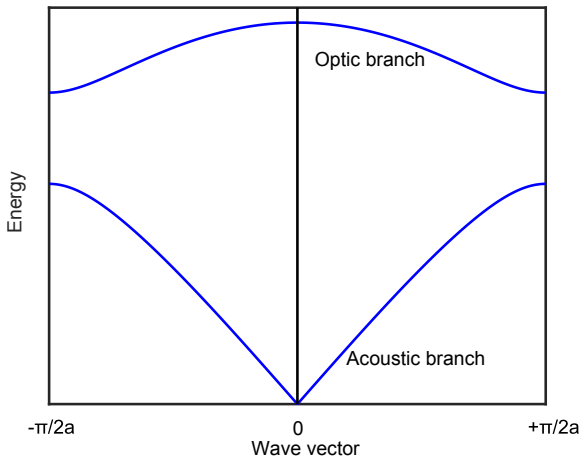

Figure 2.2: The phonon dispersion curves of 1D diatomic chain in the first Brillouin zone.

2.1.2 Phonon density of states

When the dispersion relations $\omega_j(\vec{k})$ for all momentum $(\vec{k})$ in the first Brillioun zone are known, the phonon density of states (DOS) can be calculated as:

$$g(\omega) = \frac{1}{3N} \sum_{j}^{3} \sum_{\vec{k}}^{N} \delta(\omega - \omega_j(\vec{k})). \tag{2.14}$$

Phonon DOS of one dimensional diatomic chain obtained by integrating the phonon dispersions over the frequency scale. The phonon DOS can be approximated by two simple models, namely the Einstein and the Debye models. However, these models were unable to explain experimental results for complex crystals. The state of the art technique to calculate the dispersion relations and the phonon DOS is the first principles calculations.

2.1.3 Thermodynamic and elastic properties

The partition function describes the statistical properties of a system at thermodynamic equilibrium. Most of the thermodynamic variables of the system, such as total energy, free energy, and entropy can be expressed in terms of the partition function, or its derivatives. The phonon modes are independent harmonic oscillators in the quasi-harmonic approximation. The partition function Z for a single harmonic oscillator of frequency $\omega_i = E_i/\hbar$ is [26]:

$$Z_i = \sum_{n}^{\infty} e^{-\beta(n+1/2)E_i} = \frac{e^{-\beta E_i/2}}{1 - e^{-\beta E_i}}. \tag{2.15}$$

where $\beta \equiv 1/(k_B T)$. Therefore, the partition function for a harmonic solid with N atoms and $3N$ independent oscillators is a product of individual oscillator partition functions:

$$Z_n = \prod_i^{3N} \frac{e^{-\beta E_i/2}}{1 - e^{-\beta E_i}}. \tag{2.16}$$

The equation 2.16 can be expressed in terms of the phonon density of states $g(E)$. For a 3D solid, $3Ng(E)dE$ phonon modes are available in an energy interval dE:

$$lnZ_n = -3N \int ln\left(2sinh\frac{\beta E}{2}\right) g(E)dE. \tag{2.17}$$

The **vibrational internal energy** of an atom is given by [26]:

$$U = -\frac{\partial lnZ}{\partial \beta} = \frac{3}{2}\int Ecoth\frac{\beta E}{2} g(E)dE \tag{2.18}$$

The **Helmholtz free energy** per atom is defined as $F_{vib} = -\frac{lnZ}{\beta}$:

$$F_{vib} = 3k_BT \int ln\left(2sinh\frac{\beta E}{2}\right) g(E)dE. \tag{2.19}$$

Vibrational entropy: It is well known that vibrational entropy S_{vib} of material influences the relative stability of its ordered and disordered states [27]. This indicates its importance in thermodynamics of solid state phase transitions [28], diffusion on surfaces [29], stability of nanocrystalline materials and others. It can be expressed in terms of the Helmholtz free energy:

$$S_{vib} = \frac{\partial F_{vib}}{\partial T} = k_B\beta U + ln(Z). \tag{2.20}$$

Lattice specific heat: Specific heat of a material is the amount of energy required to raise its temperature by one degree Celsius. It has mainly two components, one from the lattice vibrations and one from the thermal motion of the electrons. From the phonon DOS it is possible to estimate the former component. In case of insulators and semiconductors, the lattice component dominates the total heat capacity. Understanding the modification of the heat capacity in nanostructures compared to the bulk counterparts is extremely important for optimizing thermal management of nanoelectronic devices and thermoelectric devices [30, 31].

The lattice specific heat C_V of a solid at constant volume can be expressed as [32]:

$$C_V = \left(\frac{\partial U}{\partial T}\right)_V. \tag{2.21}$$

Using equation 2.18, one gets the expression:

$$C_V = 3k_B \int \left(\frac{\beta E}{2sinh(\beta E/2)}\right)^2 g(E)dE. \tag{2.22}$$

Speed of sound: The speed of sound is given by the slope of the acoustic phonon dispersion curves. At small wave vectors (long wavelengths) most solids are

well approximated by the Debye model, where the phonon dispersion is linear and the corresponding phonon DOS is quadratic in energy. The speed of sound v_s is independent of the energy of the phonon mode and is given by [33]:

$$\lim_{E\to 0} \frac{g(E)}{E^2} = \frac{m_R}{2\pi^2\hbar^3\rho v_s}, \tag{2.23}$$

where, m_R is the mass of the nuclei and ρ is the mass density. However the Debye approximation fails at higher energies due to the microscopic details of the lattice. The **thermal conductivity** of insulators and semiconductors is dominated by the acoustic phonon transport [34]. Therefore, the thermal conductivity k in a Debye solid can be estimated from the speed of sound v_s using the relation [32]:

$$k = \frac{1}{3} C \lambda_p v_s, \tag{2.24}$$

where C is the heat capacity per unit volume and λ_p is the phonon mean free path.

The **mean force constant** can be calculated from the phonon DOS using the following expression [35]:

$$K = \frac{1}{4} \int g(E) E \frac{e^{\beta E}+1}{e^{\beta E}-1} dE. \tag{2.25}$$

It is independent on temperature and weighted more to the higher phonon energies. In the harmonic approximation, the mean force constant can be also derived as a second derivative of the lattice potential [36].

2.1.4 First principles calculations

The first principles (*ab initio*) calculations based on density functional theory (DFT) has been found to be a promising tool for studying the structural and dynamical properties of real materials. This sophisticated theoretical approach needs only input information on the material such as atomic mass/number of constituent atoms and their arrangement in the crystal.

The physical properties of N interacting electrons in a lattice can be obtained by solving a set of Schrödinger equations:

$$\mathcal{H}\Psi = [T_e + V_{ee} + V]\Psi = E\Psi, \tag{2.26}$$

where T_e is the kinetic energy, V_{ee} is the electron-electron interaction energy, V is the external potential operator corresponding to the nucleus-nucleus interaction and nucleus-electron interaction, and Ψ is the wave function of N electrons. However, it is very difficult to analytically solve this Schrödinger equation with N electron wave functions, which is a complex function with $3N$ electron coordinates. To circumvent this problem DFT [37] utilizes the electron charge density to describe the multiple electron interactions. The DFT proves that an external potential $v(\vec{r})$ corresponding

to the operator V is a unique functional of the electron density $\rho(\vec{r})$, consequently the total energy E is also a unique functional of $\rho(\vec{r})$. That is, the electron density uniquely determines the potential acting on the electrons and vice versa. The ground state energy of the system is given by:

$$E[\rho(\vec{r})] = \langle \Psi_0 | \left(T_e + V_{ee} + V\right) | \Psi_0 \rangle = F[\rho(\vec{r})] + V[\rho(\vec{r})] \tag{2.27}$$

$$V[\rho(\vec{r})] = \langle \Psi_0 | V | \Psi_0 \rangle = \int V(\vec{r})\rho(\vec{r})d\vec{r}, \tag{2.28}$$

where Ψ_0 is the electron wave function in the ground state. The first two terms (T_e and V_{ee}) of equation (2.27) describe the kinetic energy and electron interactions, respectively. They are not system specific and their expectation value is expressed as a universal functional F of $\rho(\vec{r})$. On the other hand the external potential operator is system specific and is expressed as a unique functional V of $\rho(\vec{r})$.

In order to find the ground state energy, DFT uses the variational principle. The density ρ_0 that minimizes the total energy of the system is taken as the ground state density. To continue the calculations some assumptions are made to obtain the functionals that are mentioned in equation (2.27). The kinetic energy $T_0[\rho(\vec{r})]$ corresponding to a non-interacting system of electrons is assumed. The electron-electron Coulomb interaction $V[\rho(\vec{r})]$ consists of two terms: the Hartree energy functional $E_H[\rho(\vec{r})]$ and the exchange-correlation energy functional $E_{xc}[\rho(\vec{r})]$. Now the functional of the electron system is expressed as:

$$F[\rho(\vec{r})] = T_0[\rho(\vec{r})] + E_H[\rho(\vec{r})] + E_{xc}[\rho(\vec{r})]. \tag{2.29}$$

The exchange-correlation energy is not known exactly and it is usually obtained within the local density approximation (LDA) [38], or generalised gradient approximation (GGA) [39, 40, 41]. In LDA, the system is treated locally as an uniform electron gas. The exchange correlation energy at each point in the system is the same as that of an uniform electron gas of the same density [42]. In the GGA approach, a gradient to the electron density is added to account for non-homogeneity in the real electron density.

Since a non-interacting model is assumed for the kinetic energy, the variation procedure leads to a self consistent set of equations, called the Kohn-Sham equation:

$$\left[-\frac{\hbar^2}{2m}\nabla^2 + V_{scf}(\vec{r})\right]\phi(\vec{r}) = \epsilon(\vec{r})\phi(\vec{r}), \tag{2.30}$$

$$V_{scf} = v(\vec{r}) + \frac{\delta E_H[\rho(\vec{r})]}{\delta\rho(\vec{r})} + \frac{\delta E_{xc}[\rho(\vec{r})]}{\delta, \rho(\vec{r})} \tag{2.31}$$

where $\phi(\vec{r})$ and ϵ are the wave function and energy of a *single electron*. V_{scf} is the self-consistent potential, that is the effective potential, which an electron experiences. Essentially, the many electron problem posed by equation 2.26 is reduced to a simpler self-consistent one-electron form, through the Kohn-Sham equations. The

eigenvalues of the Kohn-Sham equation gives the ground state electronic structure of the system.

Once the ground state electronic structure is determined, the optimised mean position of the atoms in the system is known and the phonon dispersion and density of states can be obtained via the direct method [43]. The Hellmann-Feynman forces are obtained by displacing non-equivalent atoms from their equilibrium positions to determine the force constants and dynamical matrices. Phonon energies and polarization vectors at a given wave vector follow from the exact diagonalization of the dynamical matrix.

All lattice dynamics calculations presented in this thesis were performed by Dr. habil. P. Piekarz from the Institute of Nuclear Physics (Polish Academy of Sciences) in Krakow, Poland. The *ab initio* calculations were performed using the DFT implemented in the VASP [44] program using the full potential projector augmented-wave method [45]. Phonon energies, dispersion relations, thermodynamic and elastic properties were calculated from the direct method implemented in the PHONON software [43].

2.2 Experimental techniques

2.2.1 Molecular beam epitaxy

Molecular beam epitaxy (MBE) was the technique used for the growth of all EuO samples investigated in this thesis. MBE is a process for growing epitaxial films of a wide variety of materials, ranging from simple metals to complex oxides [46]. A directed beam of atoms or molecules is created by heating of a material in an ultra high vacuum (UHV) environment. The beam impinges on a clean crystal surface (substrate) kept at elevated temperatures to provide enough energy to the arriving atoms, enhancing their mobility on the surface. The rest of the atoms that do not reach the substrate condense on the cold walls of the chamber. The UHV environment ensures extremely small amount of impurity atoms. The growth can be abruptly terminated by employing a shutter to block the beam, thus enabling to control the film thickness on an atomic level. The material source is usually placed in an effusion cell which creates a directed beam up on heating. The effusion cell consists of thermocouples, inert crucible containing the starting material and a resistive heater. Effusion cells are designed to operate at temperatures up to about 1500°C. Electron beam evaporators are used for materials characterised with higher sublimation temperatures. As the atom/molecule beam reaches the surface of the heated substrate, a series of surface processes occur. The first step is the adsorption of the incoming atoms on the surface, followed by the surface migration. These migrating atoms tend to occupy the crystal lattice points of the substrate or the

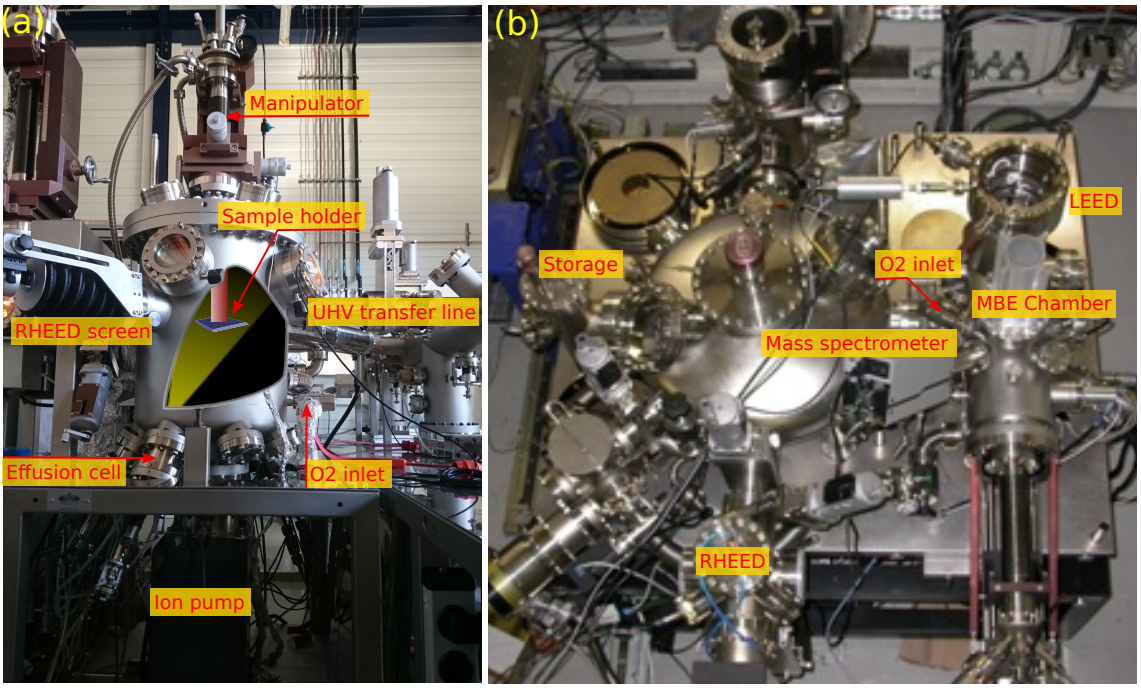

Figure 2.3: The MBE chambers that were used for the growth of oxide thin films at (a) the UHV Analysis laboratory of ANKA and (b) ID18 beamline of the ESRF.

epitaxial layer that is already formed. The atoms that are not incorporated into the crystal lattice are thermally desorped, provided the substrate temperature is high enough for the atoms to escape.

The growth process of the epitaxial thin films using MBE is similar to the growth of bulk crystal except for the influence of the substrate. The influence of the substrate includes lattice mismatch, thermal stress, defects appearing at the substrate/film interface and the chemical interaction between the film and the substrate. The following three main epitaxial growth modes have been identified [47]:

1. In the Volmer-Weber mode, or island growth mode, the atoms arrange themselves into islands at different nucleation sites. This mode occurs when atoms of the deposited material are stronger bound to each other than to substrate.

2. In the Frank-van der Merwe mode, or layer by layer mode, the atoms condense onto a complete layer before the next layer is formed. This mode is observed when the atoms are stronger bound to the substrate than to each other. The following layers are formed on top of one another with monotonously decreasing binding strength. The epitaxial growth of EuO(0 0 1) on YSZ(0 0 1) follows this particular growth mode [48].

3. In the Stranski-Krastanov mode, a few monolayers are formed at first and then it becomes unfavourable to form anymore complete layers resulting in the formation of island on top of the layers. Such kind of growth mode is

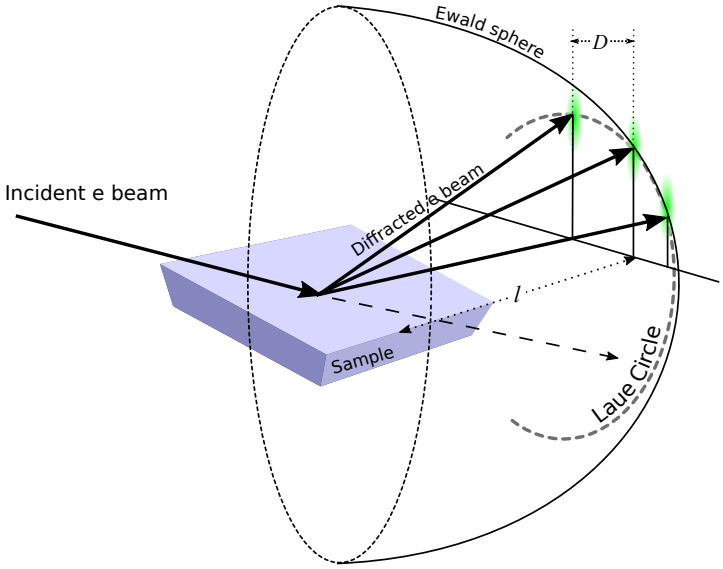

Figure 2.4: The schematic representation of the scattering geometry of RHEED experiment.

common in systems with high epitaxial strain [49].

The samples studied within this thesis were grown in two UHV systems that are located at the UHV laboratory of ANKA, KIT and at ID18 beamline of the ESRF. Both chambers were pumped with three kinds of vacuum pumps, namely rotary pumps, turbo molecular pumps and ion pumps. The base pressure of the UHV chambers at ID18 and ANKA were approximately 4×10^{-11} mbar [50] and 5×10^{-11} mbar, respectively. The images of these chambers are shown in figure 2.3. The Eu metal was evaporated from an effusion cell with a pyrolytic boron nitride crucible. The protective Niobium capping layer was evaporated directly from Nb metal rods that were loaded in a 4-pocket electron beam evaporator. The partial pressures of various elements inside the UHV chambers were monitored by a residual gas analyser. Both MBE growth chambers are attached to other UHV chambers that facilitate surface characterisation using RHEED and LEED. The UHV Analysis Laboratory of ANKA enabled additional *in situ* characterisation techniques such as XPS and AFM.

2.2.2 Reflection high energy electron diffraction

Reflection high energy electron diffraction (RHEED) is a powerful technique for structural characterisation of solid surfaces. It can be even employed in real-time, during the epitaxial growth, to monitor the evolution of thin films. The scattering geometry of RHEED is shown in figure 2.4. A focused electron beam is incident on the sample surface at grazing angle. Diffraction patterns are formed on the fluorescent screen by the electrons that are diffracted from the surface lattice. Various

surface related information including interplanar spacing can be obtained from the diffraction pattern. The electron gun and RHEED detector are located far from the film to avoid interference with the crystal growth process and to be shielded from the hot evaporation sources. The grazing-incidence scattering geometry makes the RHEED extremely surface sensitive technique. The electrons are typically accelerated to energies less than 100 keV, leading to large wave vectors $\vec{k}$ compared to the typical reciprocal lattice spacing. Consequently, the Ewald's sphere has a large radius and cuts through many reciprocal space points, which gives rise to many reflections [51]. The shape and position of the diffracted spots on the screen carry important information about the surface morphology. Figure 2.5(a) shows the case where the electrons are diffracted from a perfectly flat surface. These electrons are diffracted in trajectories that exactly fall on the Laue ring. A stepped, or wavy surface, as shown in figure 2.5(b), results in vertical streaks, or vertically elongated spots that lie on the Laue ring. The vertical elongation results from the larger intersection between the broadened crystal truncation rods and the Ewald's sphere. The RHEED images of a surface that has island-like formations are shown in figures 2.5(c-e). The electrons transmitted through these islands diffract and form a pattern on the screen. Depending upon the aspect ratio of the islands, these diffraction spots become elongated in horizontal, or vertical directions.

The in-plane lattice parameter d_{hkl} of the crystal surface can be derived from the horizontal spacing between the diffraction spots in the RHEED image [51]. In case of islands, the out-of-plane lattice parameter can be calculated from the vertical distance between the diffraction spots. The electrons are scattered from the surface in accordance with the Bragg law. Since the angle of incidence is very small, the following approximation can be used:

$$2sin(\theta) = tan(2\theta) = \frac{D}{l}, \tag{2.32}$$

where θ is the incident angle, D is the distance between the RHEED spots/streaks

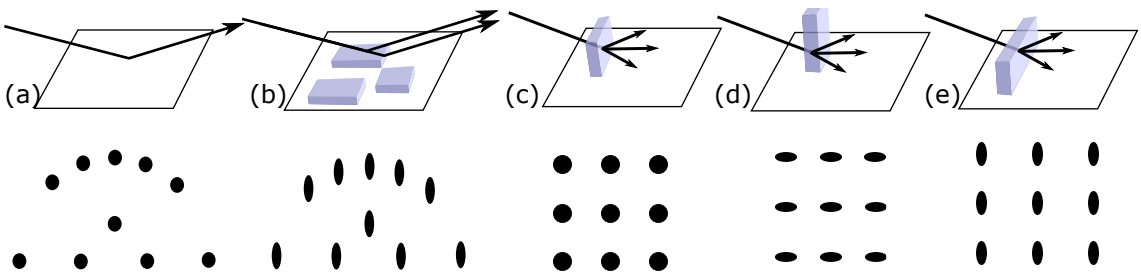

Figure 2.5: The RHEED pattern obtained on the fluorescent screen depends on the surface morphology. The shape and arrangement of the diffraction spots in the RHEED images for (a) perfect crystal, (b) stepped surface, (c) islands of nearly equal width and height, (d,e) islands with large aspect ratio.

and l is the distance between screen and the sample.

Therefore the Bragg law in this case can be rewritten as:

$$2d_{hkl}sin(\theta) = n\lambda, \tag{2.33}$$

$$d_{hkl} = \frac{l\lambda}{D}, \tag{2.34}$$

where λ is the wavelength of the electrons. At a certain accelerating voltage of the RHEED gun, the constant $l\lambda$ can be determined by performing a calibrating RHEED experiment on a known crystal surface. The RHEED images shown in this thesis were obtained with accelerating voltage of 30 keV, correspondingly $\lambda \approx 0.1$ Å. Further information regarding crystal symmetry and lattice spacing along different crystallographic directions can be obtained by rotating the sample with respect to the electron beam.

2.2.3 Atomic force microscopy

Atomic force microscopy (AFM) traces the topography of samples with extremely high resolution, even down to atomic scale. AFM provides spatial information parallel and perpendicular to the surface. The simplified schematics of an AFM setup is shown in figure 2.6. It consist of a cantilever with a scanning tip, laser, photodiode and piezoelectric stage that moves the sample with respect to the tip. The movement of the cantilever is sensed by the laser that is adjusted such that it reflects off the back of the cantilever and falls on to a photodiode. Typically an AFM works in two modes, contact and non-contact mode. In the contact mode, the tip is pressed constantly towards the surface of the sample with certain predefined force (a few nN in magnitude). The sample is raster-scanned along an xy grid and an electronic feedback loop is employed to keep a constant tip-sample force during scanning. The output from the feedback is the surface topography of the sample. In the case of non-contact mode, the tip of the cantilever is not in contact with the sample surface. Instead, the tip is oscillated at its resonant frequency. When the tip is approximately less than a few tens of nanometers from the sample surface, the Van der Waals force between the tip and the sample surface tends to decrease oscillation frequency of the tip. The feedback electronics then adjusts the tip-sample distance such that the resonant oscillation frequency is restored. Therefore, by recording the output of the feedback while raster scanning the sample with respect to the AFM tip, the surface topography can be reconstructed. Since the AFM tip is not in direct contact, non-contact mode is preferred for measuring soft surfaces.

The AFM measurements in this thesis were performed using the *in situ* AFM by Scienta-Omicron located in the UHV Analysis laboratory of ANKA. The measure-

ments were performed in non-contact mode with super sharp silicon tips supplied by Nanoworld AG. The typical tip radius is 2 nm and the half cone angle is $< 10°$.

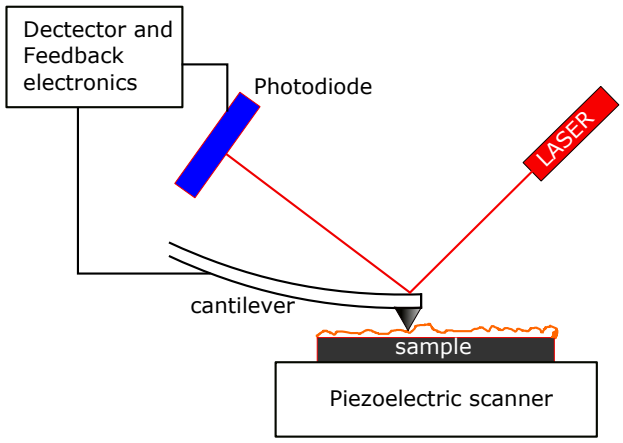

Figure 2.6: Schematic representation of an atomic force microscope that shows its main components and operating principle.

2.2.4 X-ray photoelectron spectroscopy

X-ray photoelectron spectroscopy (XPS) is an analytical method to determine the chemical composition of a solid surface and gives information regarding the binding states of the elements [52]. The technique is based on the photoelectric effect. The sample is placed in vacuum and is exposed to soft x-rays that are typically Kα radiation from Al or Mg anodes. The absorption of x-rays leads to ejection of electrons from the atomic orbitals. The kinetic energy of these electrons is analysed to obtain a spectrum of electron intensity as a function of energy, the so called x-ray photoelectron spectrum. Even though the x-rays could penetrate several micrometers, the surface sensitivity is due to the fact that only a fraction of the generated photoelectrons have enough energy to escape the solid. From the law of conservation of energy follows the equation:

$$E_K = h\nu - E_B - \phi, \tag{2.35}$$

where E_K is the measured kinetic energy of the photoelectron, $h\nu$ is the energy of the exciting photon, E_B is the binding energy of the electron with respect to the Fermi level. ϕ is the work function of the material and surface potential in case of any electrical charging that is likely to occur in the case of insulators. Such surface charging effects can be compensated by the use of an electron flood gun. This device shoots electrons on the surface of the sample to neutralise the positive charge created by the ejected electrons.

Figures 2.7(a) and (b) schematically show photoelectric effect and decay processes of the consequently produced holes. There are two main decay channels for

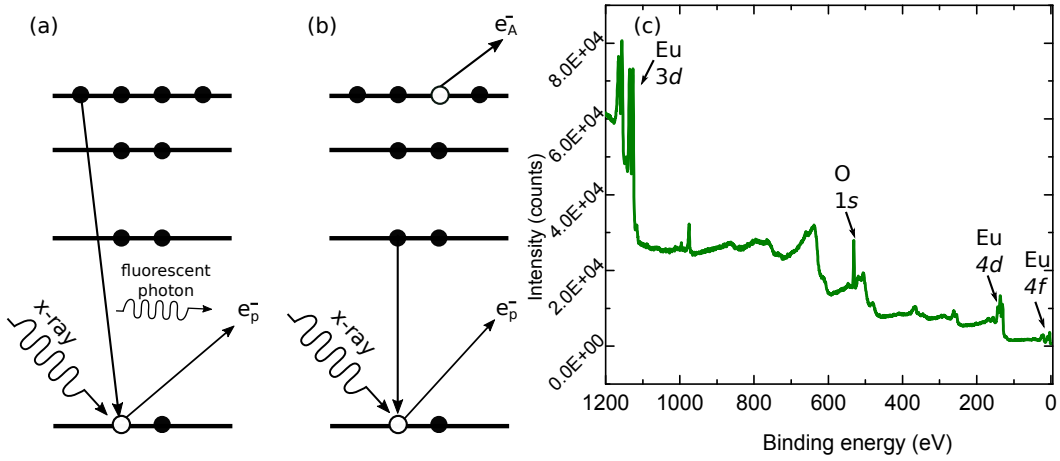

Figure 2.7: Energy level diagram depicting photoelectric effect and possible decay channels via (a) fluorescent photon, (b) emission of secondary electrons. (c) A XPS spectrum of EuO film measured by x-rays from an Al anode.

the holes created by the ejected photoelectrons. An electron from the valence band occupies the core level hole by emitting a photon of appropriate energy, see figure 2.7(a). Another decay mechanism involves the emission of secondary electrons that results in a double-charged ion via the Auger processes is shown in figure 2.7(b). The XPS spectrum of EuO is shown in figure 2.7(c). All aspects of the primary structure is visible in the XPS spectrum. The photoelectrons that are ejected from the solid without suffering energy loss, give rise to discrete peaks whose energy obey equation (2.35) and reflect the electronic shell structure of the atoms. At low binding energies ($E_{BE} < 50$ eV), peaks in the spectrum correspond to valence electrons and at higher binding energies tightly bound core electrons are observed. The binding energy of electrons depends on chemical composition of the sample. Additionally, the Auger electrons that are emitted due to the decay of core holes are observed. The XPS spectrum has a background that increases with increasing binding energy and is dominated by inelastically scattered electrons. The step like nature of the background arises from the electrons that have suffered some energy loss during their escape and also the structure of the background around the peaks in the XPS spectrum carries information about the surface morphology [53].

The XPS spectrometer consist of a x-ray source, electron analyser and a detector enclosed in an UHV chamber. The schematic representation of the x-ray photoelectron spectrometer is shown in figure 2.8(a) and a photograph of the sample stage of the spectrometer that is located in the UHV-Analysis laboratory at ANKA is shown in figure 2.8(b). The angle between the x-ray beam and the sample surface is approximately 45°. The analyser is positioned normal to the surface of the sample.

The chemical composition of the sample can be identified by comparing the measured spectrum to an XPS database. The relative proportion of each element in the sample can be determined from the relative intensity of the peaks in the XPS

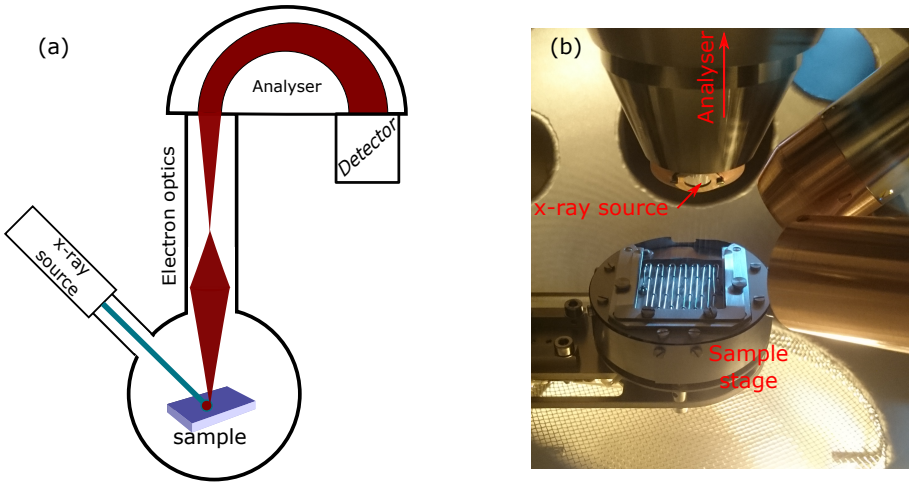

Figure 2.8: (a) Schematic representation of the x-ray photoelectron spectrometer. (b) A photograph of the XPS chamber interior at the UHV Analysis laboratory of ANKA that shows various components of the spectrometer.

spectrum. The XPS peak intensity I is proportional to [53]:

$$I \propto \sigma T \frac{E_{kin}}{E_{pas}} \int_0^d c e^{-x/(\lambda(E_{kin})} dx, \tag{2.36}$$

where σ is the absorption cross section for the transition, T is the transmission function for the analyser, E_{kin} is the kinetic energy of the photoelectron, E_{pas} is the transmission energy of the analyser, c is the depth dependent concentration distribution of the element Z, d is the thickness of the layer and λ is the energy dependent inelastic mean free path of the electrons.

2.2.5 Nuclear resonant scattering

The interaction of atomic nuclei and photons with near resonant energy involves several scattering processes and the detection of individual scattering channels gives insight on different aspects of the sample. The scattering process could be classified as elastic and inelastic as well as coherent and incoherent. Nuclear inelastic scattering looks at the inelastic and incoherent fraction of the nuclear resonant scattering, while the nuclear forward scattering (NFS) is the coherent elastic fraction. The former was employed as the primary method to experimentally obtain the phonon density of states. Similar to Mössbauer spectroscopy, but in the time domain instead of energy domain, NFS gives access to physical properties such as hyperfine interactions and magnetic spin structure. These methods are based on the classical Mössbauer effect, therefore a brief description of Mössbauer spectroscopy and its implementation at synchrotron radiation sources are described below.

The Mössbauer effect

If a naked nucleus (a hypothetical case where nucleus is not surrounded with any electron cloud) of an atom undergoes absorption, or emission of a photon, by the laws of conservation of energy and momentum, the nucleus will experience a recoil. The energy of the incoming photon could be transferred to the nucleus to excite the nucleus to a state with higher energy. After a characteristic time, the mean lifetime τ of the excited state, it decays back to the ground state that is energetically the most favoured state, determined by the Pauli's exclusion principle. The linewidth Γ of this excited state is typically in the order of neV and is given by Heisenberg's uncertainty principle: $\Gamma = \hbar/\tau$. Since the photon has a finite momentum, in order to conserve the momentum the interacting nucleus should experience a recoil. The nuclei recoil energy E_R associated with the emission of a photon with energy E_γ is given by:

$$E_R = E_\gamma^2/2mc^2, \tag{2.37}$$

where m is the mass of the nucleus, c is the speed of light. The energy loss due to recoil is large compared to the extremely narrow natural linewidth of the nuclear excitation and prevents nuclear resonant absorption/emission of the photon. However, in 1958 Rudolf Mössbauer demonstrated that when the atom is tightly bound in a crystal lattice, the recoil of the nucleus is negligible [54] (nuclear mass m in equation 2.37 is replaced with mass of the crystal M). Thus the emitted photon would have exactly the same energy as the energy of the nuclear transition. This allows the resonant absorption/emission of the photon provided that the absorber also resides in a rigid lattice. In reality, solids are not perfectly rigid, but have thermal vibrations described by the phonons. In an Einstein solid, described by a single vibrational frequency ω, the atoms can vibrate with energies equal to integral multiples of $\hbar\omega$. If $E_R < \hbar\omega$, then zero phonons are involved. For $E_R > \hbar\omega$, photon could lose part of its energy to create one, or more phonons. From a classical point of view, these thermal motions introduce Doppler shifts in the energies of the photons. Therefore, the probability for a recoilless interaction in a solid can be expressed in terms of the mean square atomic displacement $< A_{vib}^2 >$ as:

$$f = e^{-\vec{k}^2 < A_{vib}^2 >}, \tag{2.38}$$

where f is the Lamb-Mössbauer factor, or the recoilless fraction and $\vec{k}$ is the incident wave vector of the photon.

Hyperfine interactions

In the previous section of this chapter the excited energy was always referred to as the difference between the excited and ground nuclear state. However, the nucleus is made of charged particles with a spin attribute. Therefore, they interact with

the electric and magnetic fields emanating from the surrounding electron cloud and atoms, rendering the nuclear levels finely non-degenerate. The magnitude of these splittings are very small compared to the energy of the nuclear levels, therefore they are treated as perturbations. These external influences on a nucleus are collectively referred to as hyperfine interactions. They are classified into three interactions: electric monopole, electric quadrupole and the magnetic dipole interactions.

Electric monopole interaction (Isomer shift)

Consider a nucleus with finite volume and a charge density. Let $\vec{r'} = 0$ be the center of the nucleus and $\rho_n(\vec{r'})$ be the nuclear charge density at $\vec{r'}$ and V($\vec{r'}$) be the electric potential at $\vec{r'}$ due to all electric charges outside the nucleus. The total Coulomb energy is [55]:

$$E_e = \int \rho_n(\vec{r'}) V(\vec{r'}) d\tau'. \tag{2.39}$$

Since the nuclear diameter is very small compared to the distance between the nucleus and the external electric charge, the potential V($\vec{r'}$) could be approximated by a Taylor series expansion near the origin:

$$\begin{aligned} E_e = V(0) \int \rho_n(\vec{r'}) d\tau' + \sum_{i=1}^{3} \left(\frac{\partial V}{\partial x'_i} \right)_0 \int \rho_n(\vec{r'}) x'_i d\tau' + \\ \frac{1}{2} \sum_{i,j=1}^{3} \left(\frac{\partial^2 V}{\partial x'_i \partial x'_j} \right)_0 \int \rho_n(\vec{r'}) x'_i x'_j \partial\tau' + ... \end{aligned} \tag{2.40}$$

The first term is the Coulomb interaction energy and is not of interest as it describes the interaction if the nucleus was a point charge. The second term has zero magnitude because nucleus has no dipole moment. The third term (E_3) can be rewritten as:

$$E_3 = \underbrace{\frac{1}{2} \left[\sum_{i=1}^{3} V_{ii} \right] \int \frac{1}{3} r'^2 \rho_n(\vec{r'}) \partial\tau'}_{electric\,monopole\,interaction} + \underbrace{\frac{1}{6} \sum_{i,j=1}^{3} V_{ij} Q_{ij}}_{electric\,quadrupole\,interaction} , \tag{2.41}$$

where

$$Q_{ij} = \int (3x'_i x'_j - \delta_{ij} r'^2) \rho_n(\vec{r'}) \partial\tau' \tag{2.42}$$

$$V_{ij} = \left(\frac{\partial^2 V}{\partial x'_i \partial x'_j} \right)_0 . \tag{2.43}$$

Q_{ij} is the nuclear quadrupole moment tensor and V_{ij} is the electric field gradient.

The electric monopole interaction term in equation 2.41 is dominated by the scalar potential V that is created by the surrounding electron cloud and the charge distribution in the nuclear volume. Assuming that V obeys the Poisson equation

and the nucleus has a uniform spherical charge distribution, we could rewrite the electric monopole interaction term as:

$$E_M = \frac{2\pi}{5} e|\Phi(0)|^2 R^2, \tag{2.44}$$

where e is the charge of the electron, $\Phi(0)$ is the probability of finding a charge at the center of the nucleus and R is the radius of the nucleus. The radius of the nucleus in the excited state differs from that in the ground state by a very small magnitude. Therefore, the assumption $R_e - R_g = \delta R$ and $R_e + R_g = 2R$ is valid. The difference in the electric monopole interaction term ΔE_M of the ground and excited states is:

$$\Delta E_M = E_M^e - E_M^g = \frac{2\pi}{5} e|\Phi(0)|^2 R^2 \left(\frac{\delta R}{R}\right). \tag{2.45}$$

For a naked nucleus and a nucleus surrounded by an electron cloud in the ground state the radius remains the same, however the magnitude of $\Phi(0)$ is different. The s electrons can be found inside the nucleus with certain finite probability owing to their zero angular momentum. To a certain extent the p electrons can also be found within the nucleus if relativistic effects are considered. Thus depending on the valence state of the atom and chemical bonding properties of the compound the electron density at the nucleus changes.

This change leads to an energy shift of the Mössbauer spectrum, which is referred to as chemical or isomer shift. The isomer shift is always expressed as a relative value with respect to a reference material containing the same isotope. For example, for the experiments performed in this thesis an Eu_2O_3 pellet was used as an reference while measuring the EuO sample. The difference in chemical composition of both

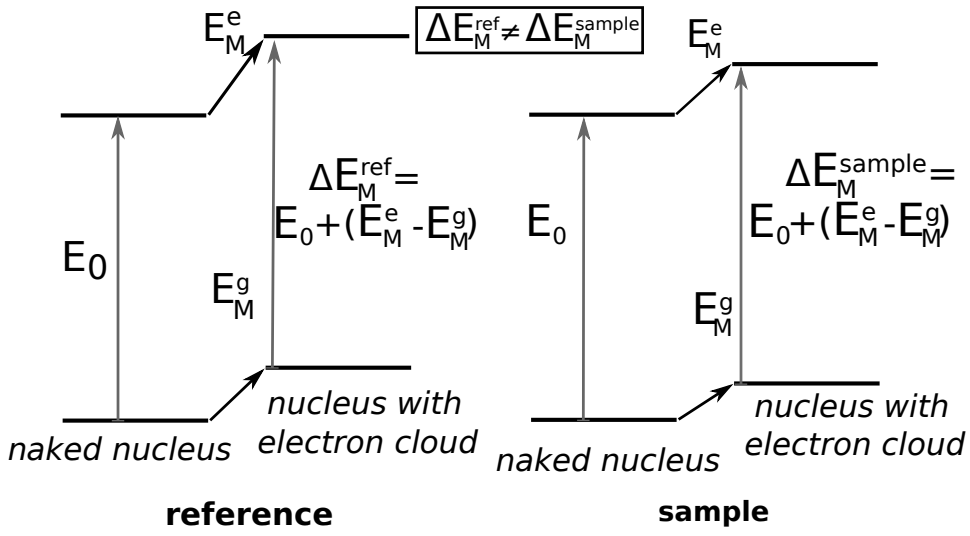

Figure 2.9: Schematic diagram depicting nuclear energy levels of the same isotope in two different compounds in ground and excited state.

materials results in a measurable isomer shift. A schematic representation of the nuclear levels of the reference material and the sample are shown in figure 2.9. The Isomer shift can be expressed as:

$$E_{is} = \Delta E_M^{ref} - \Delta E_M^{sample} = \frac{4\pi}{5} S(Z) \left[|\Phi^{ref}(0)|^2 - |\Phi^{sample}(0)|^2 \right] \frac{\delta R}{R} R^2, \qquad (2.46)$$

where ΔE_M^{ref} and ΔE_M^{sample} are the difference in energies between ground and the excited states of the reference and the sample, respectively.

Electric quadrupole interaction

The electric quadrupole interaction term in equation(2.41) is:

$$E_Q = \frac{1}{6} \sum_{i,j=1}^{3} \underbrace{\left(\frac{\partial^2 V}{\partial x_i' \partial x_j'} \right)_0}_{electric\,field\,gradient} \underbrace{\int (3x_i' x_j' - \delta_{ij} \vec{r'}^2) \rho_n(\vec{r'}) d\tau'}_{nuclear\,quadrupole\,moment}. \qquad (2.47)$$

This interaction consist of contributions from the electric field gradient and the nuclear quadrupole moment. The nuclear quadrupole moment depends on the shape of the nucleus. Assuming a symmetric nucleus along the z axis, the shape can be characterised by a single independent variable Q. When the nucleus has a prolate shape, i.e. longer along the z axis compared to the x and y, Q is positive and vice versa for an oblate shaped nucleus. Quantum mechanically Q can be approximated as $I(2I-1)$, where I is the nuclear angular momentum [55]. When $I = 0$ or $1/2$, the shape of the nucleus is spherical and the quadrupole moment vanishes.

The electric field gradient term in equation 2.47 originates from the electron cloud that surrounds the nucleus and also by the electron cloud of the surrounding ligands. Since the s orbital is spherically symmetric, electrons in the s orbital that surround the nucleus do not contribute to the electric field gradient. The asymmetry parameter for the electric field gradient is defined as $\frac{V_{zz}-V_{xx}}{V_{xx}}$. Assuming z as the quantisation axis and using the raising and lowering operators $\hat{I_\pm} = \hat{I_x} \pm i\hat{I_y}$, the Hamiltonian for electric quadrupole interaction becomes [25]:

$$H_Q = \frac{eQV_{zz}}{4I(2I-1)} \left[3\hat{I_z}^2 - \hat{I}^2 + \frac{1}{2}\eta(\hat{I_+}^2 + \hat{I_-}^2) \right], \qquad (2.48)$$

The eigenvalues of the Hamiltonian are:

$$E_Q = \frac{eQV_{zz}}{4I(2I-1)} [3m^2 - I(I+1)] \left(1 + \frac{\eta^2}{3} \right)^{\frac{1}{2}}, \qquad (2.49)$$

where $m = I, I-1, .. - |I|$.

The electric quadrupole interaction lifts the degeneracy of the nuclear levels with spin I to $\frac{2I+1}{2}$ sub-levels. Figure 2.10 shows the nuclear levels of ground and first

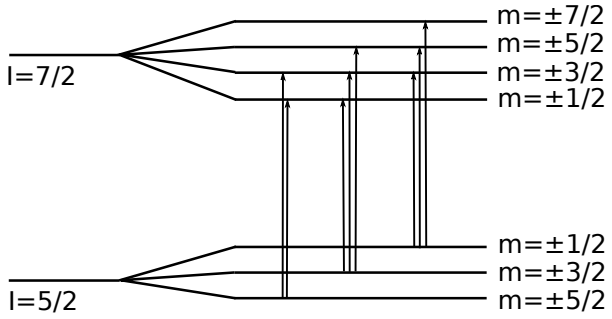

Figure 2.10: Quadrupole splitting of nuclear energy levels $I = 5/2$ and $7/2$ of ^{151}Eu nucleus. The allowed nuclear transitions are also indicated.

excited states of ^{151}Eu nucleus under the influence of electric quadrupole interaction. The ground state $I = 5/2$ splits into 3 sub-levels and the exited state $I = 7/2$ splits into 4 sub-levels, this leads to eight allowed transitions.

Magnetic dipole interaction

This is the interaction between the nuclear magnetic dipole moment $\vec{\mu}$ and the magnetic field produced by the surrounding electrons at the nucleus. It lifts the degeneracy of the energy levels of a nucleus with spin I into $(2I+1)$ levels. The Hamiltonian for the interaction is given by:

$$\mathcal{H}_M = -\vec{\mu}.\vec{B} = -g\mu_n I.\vec{B}. \tag{2.50}$$

The corresponding energies of the split levels are:

$$E_M = -gmB\mu_N, \tag{2.51}$$

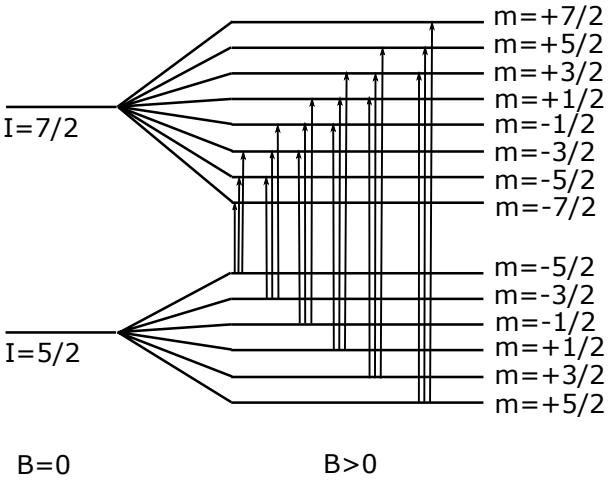

Figure 2.11: Schematic representation of the nuclear energy levels $I = 5/2$ and $7/2$ of ^{151}Eu nucleus under the influence of magnetic dipole interaction. The allowed nuclear transitions are indicated.

Parameter	Value
Isotope mass	151 u
Natural abundance	47.82 %
Transition energy	21.531 keV
Recoil energy	1.65 meV
Lifetime	13.99 ns
Halflife	9.5 ns
Natural linewidth	47.03 neV
Internal conversion coefficient	28
Nuclear angular moment	I_g=7/2; I_e=5/2
Resonance crossection	242.6 kbarn
Nuclear quadrule moment	Q_g=0.903 barn; Q_e=1.28 barn
Nuclear magnetic moment	μ_g=3.472μ_N; μ_e=2.591μ_N

Table 2.1: Nuclear properties of ^{151}Eu. The data are taken from ref. [55, 56].

where g is the nuclear g-factor, the magnetic quantum number $m = I, I-1....,-I$, and μ_N is the nuclear magneton. The γ-ray transitions between ground and excited levels should obey the selection rule - $\Delta m = -1, 0, 1$. In the case of the ^{151}Eu nucleus, the ground state I= 5/2 splits into 6 sub-levels and the excited state I=7/2 splits into 8 sub-levels. This allows 18 different transitions, as depicted in figure 2.11.

There are multiple physical causes behind the magnetic hyperfine interaction. Firstly, the Fermi contact field that is produced by the electron spin densities in the s orbital. The difference in the total number of spin up and spin down electrons in valence orbital indirectly influences the s orbital spin densities. Secondly, the orbital field that is produced by the circular motion of the unpaired electron creates a net magnetic field at the nucleus. In the case of rare earth elements, especially, Eu^{2+} that has 7 unpaired electrons, the magnitude of the oribtal field is large. Lastly, the total spin of the magnetic moment of the valence electrons also contributes to the net magnetic field at the nucleus. This contribution can also be quite large in rare earth compounds with non-zero orbital angular momentum [25].

The nuclear properties of the Mössbauer active isotope of europium ^{151}Eu are listed in table 2.1.

Nuclear forward scattering

This method is an analogue to conventional Mössbauer spectroscopy that is performed in the energy domain, however nuclear forward scattering (NFS) is a time-resolved method. NFS measures the coherent fraction of the elastically scattered photons from the nuclei that carry information about the hyperfine interactions.

Unlike the conventional Mössbauer spectroscopy where the resolution is determined by the natural linewidth of the excited nuclear state, in the synchrotron based NFS the resolution is determined by the high resolution monochromator. The typical bandwidth of 1 meV x-rays excites the nucleus from the ground state to all levels of a non-degenerate hyperfine split resonant level. When such an x-ray pulse is incident on the ensemble of Mössbauer-active nuclei in the sample, with certain probability, all nuclei of the ensemble are excited simultaneously. However, it is not possible to determine the exact energy state to which each individual nucleus is excited. The quantum state can be expressed as a superposition of all possible nuclear excited states with a certain finite probability for each of them. Subsequently, the ensemble decays with the emission of photons with slightly different energies depending on the difference in the energies of the excited hyperfine split nuclear levels. In the forward direction, the propagation direction of the x-ray beam, these photons interfere with each other and form periodic modulations in the measured signal as a function of time. This is the time spectrum of the nuclear forward scattering. From this interference pattern it is possible to calculate the strength of the hyperfine interactions.

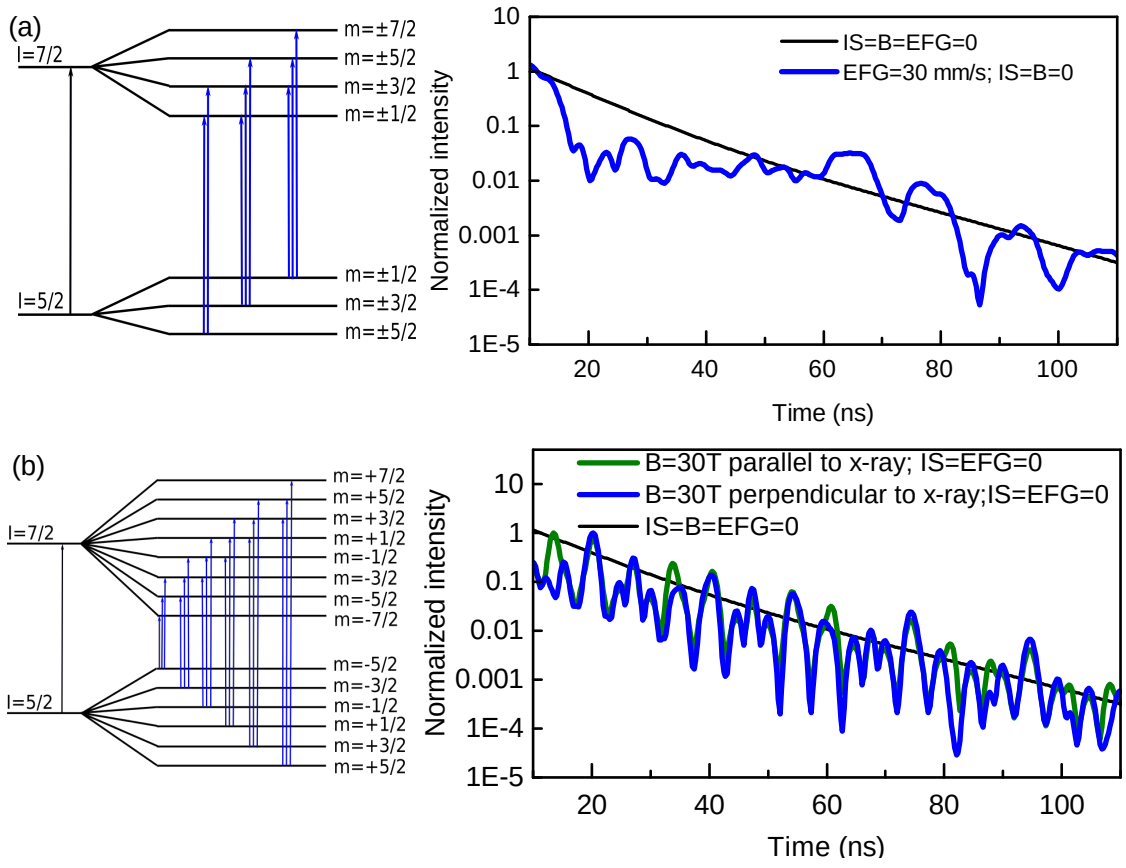

Figure 2.12: The effect of (a) electric quadrupole and (b) magnetic dipole interactions on the grazing incidence NFS spectra of 8 nm thick EuO film. The hyperfine parameters are indicated in each plot. The incidence angle is 2 mrad.

In order to demonstrate the influence of hyperfine interactions on the NFS, time spectra of 8 nm thick EuO film on YSZ substrate are simulated using the REFTIM code [57] assuming different hyperfine parameters. The spectra are shown in figure 2.12. The angle of incidence of the x-ray beam with respect to the sample surface was chosen to be 2 mrad. When the hyperfine interactions are set to zero, an exponentially decaying featureless line is obtained (black line). The effect of electric field gradient on the NFS spectrum is shown in figure 2.12(a), oscillations (quantum beats) are created when the V_{zz} electric field gradient (EFG) is set to 30 mm/s (blue line). The polarization of the synchrotron radiation gives NFS an advantage over the conventional Mössbauer spectroscopy by enabling to determine the direction of the hyperfine field. The NFS spectra that are simulated assuming a magnetic hyperfine field of 30 T oriented parallel (green line) and at azimuthal angle of 90° (blue line) with respect to the x-ray beam are show in figure 2.12(b).

Nuclear inelastic scattering

Soon after the discovery of the Mössbauer effect it was clear that nuclear resonant absorption could be used as a method for probing atomic dynamics. This technique however did not develop until the advent of third generation synchrotron radiation sources. The nuclear inelastic scattering (NIS) method detects the incoherent inelastic fraction of the photons scattered from the material upon nuclear resonant absorption. The resonant nuclei in the solid provide a very accurate energy reference only limited by its natural linewidth. When the incident photon has the same energy as of the nuclear excited state, resonant absorbtion takes place. However, when the energy of the incoming photon is off resonance in the millielectronvolt range, still the resonant process could take place by a phonon assisted mechanism. The resonant transistion occurs only when the total energy of the photon and the involved phonon equals the energy of the nuclear transition. Thus the phonon spectrum of the Mössbauer active element can be obtained by scanning the energy of the incident radiation in the vicinity of the nuclear transistion energy. When resonant absorption takes place, nuclear decay products such as fluorescence, or conversion electrons are emitted after the lifetime time of the excited state. The quantity of nuclear decay products observed at a certain energy off resonance is proportional to the number of phonon states available [58, 59, 60].

An excited nucleus can relax back into its ground state via radiative decay and internal conversion with relative probabilities of $\frac{1}{1+\alpha}$ and $\frac{\alpha}{1+\alpha}$, respectively, where α is the internal conversion coefficient. Since $\alpha > 1$ for most Mössbauer-active isotopes, the major channel of decay is internal conversion. Due to very small electron escape length, the electron conversion signal is surface sensitive. The radiative decay has two channels. Firstly, the nuclear resonant fluorescence where the incident photon is absorbed and re-emitted with the same energy. Secondly, the atomic fluorescence

that originates from the electronic recombination of the hole that is created after the emission of a conversion electron. The latter one of these two channels is the most prominent and the total intensity of the fluorescence can be estimated by:

$$I(E) = I_0 \rho \eta_k \frac{\Gamma_K}{\Gamma_0} \sigma(E), \tag{2.52}$$

where I_0 is the incident flux, ρ the effective area density of the nuclei, and η_k the K-fluorescence yield. The ratio of non-radiative Γ_K linewidth to natural linewidth Γ_0 is $\alpha_K/(1+\alpha)$, where α and α_K are the total and partial internal conversion coeffients. The crossection for nuclear resonant absorption of a photon with energy E is given by:

$$\sigma(E) = \frac{\pi}{2} \sigma(E_0) \Gamma_0 S(E - E_0, \vec{k_0}), \tag{2.53}$$

where $\sigma(E_0) = \sigma_0$ is the nuclear absorption coefficient at resonance energy. $S(E, \vec{k})$ is the normalized absorption probability per unit energy interval at the energy E. It can be expressed as [25]:

$$S(E, \vec{k_0}) = \frac{1}{2\pi} \int_0^\infty e^{-Et - \Gamma_0 t/2} F(\vec{k_0}, t) dt \tag{2.54}$$

$$F(\vec{k}, t) = \left\langle e^{-i\vec{k}.r(\vec{0})} e^{i\vec{k}.r(\vec{t})} \right\rangle_T . \tag{2.55}$$

The function $F(\vec{k}, t)$ describes the correlation of the position of a nucleus at different moments separated by a time interval t. This implies that atomic motion also influences the resonant absorption process. The expression for $S(E, \vec{k_0})$ in equation 2.54 shows that it is independent of the wave vector of the scattered photon $\vec{k_s}$ and therefore independent on the total momentum transfer $\vec{q} = \vec{k_s} - \vec{k_0}$. On the other hand it depends on the incident wave vector thus making inelastic nuclear resonant absorption anisotropic, except for polycrystalline samples and single crystalline sample with cubic symmetry [60, 61]. Inserting equation 2.53 in equation 2.52, the expression for total yield of fluorescent photons becomes:

$$I(E) = I_0 \rho \sigma_0 \frac{\eta_k \alpha_k}{1+\alpha} \frac{\pi}{2} \Gamma_0 S(E, \vec{k}). \tag{2.56}$$

The function $S(E, \vec{k})$ could be now expressed as a sum of contributions from the multiphonon excitations that could exist at finite temperatures [62, 63]:

$$S(E, \vec{k}) = f_{LM} \left(\delta_\Gamma(E) + \sum_{n=1}^{\infty} S_n(E, \vec{k}) \right), \tag{2.57}$$

where f_{LM} is the Lamb-Mössbauer factor and $\delta_\Gamma(E)$ is the Lorentzian function with width Γ.

The function $S(E, \vec{k})$ shows some interesting properties that are important for extracting the phonon density of states from the measured inelastic signal. The

most remarkable one being the fact that the average energy transfer to the lattice per photon emission equals to the recoil energy of a free nucleus. These properties are often referred to as the Lipkin's sum rules [64, 65]:

$$\int ES(E,\vec{k})dE = E_R \tag{2.58}$$

$$\int (E-E_R)^2 S(E,\vec{k})dE = 4E_R T \tag{2.59}$$

$$\int (E-E_R)^3 S(E,\vec{k})dE = \frac{\hbar}{m} E_R K, \tag{2.60}$$

where E_R is the recoil energy, T is average kinetic energy of the resonant nuclei, M is the mass of the resonant nuclei and K is the mean force constant. The second moment of the function $S(E,\vec{k})$ dictates the temperature dependence and zero-point motion of the bound nuclei, while the third moment describes the binding strength of an atom in the lattice.

From the measured total yield of fluorescence $I(E)$, it is possible to calculate the phonon DOS, Lamb-Mössbauer factor, force constants and other thermoelastic properties. Inserting equation 2.57 in the expression for $I(E)$ in equation (2.52), the measured signal can be represented as a sum of an elastic delta function and an inelastic part $S'(E,\vec{k})$:

$$I(E) = aS'(E,\vec{k}) + bf_{LM}\delta(E), \tag{2.61}$$

where a and b are normalization constants. In practice $a \neq b$ due to detector saturation effects, the area under the elastic peak is not proportional to the Lamb-Mössbauer factor. The main focus of the analysis is to determine the constants and separate the contribution from inelastic and elastic parts. The normalization constant a can be obtained from the Lipkin's sum rule given in equation 2.58:

$$a = \frac{1}{E_R}\int I(E)EdE. \tag{2.62}$$

After subtraction of the elastic part, the inelastic component of the measured spectrum is given by $I'(E) = aS'(E,\vec{k})$. Since $\int S'(E,\vec{k})dE = 1 - f_{LM}$, the Lamb-Mössbauer factor can be determined:

$$f_{LM} = 1 - \frac{1}{a}\int I'(E)dE. \tag{2.63}$$

Using the value of a and f_{LM} the measured spectrum $I'(E)$ can be decomposed into single and multiphonon contributions, as shown in figure 2.13. In limits of harmonic approximation, the single phonon contribution $S_1(E,\vec{k})$ is related to the phonon DOS $g(E)$ as [25]:

$$S_1(E,\vec{k}) = \frac{E_R g(E)}{E(1-e^{-\beta E})}, \tag{2.64}$$

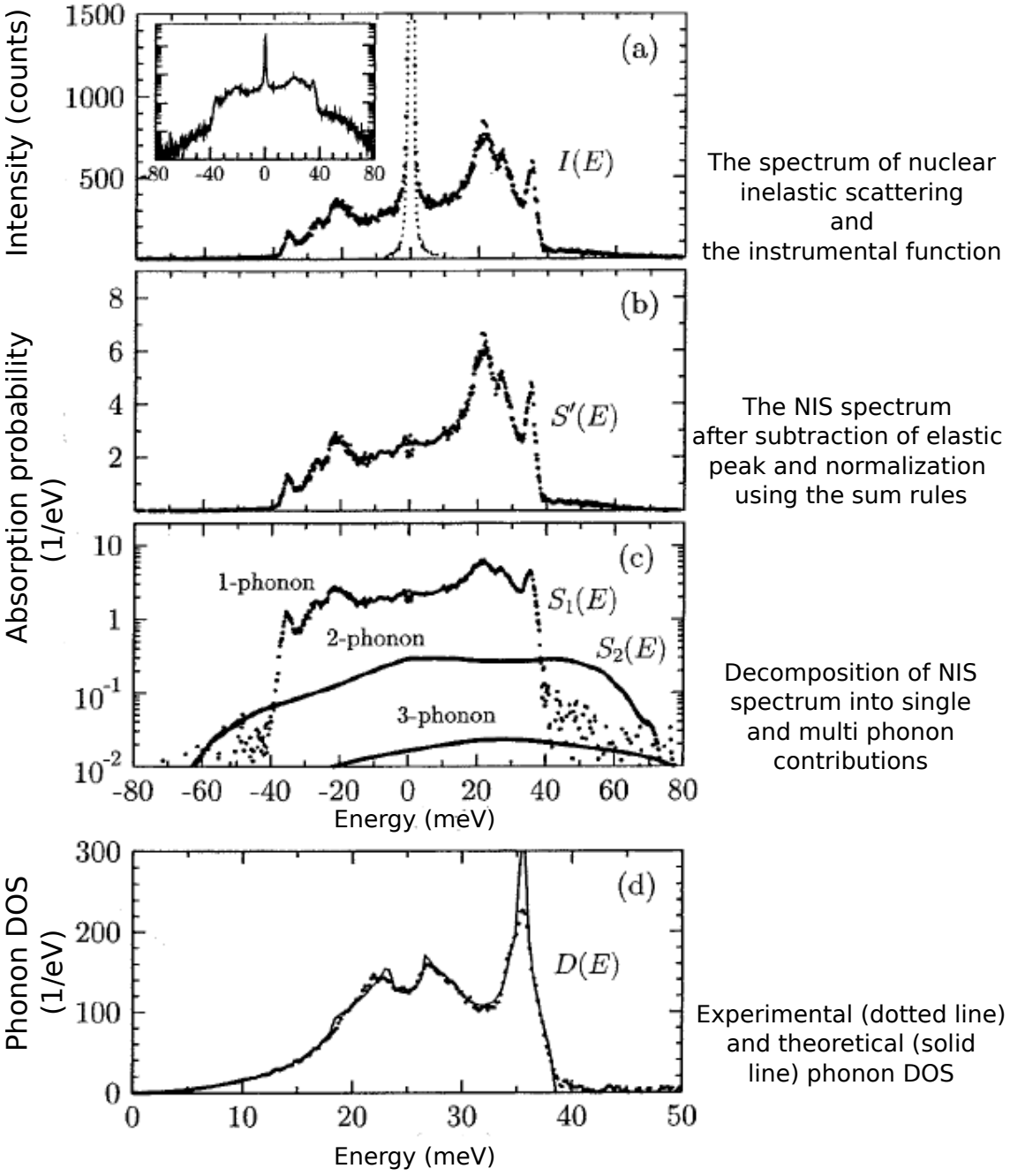

Figure 2.13: The data processing steps for obtaining the phonon DOS from measured NIS spectrum. The data shown here is from a *bcc* Fe crystal [66]. (a) The raw NIS spectrum and the instrumental function. (b) The normalized NIS spectrum using the Lipkin sum rule and the central elastic peak subtracted. (c) Identification of multiphonon contributions using the iterative procedure described by equation 2.65. (d) The phonon DOS determined from the 1-phonon term from the NIS spectrum via equation 2.64. The image is adapted from references [55].

and higher order phonon contributions are given by the sucessive convolutions of the single phonon term [55]:

$$S_n(E,\vec{k}) = \frac{1}{n}\int S_{n-1}(E-E',\vec{k})S_1(E',\vec{k})dE', \qquad n>1. \tag{2.65}$$

The determination of the Lamb-Mössbauer factor in equation 2.63 shows that the precise subtraction of the elastic peak is critical. This is followed by an estimation of the inelastic contribution in the energy range of the elastic peak and is common to assume a Debye solid like behaviour. Figure 2.13 shows the outline of the described formalism for the extraction of phonon DOS from the nuclear inelastic spectra. All the data evaluation was performed using a code called DOS [67].

Experimental setup at ID18 of the ESRF

The UHV system at the nuclear resonance beamline ID18 of the ESRF is an unique facility that combines nuclear resonant scattering methods with *in situ* investigations of thin films and nanostructures. Apart from the MBE growth chamber, the UHV system features surface characterisation tools like RHEED and LEED, as well as a dedicated chamber (NRS chamber) that provides access to x-rays at grazing incidence scattering geometry. The temperature of the sample stage can be varied

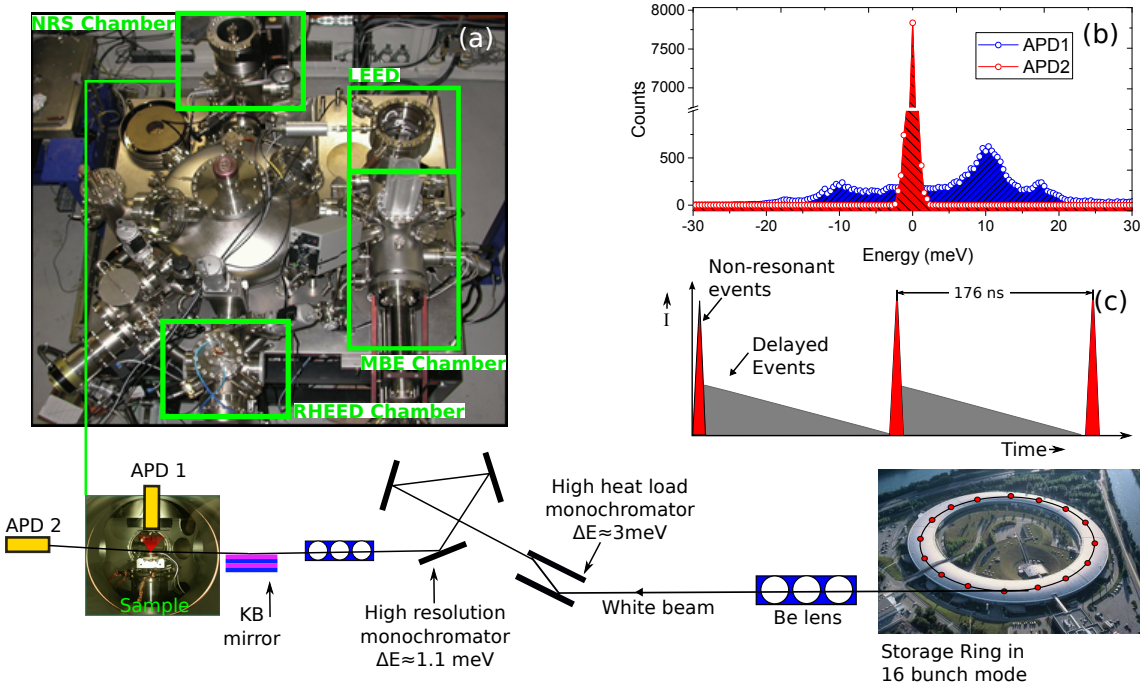

Figure 2.14: (a) The instrumentation at ID18 beamline for performing *in situ* nuclear resonant x-ray scattering experiments. (b) The typical output of APD1 and APD2 showing the NIS spectrum (blue) and the instrumental function (red), respectively.(c) The timed structure of the synchrotron pulse.

from 100 K to 1000 K. This *in situ* setup was crucial for investigating ultrathin EuO films that are extremely sensitive to air. It eliminated the need for a capping layer and therefore surface phonons could be investigated.

The UHV experimental setup is shown in figure 2.14. Nuclear resonance scattering requires the incoming synchrotron radiation to be in pulses with adequate separation in time. This allows one to discriminate the electronic (prompt) scattering from the nuclear delayed resonant products. Therefore, the storage ring was operated in 16-bunch mode to provide a time window of 176 ns between the x-ray pulses. The undulator of the beamline was tuned to the resonant energy of the Mössbauer-active atom, in case of ^{151}Eu that is 21.54 keV. The x-rays with a bandwidth of 300 eV were monochromatised by the high-heat load monochromator that narrows down the bandwidth to ≈ 3 eV. Afterwards, a high-resolution monochromator using high orders Si reflections was employed to achieve an ultimate resolution of ≈ 1.1 meV [68]. The x-ray beam was then focused by Kirpatrick-Baez (KB) mirror to area of $\approx 10 \times 5\,\mu m^2$ on the sample that was inside the NRS chamber of the UHV system. The detector system for nuclear resonant scattering experiment has to have very good time resolution (in nanoseconds), high quantum efficiency, low noise and high dynamic range. These demanding needs are met by avalanche photodiodes (APD), see figure 2.14. APD1 is positioned on the air side in a tube that ends with a Be window and it is mounted on a movable bellow right above the sample surface. This detector collects the fluorescent photons. APD2 is an array of four APDs positioned in the forward direction such that it collects the instrumental function. In order to perform phonon spectroscopy, the incident energy was scanned by the high-resolution monochromator across the resonant energy in a range of ± 100 meV.

The instrumentation for performing NFS is similar to that of NIS experiment shown in figure 2.14. In this case energy of the x-ray beam is tuned to the resonant transition energy. The APD2 collects the spectrum of nuclear forward scattering in a time resolved fashion.

2.2.6 Inelastic x-ray scattering

Inelastic x-ray scattering (IXS) is a technique to probe phonons with very high momentum and energy resolution. Until a few decades ago, inelastic neutron scattering was the primary technique for probing phonon dispersion relations. Given that most compounds have small neutron absorption crossection and the fact that its energy and momentum cover the typical range of phonon dispersions made it an ideal probe for the determination of lattice dynamics. However, some limitations of the technique mainly the relatively large scattering volume required, typically in the order of mm^3, made studies on thin films rather impossible. Therefore, in the scope of this thesis, inelastic neutron scattering proved to be ineffective. The advent of third generation synchrotron sources with highly brilliant x-rays promoted IXS as a

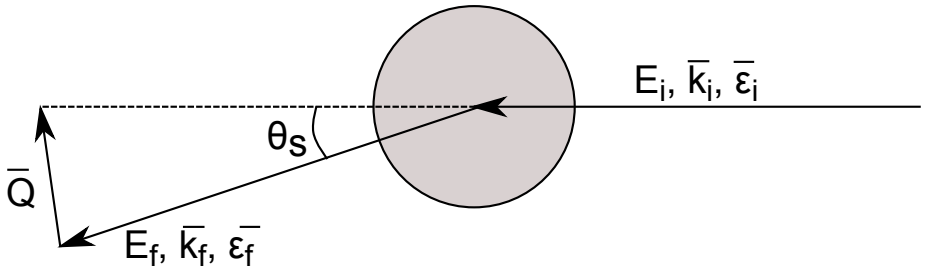

Figure 2.15: Schematic representation of the inelastic x-ray scattering.

powerful method to precisely study the lattice dynamics of crystals as thin as about 50 nm.

The inelastic scattering process is represented in figure 2.15. The laws of conservation of energy and momentum in the process implies that:

$$\vec{Q} = \vec{k_i} - \vec{k_f} \tag{2.66}$$

$$E = E_i - E_f \tag{2.67}$$

$$\vec{Q}^2 = \vec{k_i}^2 + \vec{k_f}^2 - 2k_i k_f cos(\theta_s) \tag{2.68}$$

where $\vec{Q}$ is the momentum transfer, θ_s is the scattering angle, $\vec{k_i}$ and $\vec{k_f}$ are the wave vectors of incident and scattered photons, E_i and E_f are the energies of incident and scattered photons. The energy of the incident photons is in the range of keV, while the phonon excitations are typically in the order of meV. Therefore equation 2.68 can be rewritten as:

$$\frac{\vec{Q}}{\vec{k_i}} = 2sin\left(\frac{\theta_s}{2}\right). \tag{2.69}$$

This shows the strongest feature of IXS that the ratio of exchanged momentum between the photon and the crystal depends purely on the scattering angle, unlike the conventional inelastic neutron scattering.

The scattering intensity in an IXS experiment is described by the double differential crossection and is proportional to the number of incident photons within an energy and momentum range within a solid angle $\Delta\Omega$. The double differential cross section for the inelastic scattering process shown in figure 2.15, where an electron goes from an initial state $|I\rangle$ to a final state $|F\rangle$ is given by [69]:

$$\frac{\partial^2\sigma}{\partial\Omega\partial E} = r_0^2(\epsilon_i.\epsilon_f)^2\frac{k_i}{k_f}\sum_{I,F}P_I\left|\langle F|\sum_j e^{i\vec{Q}r_j}|I\rangle\right|^2\delta(E - E_f - E_i), \tag{2.70}$$

where r_0 is the classical electron radius, P_I corresponds to the thermal population of the initial state and ϵ is the polarisation of the photons. Equation 2.70 can be reformulated by including the atomic density using the following assumptions. Firstly, we assume an adiabatic approximation that aids to separate a quantum state into electronic and nuclear part: $|S\rangle = |Se\rangle\,|Sn\rangle$. This approximation applies

in the case where the energy transfer is extremely small compared to the excitation energies of a core electron in a bound state. Secondly, we consider only the case in which the electronic part remains unaffected in the scattering process, i.e. the difference between the initial and final state is only associated with the atomic density fluctuations:

$$\frac{\partial^2\sigma}{\partial\Omega\partial E} = r_0^2(\epsilon_i.\epsilon_f)^2\frac{k_i}{k_f} \times \left(\sum_{I_n,F_n} P_{I_n}\left|\langle F_n|\sum_j f_j(\vec{Q})e^{i\vec{Q}\vec{r_j}}\,|I_n\rangle\right|^2 \delta(E-E_f-E_i)\right), \tag{2.71}$$

where $f_k(\vec{Q})$ is the atomic form factor of atom j described by the position vector $\vec{r_j}$. The term in the parenthesis also contains the dynamic structure factor, $\mathrm{S}(\vec{Q},E)$. Assuming that all scattering units in the system are equal, equation 2.71 can be written as:

$$\frac{\partial^2\sigma}{\partial\Omega\partial E} = \left(\frac{\partial\sigma}{\partial\Omega}\right)_{Th}\left|f(\vec{Q})\right|^2 S(\vec{Q},E). \tag{2.72}$$

Therefore, in the case of IXS where photon interacts with the lattice, the scattering intensity is a product of Thompson scattering cross section, atomic form factor and dynamical structure factor. Phonons excited in the crystal induce changes in the structure factor as equation 2.72 suggests. This is reflected in the scattering intensity. The role of phonon polarisation in the scattering intensity is implicitly contained in equation (2.72). Let us consider the general form of $\mathrm{S}(\vec{Q},E)$ in the limits of harmonic approximation:

$$S(\vec{Q},E) = \sum_j \left\langle n(E)+\frac{1}{2}\pm\frac{1}{2}\right\rangle (E_j(\vec{q}))^{-1}F_{in}(\vec{Q})\delta(E\pm E_j(\vec{q})), \tag{2.73}$$

where the sum is over $3k$ phonon modes of a crystal having k atoms per unit cell. The term in the angular bracket is the Bose factor that governs the phonon population at a given temperature and the inelastic structure factor $F_{in}(\vec{Q})$ is:

$$F_{in}(\vec{Q}) = \left|\sum_k M_k^{-1/2} f_k(\vec{Q})\left[e_k^j(\vec{q}).\vec{Q}\right] exp(i\vec{Q}.\vec{r_k})exp(-\omega_k)\right|^2. \tag{2.74}$$

where M_k is the mass, $exp(-\omega_k)$ is the Debye-Waller factor and $\vec{r_k}$ is the position vector of the k^{th} atom in the unit cell. $e_k^j(\vec{q})$ is the phonon eigenvector of the atom k in mode j. The dot product $[e_k^j(\vec{q}).\vec{Q}]$ in equation 2.74 implies that the IXS technique can selectively excite the transverse and longitudinal phonon polarisations. Figure 2.16 shows inelastic scattering geometry in reciprocal space for longitudinal and transverse measurements. The position of the scattering vector $\vec{q}$ in the reciprocal space for the detection of longitudinal phonon in the (h k 0) plane is shown in figure 2.16(a). In the case of transverse measurements, the scattering geometry is such that $\vec{q}$ is perpendicular to the [1 0 0] direction to excite in-plane transverse phonon polarized along the [1 0 0] direction, figure 2.16(b). Equation (2.57) contains

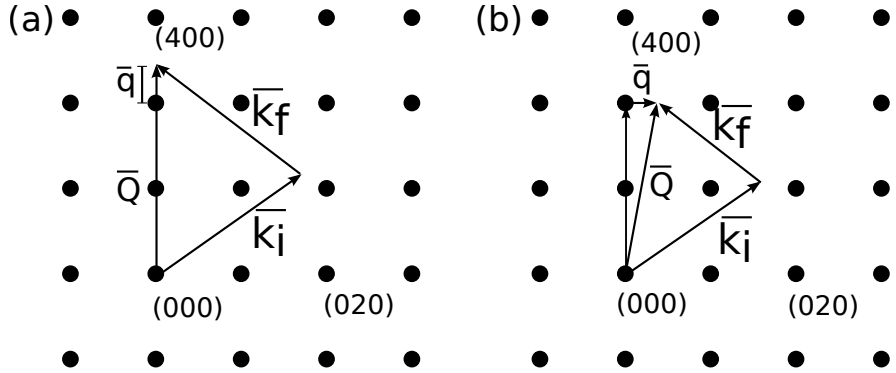

Figure 2.16: Scattering geometries in the reciprocal space for the measurement of (a) longitudinal and (b) transverse phonons.

spin dependent term. This in principle enables IXS to be sensitive to magnetic excitations. However due to the extremely weak magnitude of the magnetic scattering term, it is experimentally impossible to probe magnetic excitations at current x-ray sources yet.

Experimental setup at ID28 of the ESRF

IXS experiments can be performed at three experimental facilities in the world, namely the ESRF, Spring-8 and APS. IXS instruments are all based on the triple axis spectrometer similar to the one used in neutron scattering experiments. The three axes are constituted by monochromator, sample goniometer and analyser. Figure 2.17 shows the layout of the experimental setup at ID28 beamline of the ESRF where the data for this thesis were collected. The x-ray beam from the undulator is first pre-monochromatised with Si(1 1 1) reflection to a relative bandwidth of $\Delta E/E = 2\times10^{-4}$ [69]. Due to the intense heat load, the Si crystals are cooled down to 125 K to be at its near zero thermal expansion coefficient to provide optimum photon flux [70]. The beam is further monochromatised using a Si($n\,n\,n$) backscattering monochromator. The various Si reflections used and their corresponding resolutions

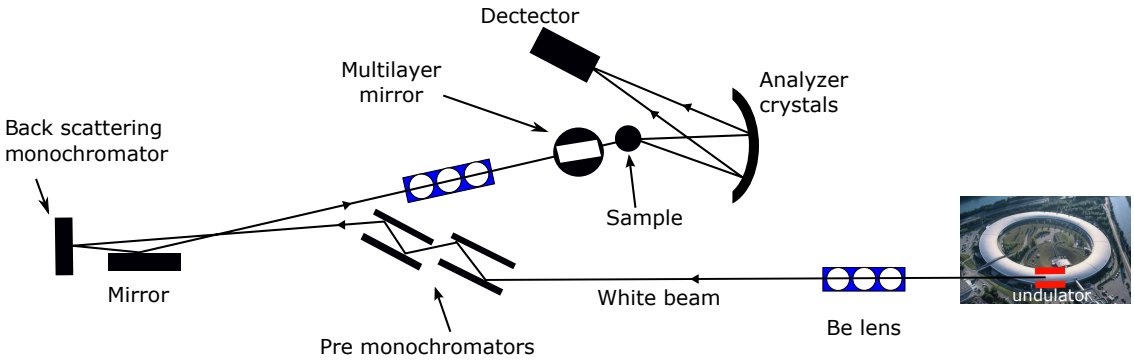

Figure 2.17: Layout of beamline ID28 of the ESRF.

Si Reflection	Energy (keV)	Resolution (meV)
(8 8 8)	15.816	6.0
(9 9 9)	17.794	3.0
(11 11 11)	21.747	1.5
(13 13 13)	25.702	1.0

Table 2.2: The x-ray energies and energy resolutions corresponding to the Si reflections that are available at the ID28 beamline of the ESRF.

are summarized in table 2.2. After monochromatization, the beam passes through x-ray optics for focusing and shaping the beam before it impinges on the sample. The scattered photons are analyzed in energy by five spherical Si crystals in pseudo Rowland geometry. These five crystals enable the spectrometer to simultaneously collect photons scattered at multiple momentum transfers. The photons diffracted by the analyser crystals are collected by low-noise solid-state detectors. IXS experiment requires very high energy resolution for the incident beam as well as the analysers. The common method to obtain higher energy resolution is by employing higher order Bragg reflections from perfect crystals. The resolving power is given by [69]:

$$\frac{\Delta E}{E} = \frac{d_{hkl}}{\pi l_{ext}}, \tag{2.75}$$

where d_{hkl} is the lattice spacing associated with the hkl plane, l_{ext} is the primary extinction length. l_{ext} increases for higher order reflections, therefore for obtaining higher energy resolutions higher order reflections are used.

In addition to the energy resolution of the analysers, their angular acceptance determine the momentum resolution. For a typical momentum transfer around 0.1

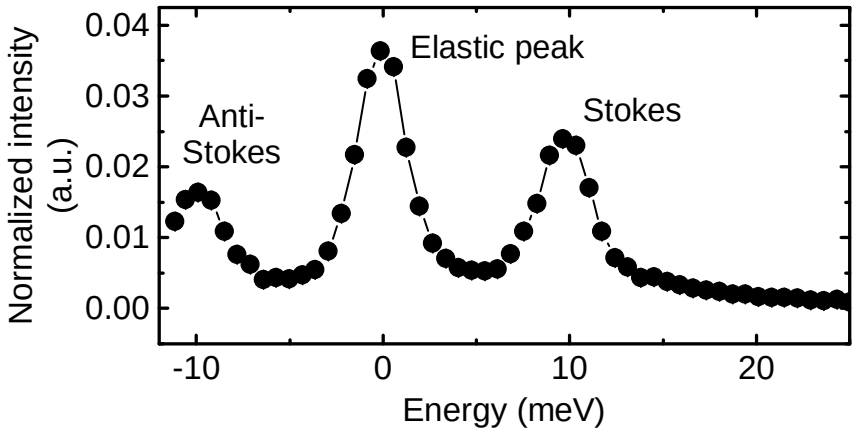

Figure 2.18: A typical energy IXS scan. The intense central peak is the elastic peak while the peaks on the left and right correspond to phonon annihilation and creation processes, respectively.

nm^{-1} the corresponding angular acceptance should be $\approx 10\,mrad$. For such large acceptance, a focussing system is required that does not degrade the energy resolution. This is achieved by assembling numerous small perfect crystals in a spherical geometry to produce a pseudo perfect crystal with spherical shape. An example IXS energy scan is shown in figure 2.18. It consist of Stokes and the anti-Stokes peaks located on the either side of the elastic Bragg peak, corresponding to phonon creation and annihilation processes, respectively. From the scattered photons, the phonon energies and linewidths (FWHM) are precisely determined by using a model function consisting of the superposition of damped harmonic oscillator profiles. The detailed balance is taken into account by the model using the Bose factor. This function is then convoluted with the experimentally determined resolution function and numerically fitted to the IXS spectra using a χ^2 minimisation routine. This mathematical formalism is performed using a FIT28 program developed at the ESRF and is available at the beamline ID28.

Chapter 3

Properties of EuO and Eu_2O_3

This chapter gives a brief summary of crystal structure, electronic and magnetic properties of the two oxides of europium, namely EuO and Eu_2O_3, whose lattice dynamics is the subject of investigation in this thesis.

3.1 Europium monoxide

Europium monoxide is a semiconducting ferromagnet with a Curie temperature T_C of 69 K. At T_C along with the magnetic phase transition tremendous changes in optical and electronic properties are observed. Soon after its discovery, the EuO became known for its giant magneto-optic Kerr [12] and Faraday [13] effects. This strong interaction of magnetism with light had already placed EuO in the spotlight for optoelectronic applications [71]. The magnetic properties of EuO are well explained by the Heisenberg model for ferromagnets, therefore it is regarded as a model system for Heisenberg ferromagnets [11]. The interest in this material has recently been renewed among the scientific community due to its proposed role in the emerging field of spintronics. In the ferromagnetic state, the lower edge of the conduction band shows a considerable exchange splitting that enables EuO to function as an efficient spin filter, or a source/detector for spin polarized current [18]. The fact that EuO has recently been successfully integrated into silicon [19] and its polarization efficiency is the second best among any known material [72], promoted this oxide to a promising candidate for Si based spintronic devices. Furthermore, EuO continues to show other exciting properties such as insulator-to-metal transition accompanied by a colossal magnetoresistance with tremendous changes in resistivity exceeding 8 orders of magnitude [14, 15]. The low Curie temperature is an issue that still needs to be addressed. It has been already shown that T_C can be drastically increased by doping with electron donors such as La or Gd atoms and by compressive strain, reaching up to 200 K [16, 73, 74].

3.1.1 Sample preparation and crystal structure

EuO crystallizes in a *fcc* crystal structure with a space group $Fm\bar{3}m$ and a lattice parameter of 5.144 Å. Figure 3.1 shows the unit cell of EuO. Since its discovery in the early 60s, stoichiometric EuO has been extremely difficult to stablize. According to Shafer *et al.* [75] a temperature of about 1800°C with precise supply of Eu and O are required to form stoichiometric EuO. The phase diagram shown in figure 3.2 shows the extremely narrow window of EuO formation, depicted as region III. Regions I and II correspond to oxygen rich regime that often lead to the formation of higher oxide phases such as Eu_2O_3 or Eu_3O_4. The regions IV and V correspond to Eu-rich oxides where Eu atoms occupy interstitial positions in the lattice, or even form metallic clusters. The physical properties, in particular the Curie temperature of O/Eu rich EuO depend strongly on the stoichiometry.

Early synthesising techniques that involved oxidation of Eu metal, or conversely reduction of Eu_2O_3 were sucessful in stabilizing stiochiometric EuO. However, they failed to produce single crystals [75, 13, 73, 77, 78, 79]. In the early 2000s P. Steeneken [80] demonstrated the growth of EuO thin films in ultra high vacuum (UHV) conditions in the so called adsorption controlled growth regime. The Eu flux and the molecular oxygen were tuned such that the concentration of Eu atoms were slightly higher than the O atoms at the surface of the substrate. The temperature of the substrate was elevated such that the excess Eu atoms are distilled off the surface, yielding a single crystalline and stoichiometric EuO film. This method is a balancing act of Eu and O fluxes, and has proven to be very successful in producing high quality EuO films with thickness ranging from a few monolayers to hundreds of nanometers on several substrates such as Si [81], GaN [82], Yttria stabilized Zirconia [48] and Al_2O_3 [72]. Eu metal and in particular EuO show very high chemical affinity

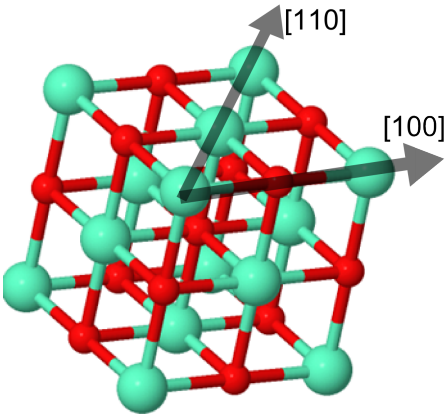

Figure 3.1: Schematic representation of the crystal structure of EuO. Eu and O atoms are indicated with green and red spheres, respectively. Adapted from www.icsd.fiz-karlsruhe.de.

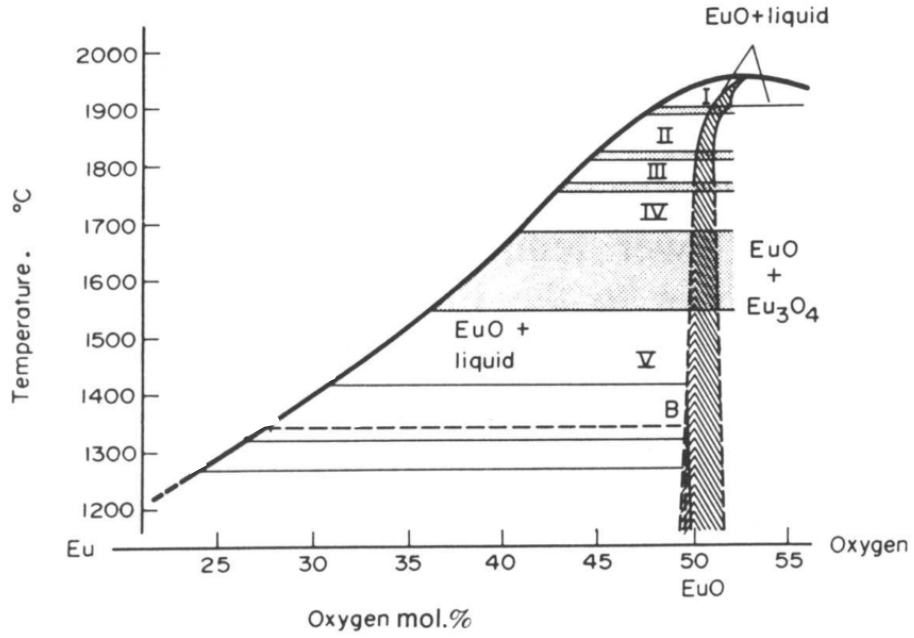

Figure 3.2: Phase diagram for the synthesis of EuO. Adapted from reference [76].

towards water, carbon and oxygen. Therefore, it is of great importance to prepare the samples in UHV condition and to cap them with a suitable protective layer before exposure to air.

3.1.2 Electronic structure

The chemical bond between Eu^{2+} and O^{2-} atoms in EuO is of ionic character, leading to an electronic configuration of europium - $[Xe]4f^7 5d^6 6s^0$ and that of oxygen - $1s^2 2s^2 2p^6$. Two electrons from the $6s$ orbital of Eu metal are transferred to the p orbital of electronegative oxygen atom. This is the reason that europium oxide and europium chalgenides in general are insulators with valence band built from p states of the oxygen and the conduction band is composed of the empty $5d\,6s$ states of europium. The half filled $4f$ orbital of the Eu atom lies near the Fermi edge and is responsible for the magnetic properties, however, due to the very narrow angular distribution of the $4f$ orbitals, they do not take part in chemical bonding. The electronic band gap was experimentally determined to be 1.1 eV [11] and the calculated electronic band structure is shown in figure 3.3(a) [83].

An interesting feature exhibited by EuO is the temperature dependent zeeman/exchange splitting of its conduction band due to exchange coupling with the aligned spins of the $4f$ orbital in its ferromagnetic state. This exchange splitting (ΔE_{ex}) was found to be 0.6 eV which is quite substantial compared to its electronic band gap of 1.1 eV [18]. This is due to the influence of the seven unparied electrons in $4f$ orbital that ultimately add up to a magnetic dipole moment of $7\mu_B$ per Eu

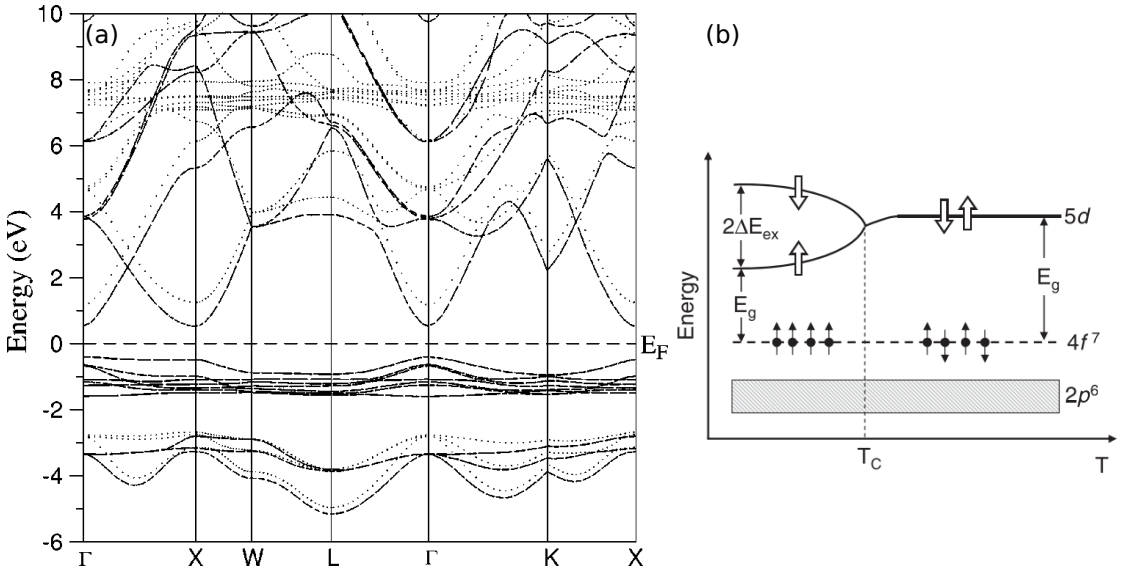

Figure 3.3: (a) The electronic band structure of EuO [83]. (b) A simplifed representation of the temperature dependent electronic band structure [84].

atom. A schematic diagram of the temperature dependence of the conduction band is shown in figure 3.3(b). This exchange splitting has given EuO some fascinating electronic transport properties. Firstly, it allows spin selective electron tunnelling through the exchange split $5d$ conduction band [84]. Secondly, the presence of impurities such as trapped interstitial Eu atoms or O vacanies may induce defect states in the electronic band gap. The exchange splitting of the conduction band may overlap with such defect states to produce a giant drop in resistance leading to a metal-to-insulator transition in non-stoichiometric EuO [14].

3.1.3 Magnetic properties

The magnetism in EuO arises from direct and indirect exchange interactions between the $4f$ orbitals and is quite different from that in $3d$ ferromagnetic metals [85]. The $4f$ orbitals of Eu atoms are half filled. According to the Hund's rules, the half filled $4f$ orbital gives rise to a pure spin moment $S = 7/2$ and an orbital angular moment $L = 0$. The net magnetic moment is $\mu_S = Sg_s\mu_B$, where $g_s \approx 2$ is the Lande-gfactor and μ_B is the Bohr magneton. This results in a rather large net magnetic moment of $7\mu_B$ per Eu atom. The strong ferromagnetic coupling is related to the large ionic radius and density of Eu atoms in the EuO crystal structure.

The Heisenberg model for magnetism suggest that spontaneous magnetisation arises from the exchange interaction between spin moments of neighbouring atoms. This implies that spin magnetic moment of the $4f$ orbitals of Eu^{2+} ions interact with the next nearest neighbour. Since the $4f^7$ orbital has a maximum spin multiplicity of 8 and no orbital contribution, the ferromagnetic ground state has a spherical s like symmetry. Therefore, the exchange interactions can be considered isotropic.

The Hamiltonian for the system considering only the nearest neighbour interaction is given by:

$$\mathcal{H} = -J \sum_{\substack{i,j \\ i \neq j}} S_i . S_j, \tag{3.1}$$

where the subscripts i and j indicate lattice sites, S is the spin angular moment, J is the exchange energy and is positive for ferromagnetic interaction. The three dimensional Heisenberg model predicts a power law for the temperature dependent magnetisation below the Curie point [86]:

$$\sigma \propto (T_C - T)^{\beta}, \tag{3.2}$$

where σ is the reduced magnetisation and β is a constant that is equal to 0.36. The value of β for EuO was found experimentally to be 0.37 [87, 88], which is clear evidence for the validity of the Heisenberg model for EuO.

Later a more complex Heisenberg model that takes into account two exchange interactions J_1 and J_2 between nearest and next nearest Eu^{2+} ions, respectively, was proposed [89]. The exact values of these exchange energies have been determined to be $J_1 \approx 5.3 \times 10^{-5}$ eV and $J_2 \approx 1.0 \times 10^{-5}$ eV from the spin wave spectrum that has been measured by inelastic neutron scattering [90]. However, the macroscopic mechanism behind these exchange interactions is still not clearly understood. The widely accepted explanation of the exchange interaction is given below [91]:

1. Nearest neighbour interaction

   A $4f$ electron is excited from the ground state to the unoccupied and delocalised $5d$ orbital and an exchange interaction occurs with $4f$ electron of the nearest neighbour. These exchange interactions are relatively strong and are ferromagnetic in nature.

2. Next-nearest neighbour interaction

   There are three different possible mechanisms between the next-nearest Eu^{2+} ions. (a) The Kramer-Anderson superexchange - an electron from the $4f$ orbital is transferred to the $4f$ orbital of the next-nearest neighbouring Eu atom via an O atom. This exchange is usually anti-ferromagnetic in nature and is very weak. (b) Superexchange via $d-f$ interaction - an electron from the p orbital of the O atom is transferred to the nearest neighbouring d orbitals of Eu atom. Consequently the $4f$ spins of the Eu atoms are affected. The 180° Eu-O-Eu bond angle ensures a substantial antiferromagnetic exchange. This explains the negative value of J_2 for other Eu chalcogenides obtained in the neutron scattering experiments. (c) A mixture of both the above described mechanisms via hybridisation of the Eu $5d$ and O $2p$ orbitals. The hybridisation of the

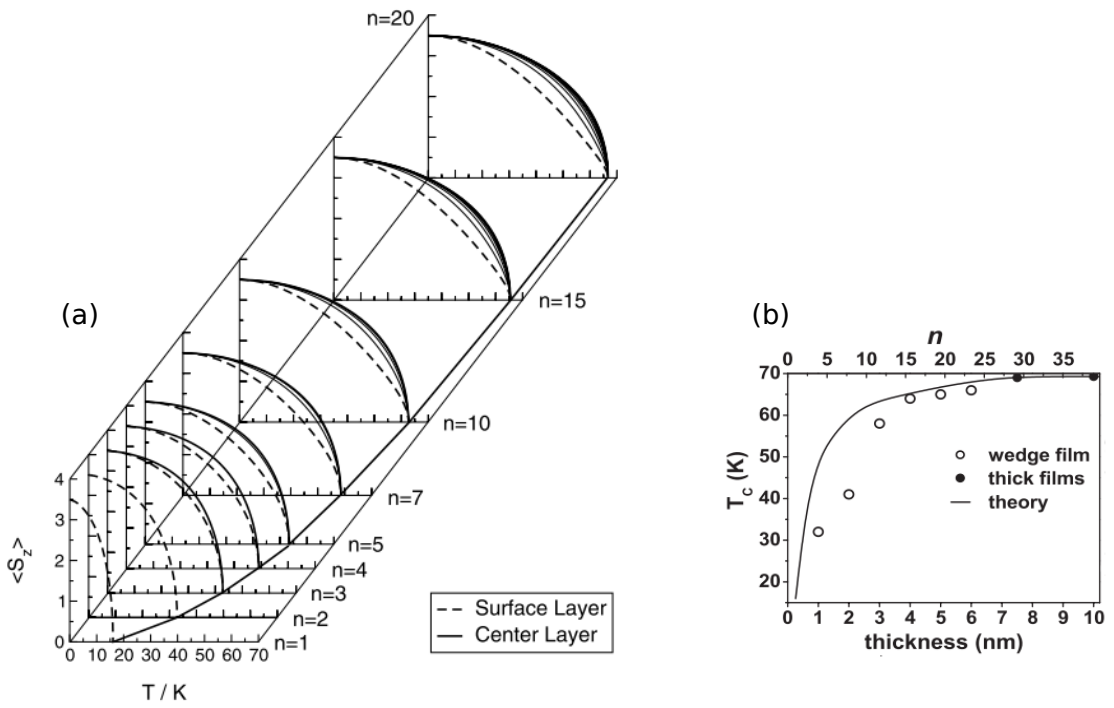

Figure 3.4: (a)Thickness and temperature dependence of the magnetizations of EuO films [92]. (b) Experimental observation of thickness dependence of Curie temperature [93]. n denotes the number of monolayers of the EuO film.

orbitals leads to the formation of bonding and anti-bonding $5d-2p$ molecular orbitals. When an electron from the O atom is excited from the bonding to anti-bonding $5d-2p$ molecular orbital, it experiences an exchange interaction with the localised $4f$ orbitals of the adjacent Eu^{2+} ions. This type of exchange is usually ferromagnetic in nature.

The magnetism, just like the lattice dynamics, deviates from that of the bulk material as the crystal dimensions are reduced to nanometer length scale. Magnetic moment of EuO has been calculated as a function of temperature and film thickness by Schiller and Nolting [92]. Figure 3.4(a) shows the Curie temperature and magnetic moment as function of temperature and thickness. It was found that for film thickness below 10 ML (monolayers, 1ML=1.71 Å), the Curie temperature drops from 69 K to 15 K for 1ML thick film. In the Heisenberg model, Eu^{2+} ions can couple with 12 other Eu ions in the bulk crystal, while at the EuO(0 0 1) surface, this coupling only occurs to 8 other Eu ions. This lowering of coordination number at the surface due to the broken translational symmetry leads to the reduction of interatomic exchange interactions between the $4f$ orbitals. The magnetic contribution of the surface layer to the magnetic properties of the film becomes more prominent as the film thickness is reduced. Therefore, the net magnetisation is also reduced. Experimental evidence for such behaviour of T_C has been demonstrated in

polycrystalline EuO films, see figure 3.4(b) [93].

3.2 Europium sesquioxide

Like the binary oxide of europium, europium sesquioxide (Eu_2O_3) is also a technologically important material due to its high dielectric constant. In microelectronics, capacitors with long retention time and flash memories need materials with large static dielectric constants. Moreover, the continuous downscaling of integrated circuits demand new (high k) materials that can serve as a gate material of nanotransistors. There are many metal oxides that have high dielectric constants, however, the ones that are thermally stable, integrable into silicon and have negligible tunnelling at nanometer thickness are limited to rare earth and transition metal oxides. Another important area of application of the RE_2O_3 is to serve as host materials for lasers and active waveguides. The excellent thermal conductivity, high Stark splitting and low phonon energies make them interesting laser host materials. The common oxides for this application are those based on Yb, Sc and Lu [94, 95]. In this section the properties of Eu_2O_3 as a representative example of the RE_2O_3 family are discussed.

3.2.1 Sample preparation and crystal growth

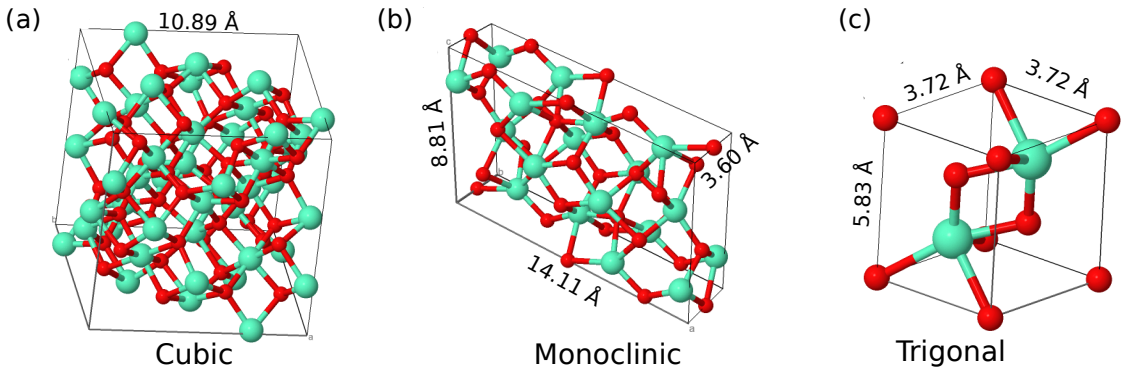

Figure 3.5: Schematic representation of the different polymorphs of Eu_2O_3. Eu and O atoms are represented by green and red spheres, respectively. Adapted from www.icsd.fiz-karlsruhe.de.

Eu_2O_3 crystallises in cubic, monoclinic and rarely in trigonal structures [96, 97]. Figure 3.5 shows the structure of these polymorphs. At ambient conditions, like most of the other rare earth sesquioxides, Eu_2O_3 crystallizes isostructural to the mineral bixbyite (space group $Ia\bar{3}$) and is best described by a simple fluorite cell with two vacancies paired along the body diagonal of the oxygen cube. There are two inequivalent lattice points that Eu atoms occupy in the unit cell, characterised

by site symmetry S_6 and C_2. All Eu atoms are coordinated by heavily distorted octahedra of oxygen atoms, i.e. the coordination number of the cation is six, see figure 3.5(a). Figure 3.6 shows the effect of temperature on the crystal structure of Eu_2O_3 and the other RE_2O_3 compounds. As temperature is increased to approximately 1100°C, the bixbyite structure changes to monoclinic (space group $C2/m$). The Eu atoms are coordinated by seven oxygen atoms. The Eu atoms are seen to be approximately hexagonal closed packed structure, see figure 3.5(b). Figure 3.5(c) shows the trigonal structure of Eu_2O_3 that is formed at temperatures above 1700°C by a slight shift of the oxygen sublattice compared to the monoclinic phase. Other structural phases with hexagonal and cubic symmetries are also reported at temperatures above 2300°C [98, 99].

Large single crystals of monoclinic Eu_2O_3 are usually grown using the Verneuil process [101]. Thin film of Eu_2O_3 have been grown by several techniques such as pulsed laser deposition [102] on $LaAlO_3$ substrate and polymer assisted deposition [103] on SnO_2. Given the technological importance of this material in high-k applications, polycrystalline Eu_2O_3 thin films were successfully deposited on Si using electron beam physical vapor deposition method [104].

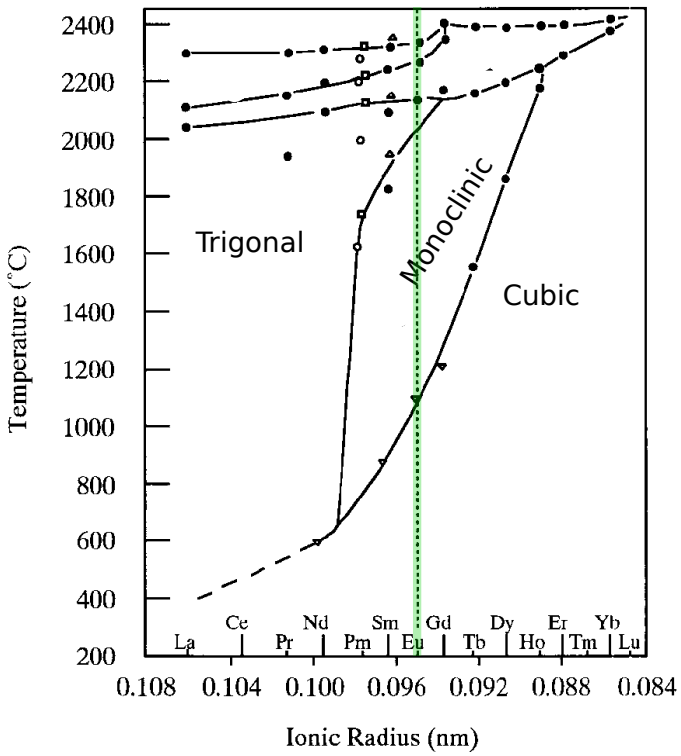

Figure 3.6: Temperature dependence of polymorphic transformations in lanthanoid sesquioxides. Adapted from reference [100].

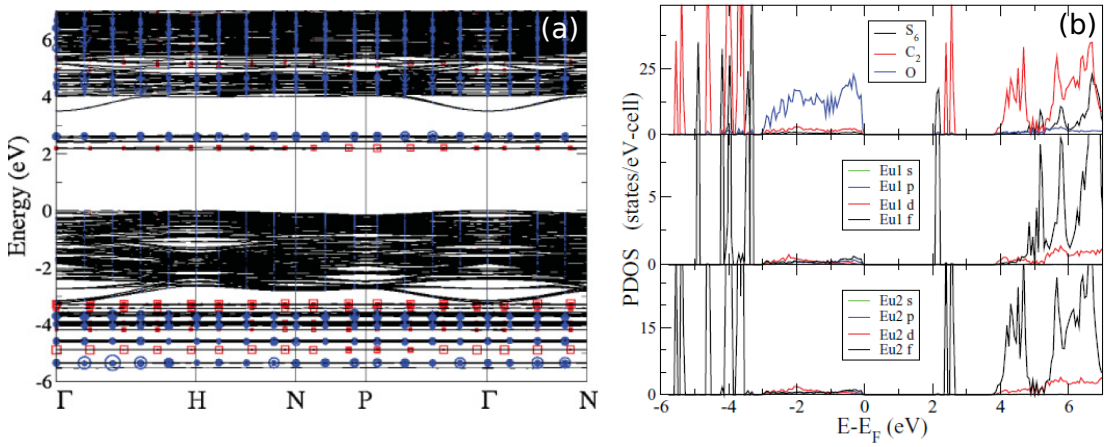

Figure 3.7: (a) Electronic band structure of cubic Eu_2O_3. Eu $4f$ character is denoted by red squares and blue circles for the S_6 and C_2 sites, respectively. (b) Orbital projected electronic DOS of cubic Eu_2O_3. The Eu1 and Eu2 labels indicate the S_6 and C_2 sites, respectively. Adapted from reference [105].

3.2.2 Electronic structure

Figure 3.7 shows the electronic band structure of cubic Eu_2O_3 that have been computed using local density formalism by LDA + U approximation [105]. The conduction band is mainly composed of metal d states and s states. While the valence band is composed of O $2p$ states. The high ionicity is indicated by the narrow energy dispersion of the valence band [106]. The experimental band gap is reported to be approximately 4.5 eV [107]. In a first approximation, the electronic band gap of monoclinic Eu_2O_3 can be also estimated to be similar to that in the cubic structure. This is because the valence band is formed by the non-bonded $2p$ O orbital and the lower conduction band is formed by the non-bonded metal d states. The electronic band gap of other lanthanide oxides ranges from 3.4 eV in Tb_2O_3 to 5.5 eV in Lu_2O_3 [107].

Rare earth sesquioxides are very good insulators with electrical conductivity σ ranging from 10^{-9} to 10^{-12} $Ohm^{-1}cm^{-1}$. They show decreasing trend in σ with increasing atomic number, and σ of Eu_2O_3 is 5×10^{-9} $Ohm^{-1}cm^{-1}$ at 400°C [108]. The electrical conduction of these sesquioxides at room temperature is dominated by electronic conduction and at higher temperatures, above the so called inflection point ($T_B = 570$°C for Eu_2O_3), a considerable contribution from ionic conductivity is observed.

3.2.3 Dielectric properties

Rare earth sesquioxides are well known for their very high dielectric constants and are proposed to be used as gate material in nanotransistors. Among other oxide

REO	Theoretical value of k	Experimental value of k
La_2O_3	14.77	-
Ce_2O_3	14.60	-
Pr_2O_3	14.43	-
Nd_2O_3	14.27	14.3
Pm_2O_3	14.10	-
Sm_2O_3	13.93	-
Eu_2O_3	13.77	13.9
Gd_2O_3	13.60	13.6
Tb_2O_3	13.43	13.3
Dy_2O_3	13.27	13.1
Yb_2O_3	12.60	-
Lu_2O_3	12.43	12.5

Table 3.1: Theoretical and experimental dielectric constants of RE_2O_3. (data from reference [113]).

materials, the rare earth sesquioxides are thermodynamically stable on silicon, have high conduction band offset and high thermal stability, making them possible alternative to SiO_2 [104]. The dielectric constant of Eu_2O_3 was experimentally found to be 13.9, which is similar to the other RE_2O_3 [109]. Table 3.1 summarises the dielectric constants of various RE_2O_3. The lighter lanthanides that crystalise in hexagonal structures were found to have slightly greater dielectric constants than heavier RE_2O_3 that crystalise in cubic structure [106]. However, the experimental values depend strongly on the deposition technique, film thickness and other deposition parameters. For example, according to reference [110], La_2O_3 deposited using electron beam evaporation on Si with thickness varying from 2 to 8 nm had dielectric constants between 8 and 23, while La_2O_3 deposited with CVD technique shows a dielectric constant of 19 [111]. These differences arise from lattice imperfections. It is known that oxygen vacancies in the lattice decrease the Coulomb interaction, which in turn affects the lattice parameter and ultimately the dielectric property [112].

Despite of intense investigations of the physical properties of RE_2O_3, their lattice dynamics, that is of high importance for the proposed applications, remains unknown.

Chapter 4

Lattice dynamics of europium monoxide

Lattice dynamics of EuO remained unknown until recently except for a few Raman scattering experiments [114, 20, 21, 22]. Given its status as a model system for Heisenberg ferromagnet and its exciting prospects in the emerging field of spintronics, determination of the lattice dynamics of EuO is more than necessary. This chapter describes the lattice dynamics study of the ferromagnetic semiconductor EuO that has been performed by a combination of inelastic x-ray scattering, nuclear inelastic scattering, and ab initio calculations. The chapter begins by giving a description of sample preparation and characterization, followed by a comparative analysis of the results of ab initio calculations and x-ray scattering experiments. The temperature dependence of the thermodynamic and elastic properties of EuO determined from the phonon DOS is presented and discussed. A discussion on the temperature and momentum dependent evolution of the phonon linewidths, spin-phonon interaction and its relevance to the spintronic applications of EuO are discussed.

4.1 Sample preparation and characterization

In order to investigate bulk-like EuO film with minimal effects from the broken translation symmetry of the surface and to facilitate inelastic x-ray scattering (IXS) experiments, EuO(001) film of approximately 100 nm thickness was grown on Yttria stabilized Zirconia YSZ(001) using reactive molecular beam epitaxy. The adsorption controlled growth regime has been established by several authors for stabilizing stoichiometric EuO [48, 115]. The growth procedure is based on the conditions described by Sutarto *et al.* [48]. The substrate was heated up to 600° C in an oxygen atmosphere with partial oxygen pressure $p_{ox} = 1 \times 10^{-7}$ mbar for 120 minutes. This step ensures a clean and flat YSZ(001) surface that is visible in the RHEED image in figure 4.1(a). Vacuum out-gassed Eu metal supplied by the Ames Laboratory

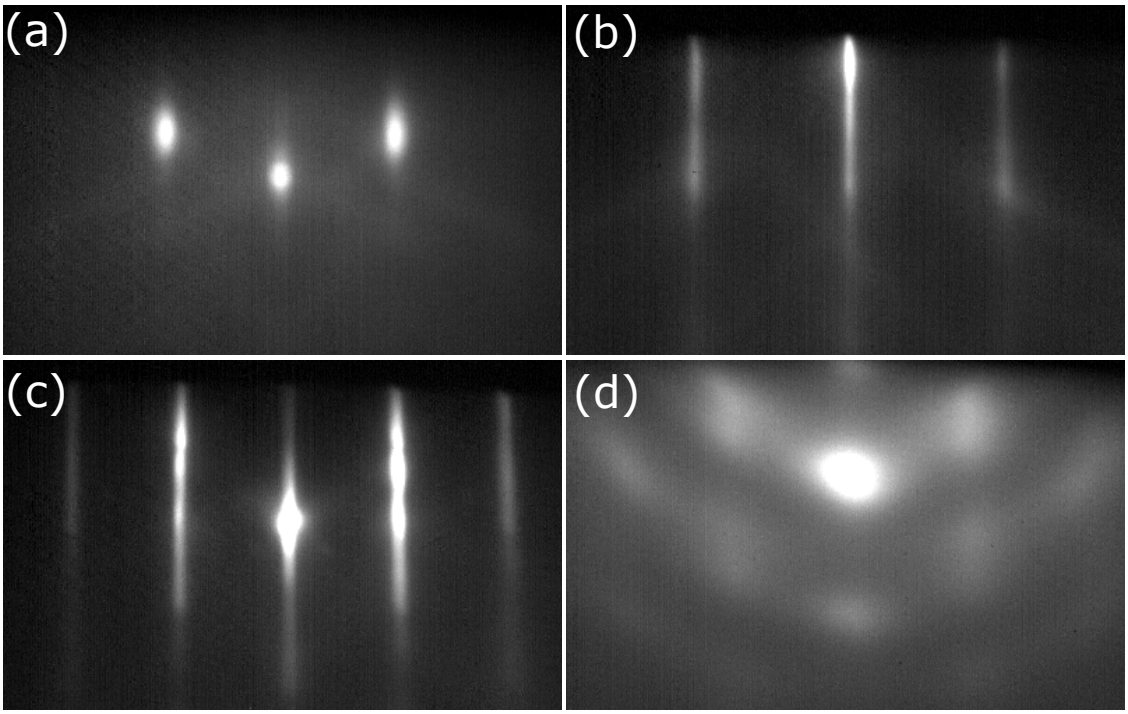

Figure 4.1: RHEED image of (a) clean and annealed YSZ(001) substrate along [110] azimuth. (b) and (c) RHEED images of the EuO(0 0 1) film grown at $p_{ox} = 1 \times 10^{-9}$ mbar along [1 0 0] and [1 1 0] azimuths, respectively. (d) RHEED image of polycrystalline film grown at $p_{ox} = 5 \times 10^{-9}$ mbar that contains multiple oxide phases.

(USA) was sublimated from an effusion cell with pyrolytic boron nitride crucible for producing a steady flux of Eu atoms. Molecular oxygen of high purity (99.999%) was used and its partial pressure in the growth chamber was controlled via a leak valve. The sample temperature was kept at 400° C and $p_{ox} = 1 \times 10^{-9}$ mbar during the growth. The Eu deposition rate was 8 Å per minute. A few monolayers of Eu metal were deposited on the substrate prior to the admission of molecular oxygen. These metal layers are oxidized by the oxygen atoms diffusing from the substrate. This step was found to be crucial for decreasing the amount of Eu_xO_y at the interface that inevitably forms because of the high mobility of oxygen atoms in the YSZ crystal. The epitaxial stabilisation of stoichiometric EuO is a balancing act between the amount of Eu atoms and O atoms at the substrate. Any increase in the oxygen partial pressure beyond the threshold limit of 2×10^{-9} mbar results in the formation of other oxide phases of europium such as Eu_2O_3 or Eu_3O_4. On the other hand, EuO is known to accommodate Eu atoms in interstitial positions, or in oxygen vacancies that drastically affect its physical properties. To avoid such excess of Eu metal in the lattice, EuO was grown with the maximum possible oxygen partial pressure at a certain Eu deposition rate and sample temperature. A main shutter in the growth chamber that is located directly in front of the substrate was opened to initiate

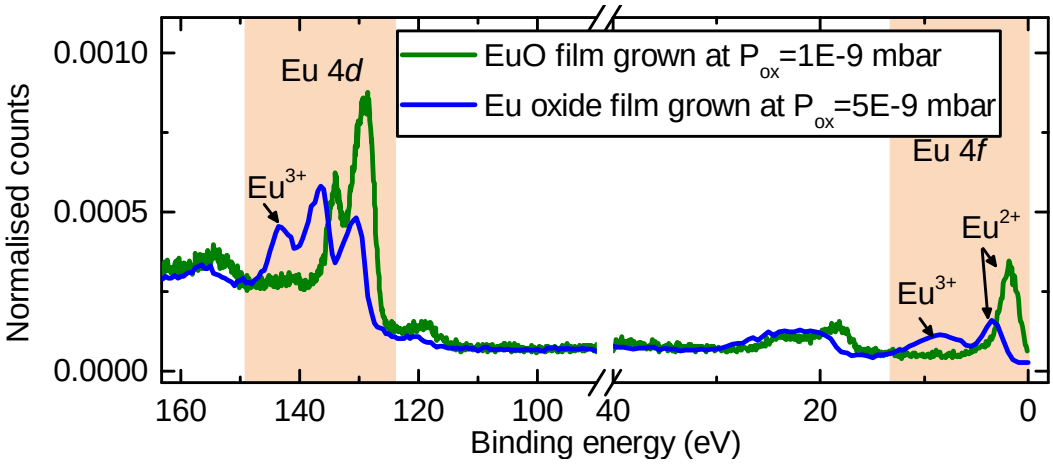

Figure 4.2: Valence band XPS of stoichiometric EuO grown at $p_{ox} = 1 \times 10^{-9}$ mbar (green line) and that of non-stoichiometric oxide grown at $p_{ox} = 5 \times 10^{-9}$ mbar (blue line) that contains a mixture of different europium oxide phases.

growth only after a stable oxygen partial pressure was achieved with the europium source shutter open. The growth was terminated by simultaneously terminating the oxygen supply and closing the main shutter. These are fine but important details for achieving EuO films of high phase purity.

The samples were characterized *in situ* by RHEED and XPS. The RHEED images of the clean YSZ substrate after annealing along [1 1 0] azimuth, the EuO film along [1 1 0] and [1 0 0] azimuth, and that of non-stoichiometric europium oxide are shown in the figure 4.1. The low background and sharp streaks in the RHEED images of EuO film grown at $p_{ox} = 1 \times 10^{-9}$ mbar (figure 4.1(b) and (c)) confirms the formation of a rather flat and single crystalline surface. The lattice spacing obtained from the RHEED image for EuO film along [1 1 0] and [1 0 0] are 3.5 ± 0.1 Å and 2.4±0.1 Å . These values are similar to the published YSZ lattice spacings ($d_{YSZ[110]}$= 3.63 Å) [116] and are in good agreement with the standardized crystal structure of EuO, proving the EuO[001]||YSZ[001] epitaxial relation [48]. Figure 4.1(d) shows a typical RHEED image of films grown with oxygen pressure larger than, or equal to $p_{ox} = 5 \times 10^{-9}$ mbar that results in the formation of mixed oxides. The appearance of Laue rings shows a reduction in single crystalline quality that mainly arises from the formation of a mixture of other polycrystalline oxide phases. The narrow growth window along with its affinity to oxygen makes the growth of EuO highly unstable against formation of Eu_3O_4 or Eu_2O_3. Determination of the oxidation state of Eu atoms in the sample is crucial for the confirmation of the phase purity. Eu atoms have 2+ oxidation state in EuO, while the other oxide phases have partial contribution from Eu^{3+} states. The chemical state of the Eu atoms was determined using valence band XPS collected at normal emission using an Al anode as the x-ray source. Figure 4.2 shows the XPS spectra of EuO films grown at two different oxy-

gen partial pressures that demonstrates the effect of oxygen partial pressure on the stoichiometry of the film. The critical partial pressure of oxygen was found to be 1×10^{-9} mbar, above which other oxide phases starts to form in addition to EuO. The oxidation state of Eu atoms have the most pronounced effect on the binding energy of the Eu $4f$ and $4d$ electrons. Figure 4.2 shows that as the oxygen partial pressure is increased beyond the critical oxygen pressure, the peak that corresponds to Eu $4f$ electrons develops a shoulder towards higher binding energies. A similar behavior is observed in the peak corresponding to the Eu $4d$ electrons. This is most likely due to the formation of Eu_3O_4 that has Eu atoms with mixed oxidation states of 2+ and 3+. Additionally, the EuO samples that are contaminated by other oxide phases are predominantly insulating in nature and their XPS spectra tend to be up-shifted in energy by a few eV due to electrostatic charging during the measurement. Such an up-shift is clearly visible in figure 4.2.

After the *in situ* surface characterization, the sample was capped with 10 nm thick Nb layer to prevent oxidation on exposure to air. In order to further characterize the stoichiometry and structural quality, the film was subjected to x-ray

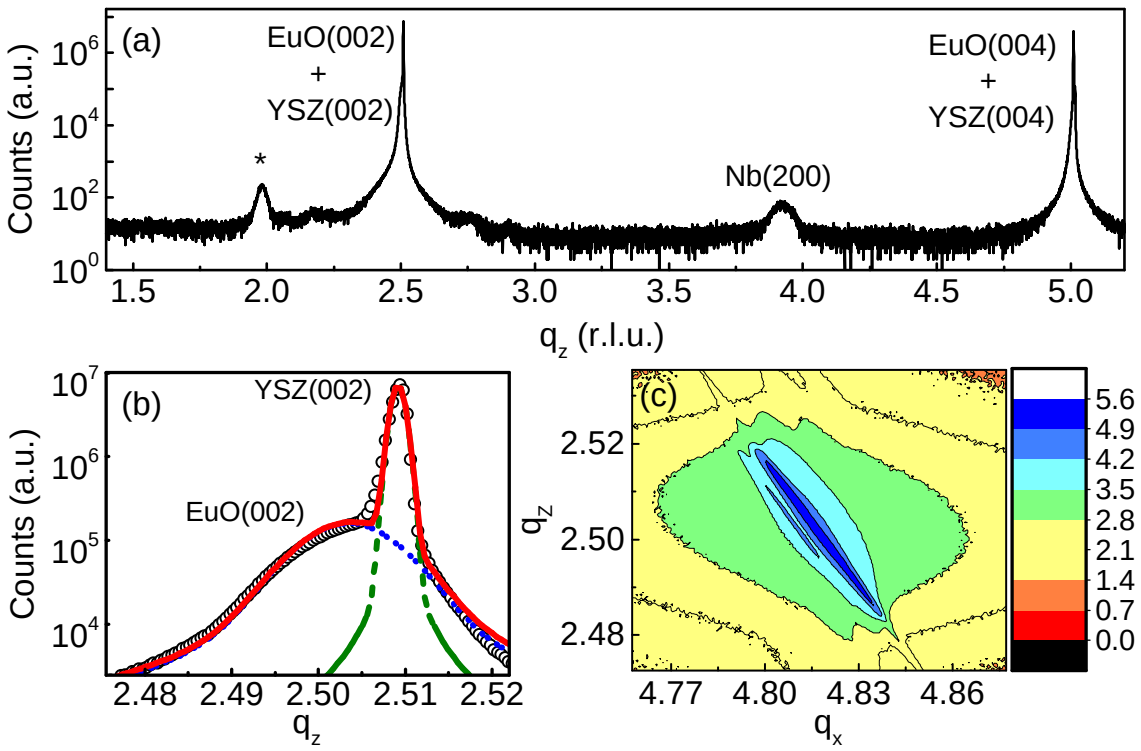

Figure 4.3: (a) XRD scan on the Nb capped 100 nm thick EuO(001) film on YSZ(001) [118]. (*) corresponds to another europium oxide phase formed at the EuO-YSZ interface. (b) High resolution XRD scan performed around the EuO(002) peak. The contributions from the EuO film and the YSZ substrate are plotted with dotted/blue and dashed/green lines, respectively. (b) Reciprocal space map around the EuO(002) peak.

diffraction (XRD) studies. The experiments were performed using a Rigaku SmartLab x-ray diffractometer with a rotating anode x-ray generator with Cu anode. Figure 4.3(a) shows XRD scan of the EuO(0 0 1) film grown on YSZ(0 0 1). Due to the identical crystal structure as well as the very similar lattice spacings, the XRD peaks of the substrate and the film overlap. Figure 4.3(b) depicts a high resolution XRD scan around the EuO(0 0 2) and YSZ(0 0 2) peaks. The peaks were fitted with two Voigt profiles to extract their positions and full width at half maximuma(FWHM). The FWHM values of the film and substrate were found to be 0.17° and 0.03° respectively. The greater FWHM of the film compared to the substrate indicates the presence of imperfections in the film. Additionally, figure 4.3(c) shows the reciprocal space map of the sample around the EuO(002) peak. The main features such as (0 0 2) reflection and the crystal truncation rod (parallel to q_z axis) are dominated by the signal from the substrate, the narrow feature next to bright spot in the middle corresponds to the EuO film. The out of plane lattice spacing calculated from the XRD data is 5.15 ± 0.01 Å and is similar to the published value (5.142 Å) of bulk EuO [117]. The contributions from the Nb capping layer at q=3.88 r.l.u and that of a higher Eu oxide at q=1.98 r.l.u. are also visible in the XRD scan. The intensity of this reflection was found to be inversely proportional to the amount of Eu metal deposited in the initial stage of growth prior to the admission of molecular oxygen. Also taking into consideration the fact that any presence of higher oxide was not observed in the surface sensitive XPS data we conclude that this higher oxide is located at the interface between the EuO film and the substrate. In addition, the area of this peak is less than 1% of the area of the EuO(0 0 2) reflection from the film, therefore it can be safely neglected.

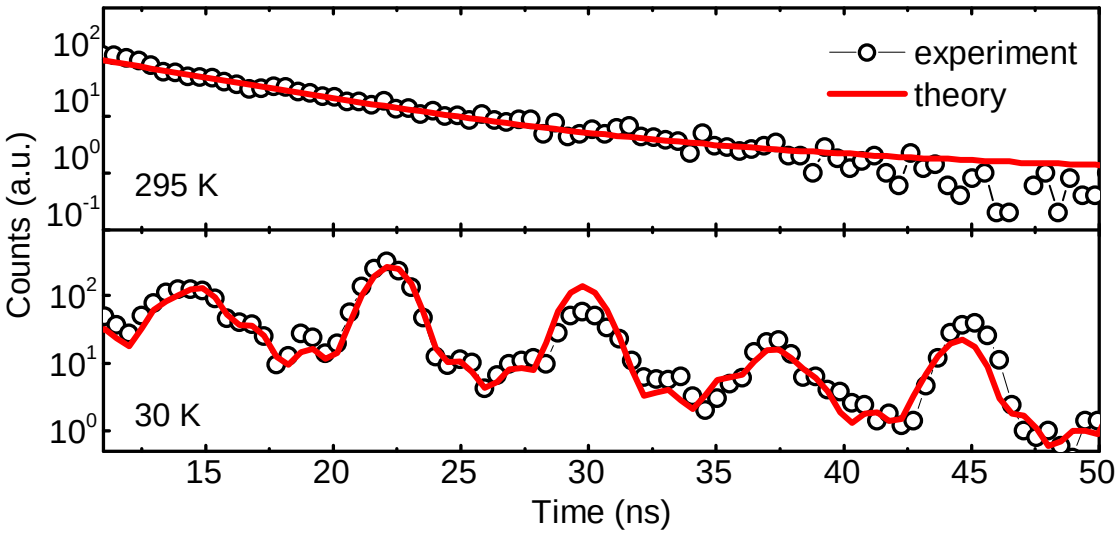

Figure 4.4: NFS spectra of EuO film at grazing incidence (black/open circles) and the fits (red/solid lines) at the indicated temperatures [118].

As discussed earlier, the presence of excess Eu atoms could result in different physical properties such as an enhanced T_C and insulator-to-metal transition. Such physical effects of non-stoichimetric EuO will influence the lattice dynamics of the crystal and ultimately will lead to erroneous conclusions. In order to exclude the presence of excess Eu, the nuclear forward scattering spectra was collected at room temperature and at 30 K, see figure 4.4. The extremely sensitive nature of the NFS signal to the chemical environment of the Mössbauer-active element, serves as the ultimate test for presence of chemically non-equivalent Eu atoms in the sample. The nuclear forward scattering data was fitted (solid/red line) using REFTIM code [57]. The input file for the fitting model and nuclear properties of the Eu^{151} isotope is given in the appendix. Figure 4.4(a) shows the absence of any quantum beats at room temperature, confirming that all Eu atoms in the sample have an equivalent chemical state of Eu^{2+}. The characteristic quantum beats due to magnetic hyperfine splitting visible in the NFS spectrum measured at 30 K (figure 4.4(b)) demonstrates the ferromagnetic order in the sample. A net magnetic field of 27.3 T is derived from the fit, that is characteristic for stoichiometric EuO at this temperature [119].

4.2 Lattice dynamics

4.2.1 *Ab initio* approach

The first principles calculations were performed by our collaborating partner Dr. habil. Przemisław Piekarz from the Institute of Nuclear Physics in Krakow, Poland[1]. The calculated phonon DOS and phonon dispersion curves are shown figure 4.8.

4.2.2 Inelastic x-ray scattering: phonon dispersion relations

Phonon dispersion relations above and below the Curie temperature were measured by the inelastic x-ray scattering (IXS) experiment. Grazing incidence temperature dependent IXS experiment was performed on beamline ID28 of the ESRF. The

[1]Density functional theory was used to calculate the lattice dynamics of EuO. The electronic structure was optimized within the projector augmented-wave method [45] and the generalized-gradient approximation (GGA) [39] implemented in the VASP software [44]. A strong local Hubbard interaction ($U_f = 8.3$ eV, $U_p = 4.6$ eV) and Hunds exchange ($J_f = 0.77$ eV, $J_p = 1.2$ eV) [120] were inluded for the Eu($4f$) and O($2p$) states using the GGA+U method [121]. The optimized lattice parameter $a = 5.16$ Å corresponds well to the measured value 5.14 Å and the calculated $4f$-$5d$ band gap of 1.05 eV agrees with the experimental value of 1.12 eV [122]. The phonon density of states (DOS) and phonon dispersions (Fig. 4.8) were calculated using the direct method [43]. The Hellmann-Feynman forces were obtained by displacing non-equivalent atoms from their equilibrium positions to determine the force constants and dynamical matrices. Phonon energies and polarization vectors at a given wave vector follow from the exact diagonalization of the dynamical matrix.

incident x-rays with an energy of 17.794 keV were monochromatised to FWHM = 3 meV by a Si(9 9 9) monochromator working in nearly backscattering geometry. The theoretical background and the experimental setup of the IXS experiment are described in section 2.2.6. The sample was measured under vacuum ($\approx 1 \times 10^{-6}$ mbar) in a helium flow cryostat equipped with kapton foil windows for the x-ray beam access.

The phonon dispersion relations along Γ-X and Γ-K-X direction were measured at room temperature and at 40K. Additionally, phonons along the Γ-X direction were also measured at 90 K. A schematic diagram representing the momentum transfer directions is shown in figure 4.5. The incident grazing angle (0.2°) was chosen to be larger than the critical angle (0.16°) in order to reduce the contribution of the Nb capping layer and to optimize the x-ray penetration into the EuO film. The direction and size of the momentum transfer $\vec{q}$ were selected by an appropriate choice of the scattering angle and sample orientation in the horizontal scattering plane. The choice of the Brillouin zone and the energy transfer was aided by the *ab initio* calculations. Due to the grazing incidence geometry, the momentum transfer has an inevitable but small out-of-plane component ($q_z \approx 0.1$ r.l.u.) that had some implications on the measurements, as discussed below. Figure 4.5 summarizes the direction, polarization and total momentum transfer of the investigated phonon branches.

The energy of the scattered photons was analysed by nine Si analysers mounted in a pseudo Rowland geometry before impinging on the detector. From the IXS spectra, the phonon energies and linewidths (FWHM) were precisely determined by

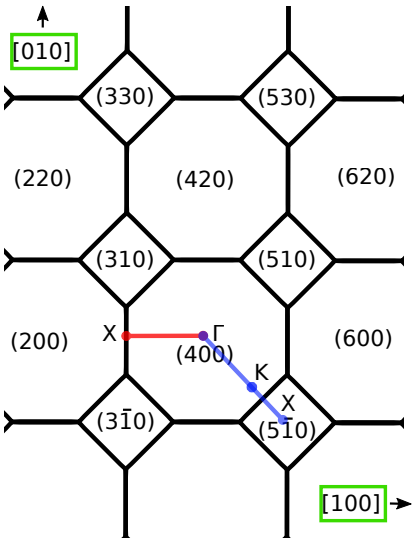

Direction	Mode	Momentum transfer
Γ-X	LA	[4-ζ, 0, 0.1] (0.2≤ ζ ≤1)
Γ-X	TA	[4, -ζ, 0.1] (0.2≤ ζ ≤1)
Γ-K-X	LA & TA	[4+ζ, -ζ, 0.1] (0.2≤ ζ ≤1)

Figure 4.5: (a) The two-dimensional extended Brillouin zone depicting the directions in the reciprocal space where IXS measurements were performed. The table summarizes the direction, phonon polarisation and momentum transfer of the IXS measurements.

using a model function consisting of a superposition of damped harmonic oscillator profiles. The detailed balance of the model was taken into account by the Bose factor. The central elastic peak was estimated with a Lorentzian profile. This function was then convoluted with the experimentally determined resolution function and numerically fitted to the IXS spectra using a χ^2 minimization routine. This mathematical processing was performed using FIT28 software available at ID28 beamline of the ESRF.

The IXS spectra were collected in two different grazing incidence sample orientations optimized for excitation of predominantly either the transverse acoustic (TA) or the longitudinal acoustic (LA) phonon modes in the EuO(001) film. However, due to the unavoidable offset in the q_z direction (≈ 0.1 r.l.u.), a contribution of the LA and TA phonons were observed in both cases. Figure 4.6 and figure 4.7 shows the energy IXS scans along Γ-X direction for probing TA and LA phonons, respectively. The energy scans are arranged in three different columns based on the measurement temperature and each row corresponds to a single momentum transfer. For a precise disentanglement and determination of the positions and linewidths of the phonon excitations at low temperatures, the following strategy was employed. The IXS spectra for LA phonon modes, see figure 4.7, were first fitted using the procedure described above, keeping all the fit parameters of the excitations unconstrained. The FWHMs of the LA modes thus obtained were kept constants while performing the fit of the TA modes. An exception from this fitting procedure was made for the transverse phonons at $q = 0.8$ and 1 that was measured at 90 K. The FWHMs were limited to 9.0 meV and 10.0 meV, respectively, to obtain the best fit of the phonon excitation, see figure 4.6(g) and (h). In IXS spectra with energy transfers larger than 25 meV, weak contributions from the optic phonons in the EuO(0 0 1) film and the acoustic phonons in the YSZ(001) substrate are visible, see figure 4.7(h-l).

Figure 4.8(b) shows the excellent agreement between *ab initio* calculated phonon dispersion relations (solid lines) and the experimentally determined phonon energies at different temperatures by the above described procedure. The energies of almost all phonon modes remains fairly temperature independent except for a softening ($\Delta E \approx 21\%$) of the TA modes near the zone boundary along Γ-X direction in the vicinity of the Curie temperature and below. Since the IXS crossection is proportional to the atomic number, the scattering from the O atoms that makes up the optical branches were too weak to be reliably detected.

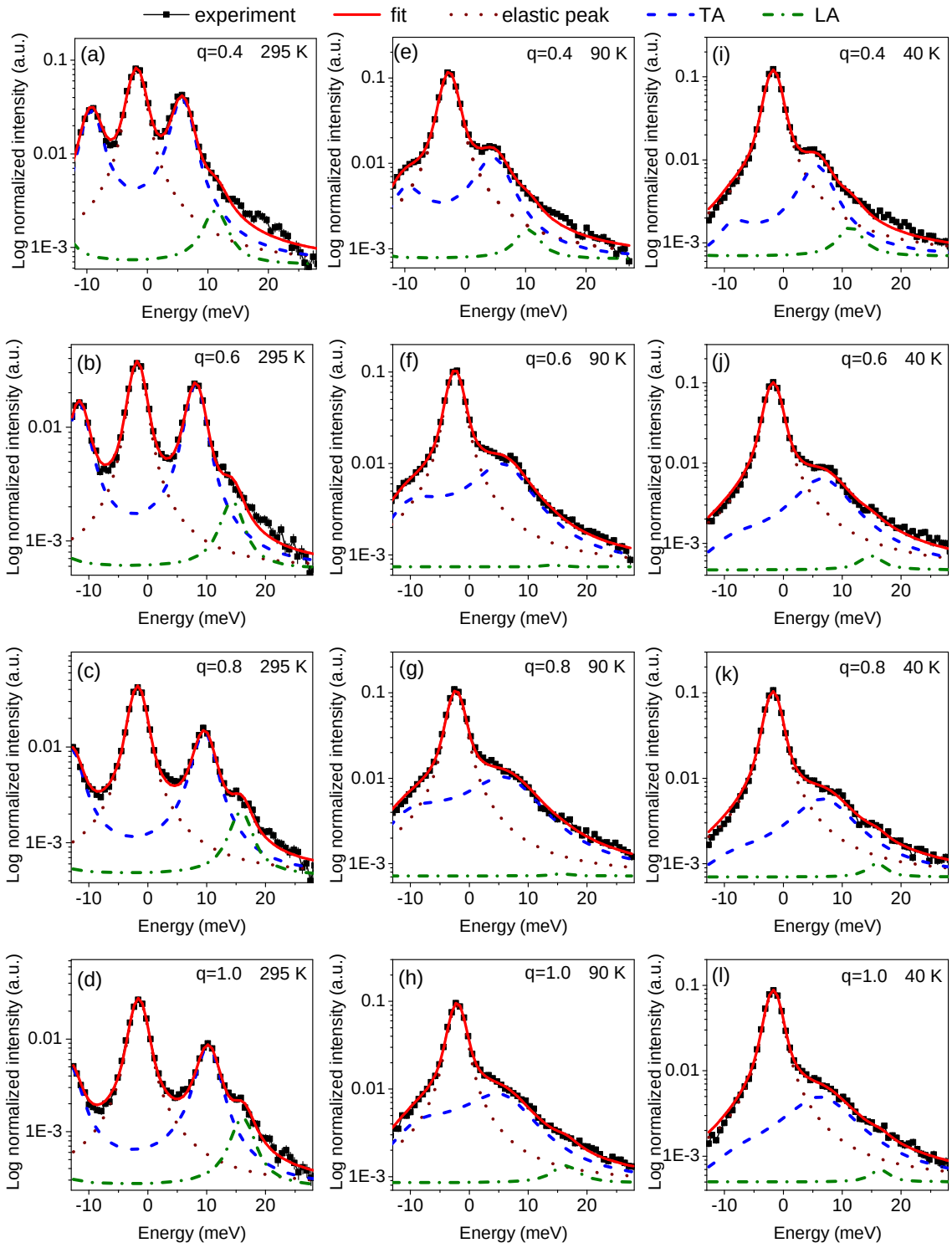

Figure 4.6: IXS spectra obtained in a scattering geometry optimized for measuring the TA phonon modes with momentum transfer along Γ-X direction at 295 K (a-d), 90 K (e-h) and 40 K (i-l). The momentum transfer values and temperatures are indicated in each plot [118].

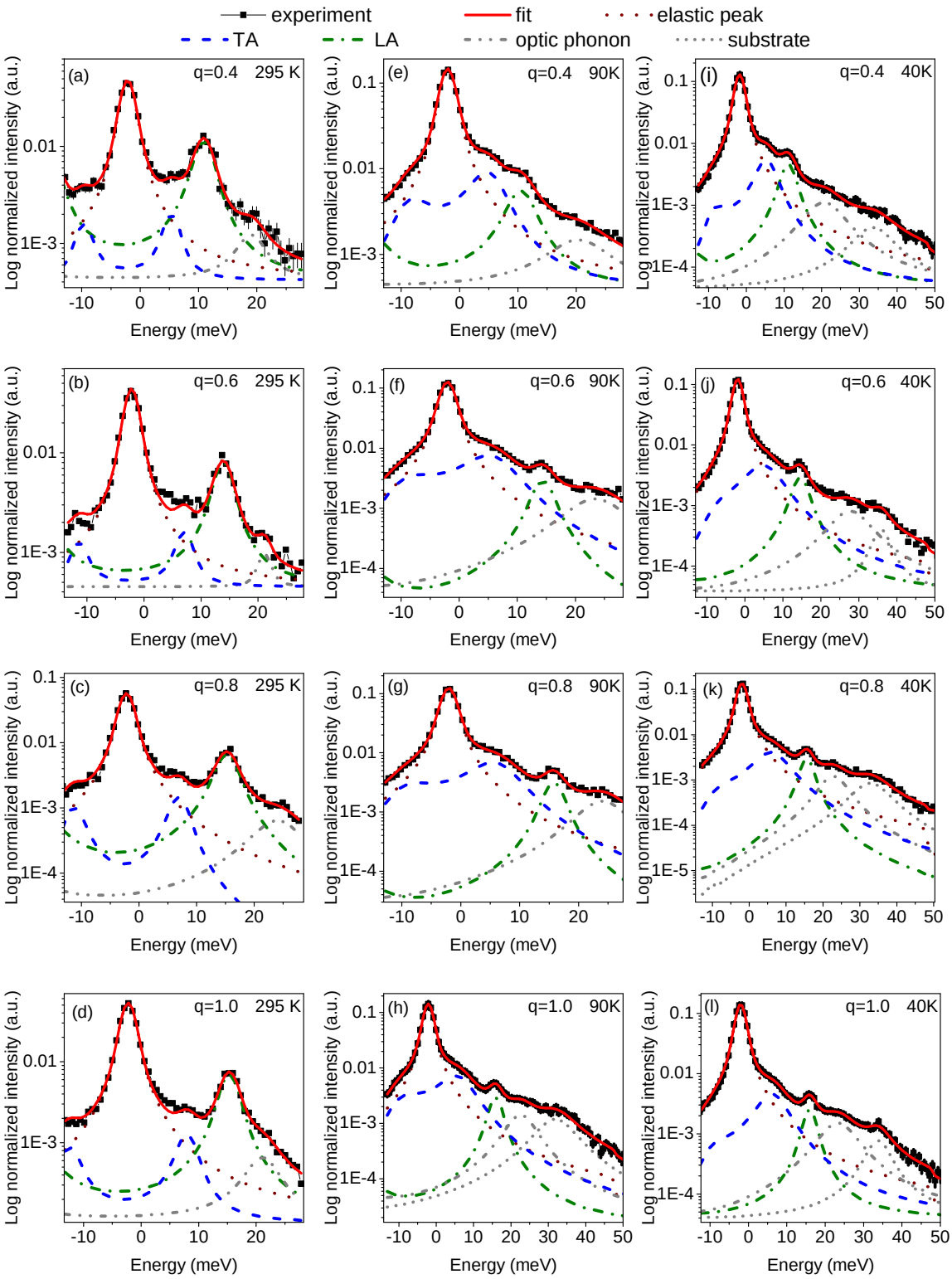

Figure 4.7: IXS spectra obtained in a scattering geometry optimized for measuring the LA phonon modes with momentum transfer along Γ-X direction at 295 K (a-d), 90 K (e-h) and 40 K (i-l). The momentum transfer values and temperatures are indicated in each plot [118].

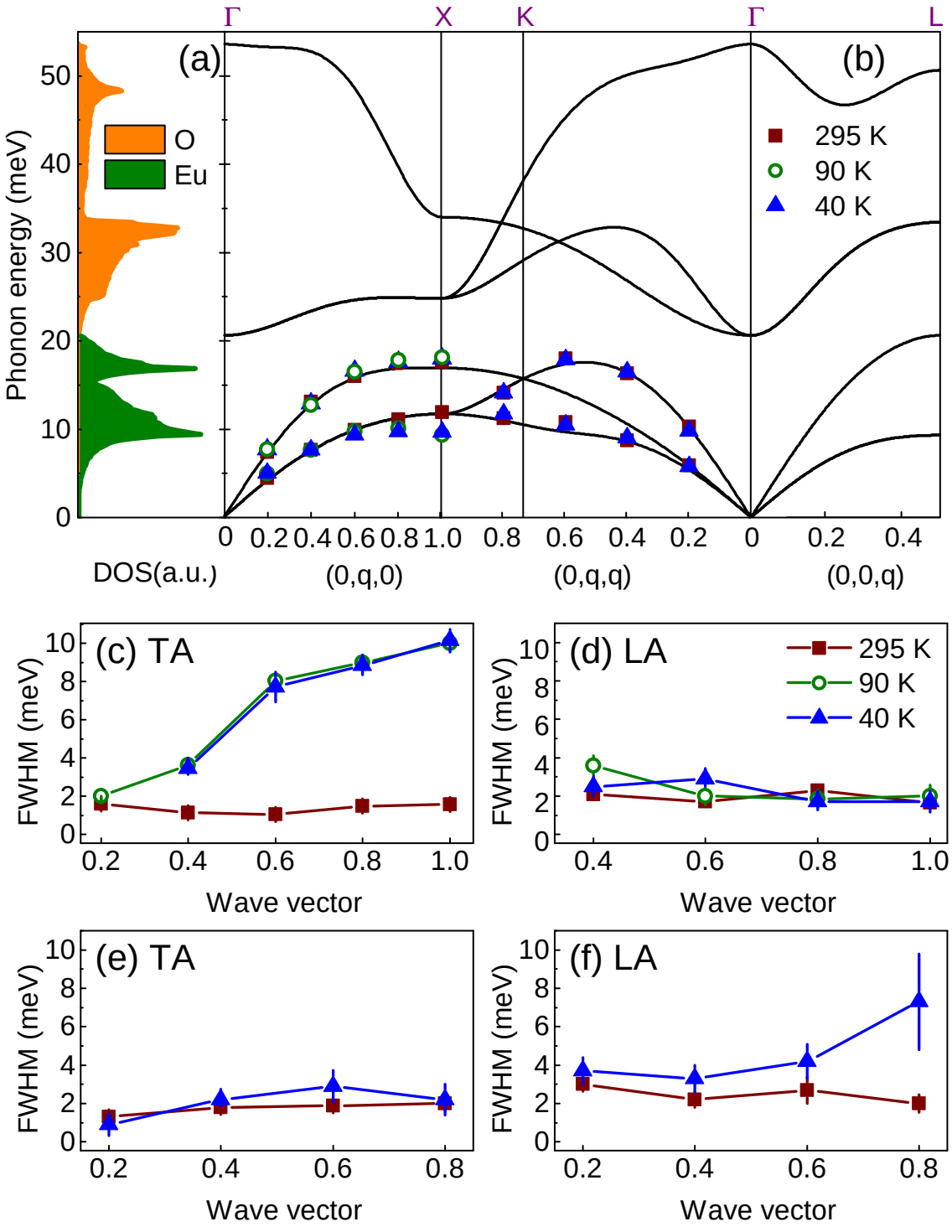

Figure 4.8: (a) The *ab initio* calculated phonon DOS of EuO. The partial contributions of the Eu and O atoms to the phonon DOS are indicated. (b) Phonon dispersion relations from *ab initio* calculations (lines) and IXS experiment (points) at 295, 90 and 40 K. (c,d) FWHMs as a function of momentum transfer for the TA and LA branches along the Γ-X direction at 295, 90 and 40 K. (e,f) FWHMs for the TA and LA branches along Γ-K-X direction at 295 and 40 K [118].

The analysis of the IXS spectra reveal a remarkable and unusual behaviour of the phonon linewidths. The FWHMs derived from the fit to the experimental data are plotted as a function of momentum transfer for the TA and LA branches along the Γ-X and Γ-K-X directions in figures 4.8(c,d) and 4.8(e,f), respectively. The FWHMs of the TA and LA modes along all the measured directions at room temperature remain weakly q-dependent throughout the entire Brillouin zone. However, the TA modes along the Γ-X direction at $T = 90\,\mathrm{K}$ and below show the largest q-dependent linewidth broadening (figure. 4.8(c)). In fact, the phonon linewidth at the zone boundary increases by a factor of five from that measured at room temperature. Additionally, a weakly q-dependent broadening of the LA phonon modes along Γ-K-X is observed, see figure 4.8(d). In contrast to the Γ-X direction, the increase of the FWHMs for $q \leq 0.6$ is only by a factor of 1.6 with respect to that measured at room temperature with a clear tendency to increase towards the X point. At the same time the widths of the LA and TA branches along Γ-X and Γ-K-X, respectively, remain temperature independent within the error bars, see figure 4.8(d,e). The broadening of phonon linewidth suggests that in EuO the phonon lifetimes are tremendously reduced near the vicinity of T_C and in the ferromagnetic state. Such temperature dependent trend indicates the possible effect of magnetism on the lattice vibrations.

4.2.3 Nuclear inelastic scattering: phonon DOS

The Eu-partial phonon DOS was determined by an *ex situ* temperature dependent NIS experiment performed at the Nuclear Resonance beamline ID18 of the ESRF. The sample was fabricated and characterized in the UHV Analysis laboratory of ANKA, KIT. The sample had specifications similar to the one used for the IXS experiment, 10 nm of Nb capped 100 nm thick EuO(001) film on YSZ(001). The sample was mounted in a He flow cryostat with Kapton foil windows for x-ray access. The NIS experiment was performed across the Curie temperature, specifically at 295 K, 90 K, 70 K, 50 K and 30 K. The incident photon beam was parallel to the EuO[100] direction for obtaining the phonon DOS projected along the direction that showed the largest temperature dependent effects. In the NIS experiment the incident energy of the photons was tuned in the vicinity of the resonant transition energy (21.54 keV) of the ^{151}Eu nuclei with an energy resolution of 1.1 meV [123]. An optimum x-ray penetration depth and the elastic signal in the forward direction (instrumental function) were achieved by selecting an incident angle $\approx 0.2^\circ$ that is slightly above the critical angle ($\approx 0.14^\circ$) for this particular energy. Figure 4.9 shows the cumulative NIS spectra obtained at the indicated temperatures. The NIS spectra already show the main features of the DOS at 11 meV and 17 meV.

Following the procedure described in section 2.2.5, temperature dependent Eu partial phonon density of states projected along EuO[1 0 0] were extracted from NIS data collected at different temperatures. The result is plotted along with *ab initio*

calculated DOS in figure 4.10. In order to compare the theoretical and experimental results, the *ab initio* calculated DOS was convoluted with a Gaussian profile of width 1.5 meV to account for the effect of the instrumental function (shaded area). Figure 4.10(a) shows the Eu partial phonon DOS measured as a function of temperature along with the calculated DOS. The spectra are given an offset of 0.05 meV^{-1} along the Y axis for better visibility. The Eu partial phonon DOS of EuO has two main peaks at around 11 meV and 17 eV that are mainly constituted by the TA and LA modes, respectively. The experimental phonon DOS shows an overall good agreement with the *ab initio* calculated DOS convoluted with the Gaussian curve. On the other hand, the peak at 11 meV that corresponds to the TA modes shows a broadening effect towards lower temperatures. In order to quantify the broadening phenomenon, these peaks were modelled as a combination of two Voigt profiles (dashed lines) and the derived FWHMs are plotted in figure 4.10(b,c) as a function of temperature. The peak that corresponds to the TA modes broadens by 17% at 30 K when compared to the room temperature measurement, while the peak that correspond to the LA modes remain fairly temperature independent, which is in qualitative agreement with the IXS results. However, a direct quantitative comparison of the phonon linewidths obtained by IXS and NIS will be erroneous since the latter gives the momentum averaged and combined contributions from the LA and TA branches.

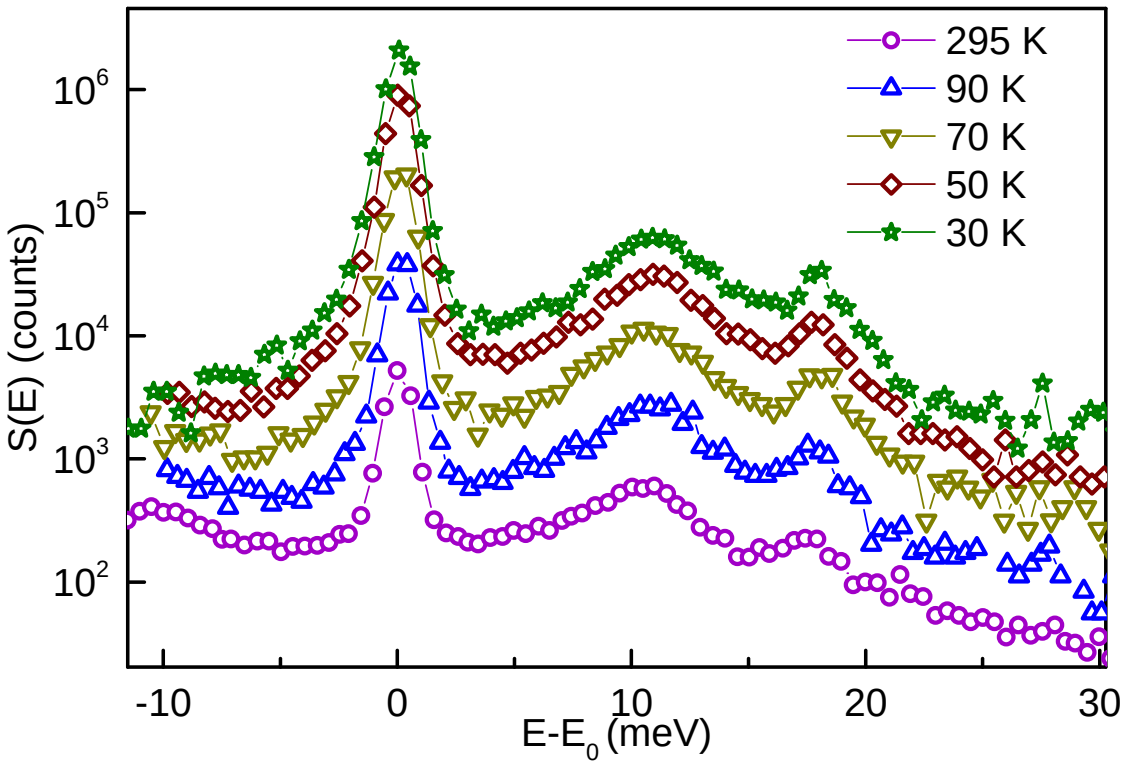

Figure 4.9: The cumulative NIS spectra of the EuO film obtained at the indicated temperatures.

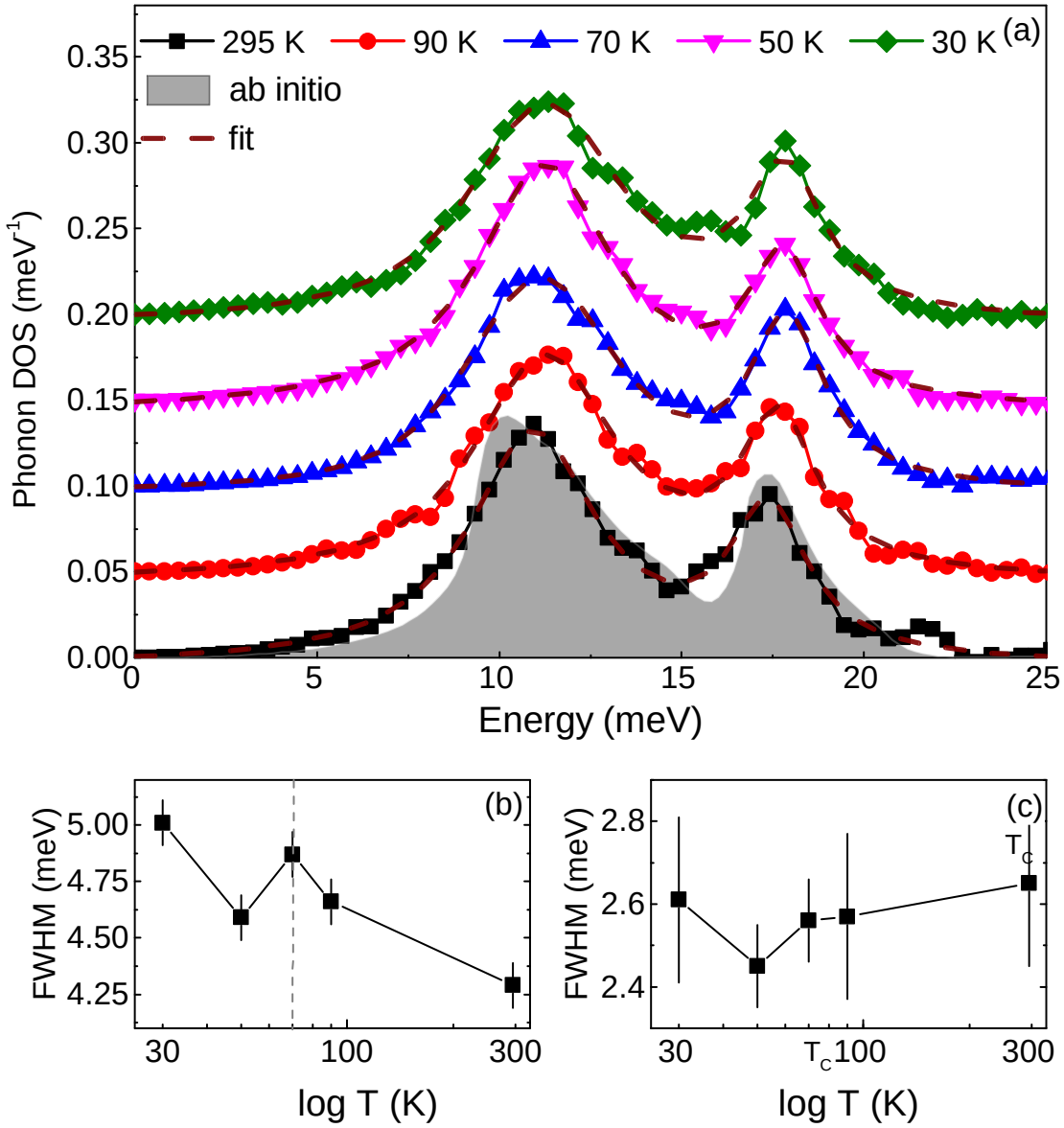

Figure 4.10: a) The Eu-partial phonon DOS in EuO obtained from the NIS experiment at the indicated temperatures. The spectra are up shifted by 0.05 meV^{-1} for clarity. The *ab initio* calculated Eu-partial phonon DOS, convoluted with a Gaussian curve of FWHM=1.5 meV, is depicted as the shaded area. The dashed line stands for the fit of the experimental data with a combination of two Voigt profiles. The FWHM as a function of temperature for phonon peaks at: (b) 11 meV, and (c) 17 meV. The solid lines are guide to the eye [118].

4.2.4 Thermodynamic and elastic properties

From the phonon density of states the thermodynamic and elastic properties such as vibrational entropys S_{vib}, lattice specific heat C_v, mean force constants K, vibrational amplitude, Lamb-Mössbauer factor etc. can be calculated, as described in section 2.1.3. The temperature dependent evolution of selected thermoelastic properties deduced from the *ab initio* calculated and measured Eu-partial phonon DOS of EuO is shown in figure 4.11. An excellent agreement between theory and experiment for the vibrational entropy and lattice specific heat is clearly visible. Anomalous increase in the lattice specific heat near the magnetic phase transition was not detected, implying that the anomaly observed by calorimetric experiments [124, 125] is not connected to the lattice excitations but arises from the magnetic contribution to the specific heat capacity [126]. The existance of a sharp reduction in the thermal conductivity of EuO around T_C is debated [127, 128]. The absence of the critical behavior in C_v determined from the phonon DOS at 70 K tends to agree with absence of critical behviour in the thermal conductivity [127]. The normalized force constant K remains temperature independent within the error limits hinting the absence of any significant anharmonicity in the crystal.

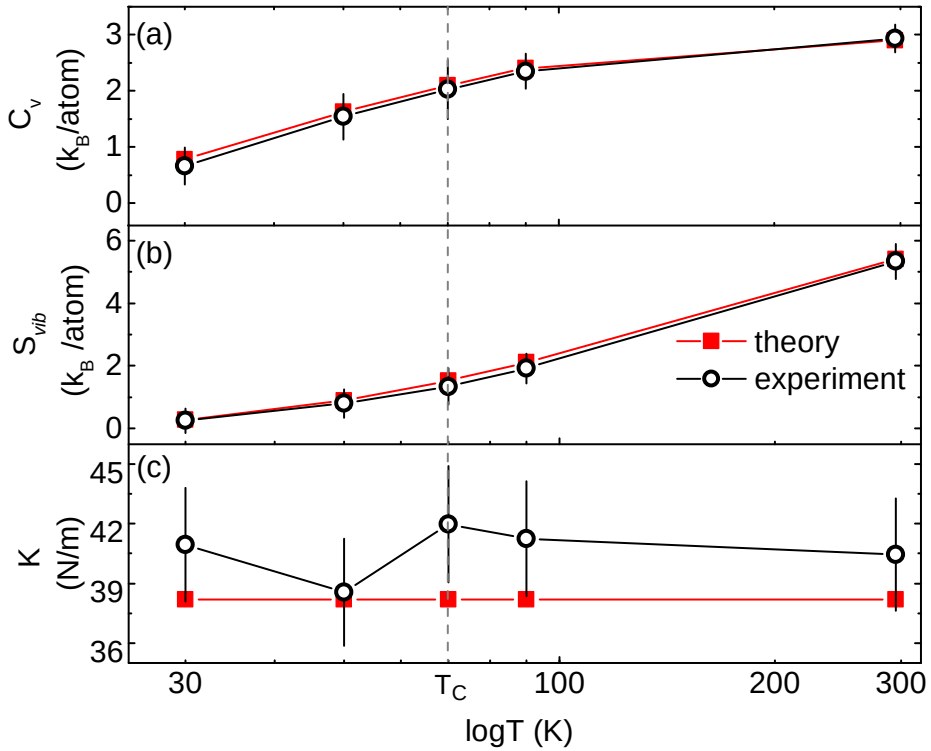

Figure 4.11: The experimental and theoretical temperature dependences of the Eu-partial: (a) vibrational entropy S_{vib}, (b) lattice specific heat C_v, and (c) mean force constant K [118].

4.2.5 Spin-phonon coupling

The phonon linewidth increase near and below the Curie temperature obtained via two mutally exclusive experimental methods, IXS and NIS is surprising and in contrast to the usual decrease of phonon linewidths with decreasing temperature [129]. The inverse temperature dependence of the phonon linewidths suggests a physical phenomenon that neither originates from the phonon-phonon scattering processes, nor from scattering from defects. The bosonic nature of the phonons imply that at low temperatures the number of phonons in the system should be less than that at room temperature, which in turn should reduce the magnitude of phonon-phonon interactions. An IXS experiment on BeO has demonstrated that anharmonicity in the crystal structure could lead to momentum dependence of the phonon linewidths [130]. The first proof for the absence of anharmonic behavior in EuO is given from the temperature independence of the mean force constants obtained from the DOS (figure 4.11(c)). Additionally, the Hellmann-Feynman forces and phonon dispersion relations were calculated assuming two independent sets of displacements with amplitudes u= 0.03 Å and 0.06 Å. Figure 4.12 demonstrates that the calculated phonon energies vary negligibly with respect to the assumed atomic displacements indicating the absence of significant anharmonicity in EuO. The observed anomalous temperture behaviour of the linewidths could also arise from epitaxial strain in the thin films [131]. The YSZ substrate and EuO have an identical crystal structure and the difference in lattice parameters derived from the XRD measurement is merely 0.04%, implying that YSZ provides a nearly strain-free template for the epitaxial growth of EuO. Moreover, the thin layer of higher oxide formed at the interface, as discussed in section 4.1, shields the EuO film from epi-strain propagating from the substrate at low temperatures that could possibly arise from the difference in lattice thermal expansion coefficients of the EuO film and the YSZ substrate. Therefore, phonon-phonon scattering, defect induced scattering, anharmonicity, and epitaxially induced strain could be safely excluded as physical mechanisms behind the observed phenomenon.

The temperature dependence of the phonon linewidth suggests that it is related to the effect of the evolution of magnetism in the crystal. Inelastic neutron scattering experiments have already proven the existence of finite spin correlations above T_C up to 115 K [90, 132, 133]. Well-defined but heavily damped spin waves above T_C at the zone boundaries, mediated by exchange between nearest and next-nearest neighbor Eu ions, have been experimentally observed [90, 132] and theoretically confirmed [134], similar to Fe [135], Ni [136], and double perovskites [137]. The measured spin waves in EuO also showed an increasing linewidths towards the zone boundary and were not accurately described most likely because their scattering from phonons was not considered. Early Raman scattering experiments reported a shift in the fundamental frequency of the scattered light as a function of sample temperature

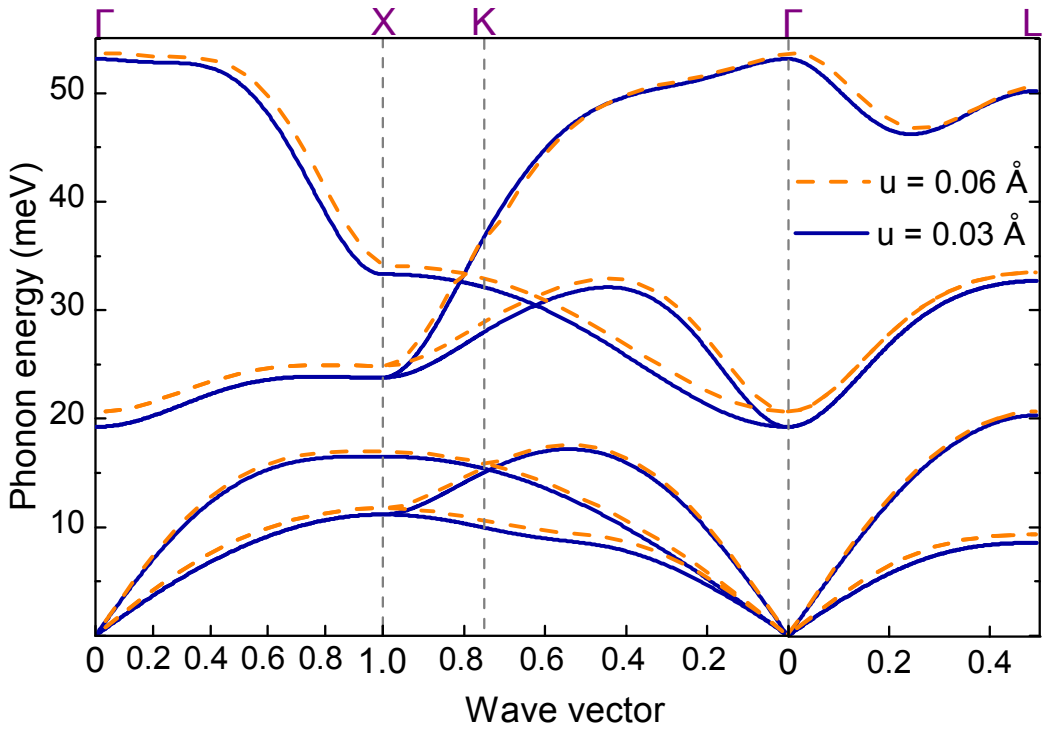

Figure 4.12: *Ab initio* calculated phonon dispersion relations of EuO for the indicated atomic displacements [118].

that was attributed to a coupling of spin waves to phonons [114, 20, 21, 22]. On similar lines, the observed increase of phonon linewidths towards the zone boundary along Γ-X at 90 K is attributed to an enhanced scattering of phonons by short-range spin excitations. Figure 4.8 reveals that at 40 K, when the sample is in the ferromagnetic state, phonon linewidth broadening is observed for the TA modes along Γ-X with a similar magnitude as in the measurement at 90 K. Additionally, at the same temperature the LA modes along the Γ-K-X direction also show a finite phonon linewidth broadening. Spin waves were also experimentally measured in the ferromagnetic state of EuO [138]. Therefore, similar to the observations at 90 K, the strong interaction between spin waves and phonons are responsible for the increase of the phonon linewidth at 30 K. This is in agreement with the earlier acoustic measurements that reported an anomalous reduction of sound velocity below T_C that originates from strong coupling of spin fluctuations to acoustic phonons [139].

Furthermore, a theoretical study of magnon-phonon coupling in a Heisenberg ferromagnet showed that the force constants acting between the nearest-neighbor (NN) and next-nearest-neighbor (NNN) and their ratios play a decisive role in the spin-phonon coupling process [140]. For the TA modes the coupling is stronger towards the X point along Γ-X, while the LA modes couple more tightly to spin waves along Γ-K-X, provided that the force constants between the NNN are comparable to those acting between the NN. The force constant matrices from our *ab initio* calculation for EuO are presented below (in units amuTHz^2).

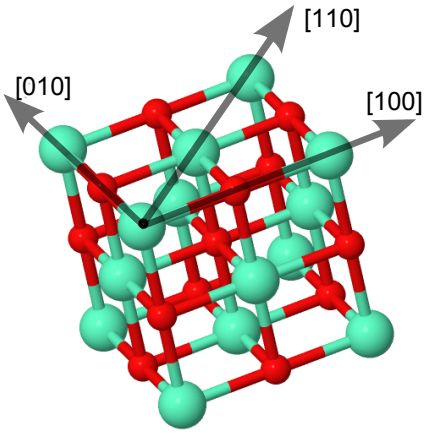

Direction	Atoms	Distance
[010] or Γ-X	Eu-O	2.57 Å
[110] or Γ-K-X	Eu-Eu	3.64 Å

Figure 4.13: The crystal structure and its main crystallographic directions in EuO. The Eu and O atoms are represented by green/larger and red/smaller spheres, respectively. The inset table shows interatomic distances along the investigated crystallographic directions (Source: adapted from www.icsd.fiz-karlsruhe.de) [118].

The force constants matrix between the NN atoms along [010] direction (Γ-X), i.e. between Eu and O atoms is:

$$VV_{NN} = \begin{bmatrix} -6507.83 & 0.00 & 0.00 \\ 0.00 & -1955.71 & 0.00 \\ 0.00 & 0.00 & -6507.83 \end{bmatrix}.$$

The force constants matrix between the NNN along [110] direction(Γ-K-X), i.e. between the two Eu atoms is:

$$VV_{NNN} = \begin{bmatrix} -5587.65 & -10287.46 & 0.00 \\ -10287.46 & -5587.65 & 0.00 \\ 0.00 & 0.00 & 3070.31 \end{bmatrix}.$$

There are off-diagonal elements in the NNN force constant matrix representing the in-plane x and y components. On average these matrix elements are larger than the elements of NN matrix. Especially, the diagonal (V_{xx} and V_{yy}) and off-diagonal (V_{xy} and V_{yx}) are much larger than the force constant V_{yy} for Eu-O. According to the calculations presented in reference [140], the stronger NNN force constant compared to the NN force constant is responsible for the relatively strong coupling of spin waves to the TA modes along Γ-X direction compared to the LA modes. In addition, the energies of the TA modes are closer to those of the spin waves (up to 6 meV [141]) compared to the LA modes. Even though the energies do not match exactly, they span a comparable range such that the momentum and energy conservation of the spin-phonon coupling process could be fulfilled. This explains the linewidth increase observed in the TA modes along the Γ-X direction (Fig 4.8(c)). On the contrary to the TA modes, the LA phonons show a broadening effect along

the Γ-K-X direction (Fig. 4.8(f)). This is due to the fact that these LA modes along Γ-K-X direction modulate the shortest Eu-Eu distance, thus affecting the magnetic exchange interaction between the localized $4f$ electrons. This effect is particularly strong at the zone boundary, where the NN atoms vibrate with opposite phases, which explains the increase of the phonon widths towards the X point.

In order to estimate the spin-phonon coupling constant α, the following relation is used [129]:

$$\Gamma \approx \frac{\hbar\omega z J'^2}{K}\chi_s''(\hbar\omega), \tag{4.1}$$

where Γ is the phonon width induced by spin fluctuations, $\hbar\omega$ is the phonon energy, z is the coordination number, J is the exchange coupling constant, K is the normalized force constant, and $J' = \alpha J/\text{Å}$ is the change of the exchange coupling constant J due to atomic displacement. For a paramagnet, $\chi_s''(\hbar\omega) \approx \hbar\omega(S/zJ)^2$. At low temperatures, Γ increases by $\approx 8\,\text{meV}$ at the X point compared to the room temperature values, and taking $S = 7/2$, $z = 6$, $\hbar\omega = 10\,\text{meV}$, $K = 2.5\,\text{eV/Å}^2$, the value for α is ≈ 10. This value is among the largest spin-phonon coupling constants observed in solids [142, 143, 144]. The spin-phonon coupling in EuO arises from the Heisenberg and s-f exchange interactions and assuming a value of $\alpha_H \approx 4$ for the Heisenberg term [145], the contribution of the s-f interaction amounts to $\alpha_{s-f} \approx 6$ [118].

4.3 Conclusions

The lattice dynamics of EuO is determined in a broad temperature range across the T_C by inelastic x-ray scattering, nuclear inelastic scattering and first-principles calculations. The calculated and experimentally determined phonon energies are in excellent agreement, proving that GGA+U method is very good approximation for describing electron correlations in strongly correlated systems like EuO. The experiments unambiguously reveal a remarkable broadening of the phonon linewidths at low temperatures, especially pronounced for the TA modes along the Γ-X direction. This is unexpected and implies a surprisingly strong spin-phonon coupling activated by spin fluctuations, which influences the electronic states and the lattice dynamics. The large spin-phonon coupling reported here seems to be the missing component for the accurate interpretation of the spin-wave linewidth dependence on temperature and momentum obtained by inelastic neutron scattering experiments [90, 134, 138]. Such strong coupling between magnetic, electric and atomic vibrations in materials pave the way towards the design of devices with new functionalities [144]. Moreover, the discovered anisotropic coupling discussed above is of relevance for the proposed application of EuO in spintronics. The results show that the magnitude of the spin-phonon coupling in EuO is smaller along the Γ-K-X than along the Γ-X direction,

implying that the choice of crystal orientation could be crucial for reducing the undesired spin-flips that could potentially reduce the degree of spin polarisation.

Chapter 5

Lattice dynamics of ultrathin EuO films

In order to investigate the influence of spatial confinement and broken translational symmetry at the surface on the lattice dynamics of EuO, thin films with thickness 1ML, 2MLs and 45MLs (ML stands for monolayer; 1ML = 1.71 Å) were epitaxially grown on $YAlO_3$ and characterized by x-ray and electron diffraction techniques. The lattice dynamics study of the EuO films in the paramagnetic regime was performed by a combination of ab initio calculations and temperature-dependent nuclear inelastic scattering in the range 300 - 130 K. The relevant thermodynamic and elastic properties of the EuO films were calculated from the phonon DOS and are presented in this chapter.

5.1 Sample preparation and characterization

In order to investigate surface phonons and lattice dynamics of EuO(0 0 1) ultrathin films, single crystalline films with a thickness of 1 and 2 monolayers (ML) were epitaxially grown on Yttrium Aluminate substrate $YAlO_3(1\,1\,0)$ in the MBE chamber located at the beamline ID18 of the ESRF. One ML is equivalent to a film thickness of 1.71 Å. Additionally, a bulk-like 45ML thick EuO film was also grown on the same substrate and investigated for comparison. Vacuum out-gassed Eu metal enriched to 97% in the Mössbauer-active isotope ^{151}Eu supplied by the Oak Ridge National Laboratory (USA) was sublimated from an effusion cell with molybdenum crucible for producing a steady flux of Eu atoms. A molecular oxygen of high purity (99.999%) was supplied via a leak valve. The $YAlO_3(1\,1\,0)$ has a rectilinear surface, with lattice parameter of 7.431 Å along $[1\,\bar{1}\,0]$ and 7.371 Å along [0 0 1] [115]. This surface provides a small biaxial strain resulting from the lattice mismatch of 2.2% for EuO$[1\,1\,0]\|YAlO_3[1\,\bar{1}\,0]$ and 1.4% for EuO$[1\,\bar{1}\,0]\|YAlO_3[0\,0\,1]$. Similar to the growth on YSZ, the adsorption controlled growth regime was utilized for stabi-

lizing stoichiometric EuO [48, 115]. The oxygen mobility in YSZ is high compared to $YAlO_3$, making the synthesis of stiochiometric ultrathin EuO films on YSZ(0 0 1) difficult. Even without an external supply of oxygen, the metal deposited on the surface is oxidised for upto about 6 ML [48]. Several attempts to stabilise single crystalline ultrathin films of EuO using oxygen diffusing from the YSZ failed due to the formation of higher oxides of europium. On the other hand, $YAlO_3$ proved to be an ideal substrate for the growth of ultrathin EuO films. The low oxygen diffusion from the substrate enables a precise control over the amount of oxygen at the surface by adjusting the partial oxygen pressure in the growth chamber via a leak valve.

The next challenge in the epitaxial growth of these ultrathin films was to reduce the surface roughness. It was found that the oxygen partial pressure and sample temperature play a crucial role in controlling the surface morphology of the samples. Table 5.1 correlates the sample growth parameters to the respective RHEED images shown in figure 5.1. The RHEED images in the left and right columns of figure 5.1 correspond to [1 1 0] and [1 0 0] directions of the substrate and the film. The substrate was annealed in oxygen atmosphere for 120 min prior the sample growth to achieve a clean and flat surface, see figure 5.1(a) and (b). The RHEED images of the samples used for the nuclear inelastic scattering experiments that were grown at an optimal oxygen partial pressure P_{ox} of 2×10^{-9} mbar and a sample temperature of 450 °C are shown in figure 5.1(c-h). The streaks and the vertical elongation of the spots in the RHEED images of 45ML and 2ML thick films imply a smooth film-like morphology. The weak reflections from the 1ML thick film are due to the very low scattering volume, however the absence of reflections from the substrate proves the homogeneous spread of the film. The influence of elevated temperatures up to 550 °C and reduced oxygen pressure of 1×10^{-9} mbar on the surface morphology of approximately 3ML thick EuO film are illustrated in figure 5.1(i-l). These RHEED images show a relatively high background compared to the RHEED images in figure 5.1(c-h). In addition, they reveal reflections similar to that of the substrate implying a rough and partial coverage of EuO over the substrate. The higher EuO growth temperatures force rapid re-evaporation of Eu atoms from the surface lead-

RHEED image	Film thickness (ML)	p_{ox} (mbar)	T (°C)	Eu rate (Å/min)
c,d	45	2×10^{-9}	450	8
e,f	2	2×10^{-9}	450	8
g,h	1	2×10^{-9}	450	8
i,j	3	1×10^{-9}	525	8
k,l	3	1×10^{-9}	560	8

Table 5.1: Correlation between the oxygen partial pressure, substrate temperature, Eu deposition rate and the RHEED images shown in figure 5.1.

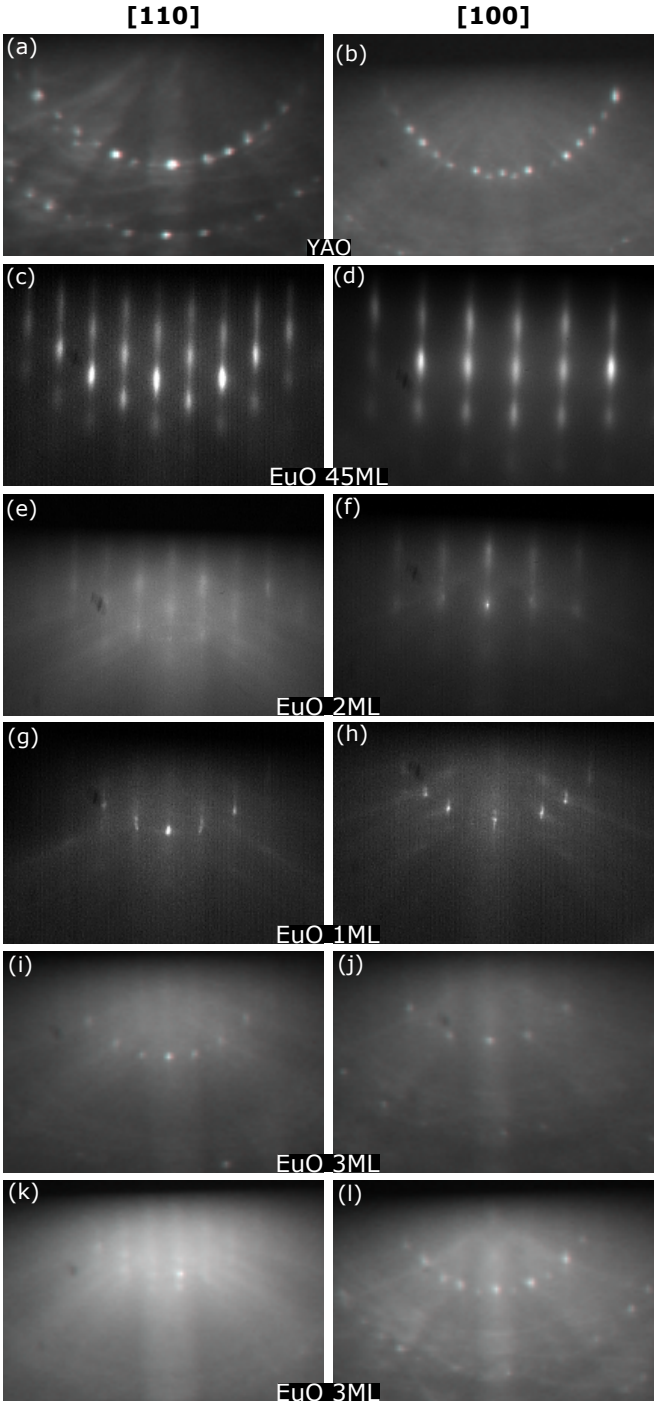

Figure 5.1: (a,b) RHEED (using electron energy 30 keV) images of clean and annealed $YAlO_3$ substrate along [1 1 0] and [1 0 0]. (c,e,g) RHEED images along EuO[1 1 0] direction of 45ML, 2ML and 1ML thick films. (d,f,h) RHEED images along EuO[1 0 0] direction of 45ML, 2ML and 1ML thick films. (i,k) and (j,l) RHEED images along EuO[1 1 0] and EuO[1 0 0] direction of 3ML films that were grown at slightly different temperature and p_{ox} compared to the optimal parameters, see table 5.1 for details.

Direction	a_{45ML}	a_{2ML}	a_{1ML}	$a_{reported}$
[1 1 0]	3.7 ± 0.1	3.7 ± 0.1	3.8 ± 0.1	3.68
[1 0 0]	2.6 ± 0.1	2.6 ± 0.1	2.6 ± 0.1	2.55

Table 5.2: Lattice spacing (in Å) of 1, 2 and 45ML thick EuO films calculated from the RHEED data along the indicated directions. The published lattice spacing are also given for comparison [117].

ing to the formation of islands. The lattice spacings determined from the RHEED images are shown in table 5.2. The values remain constant for all the thickness

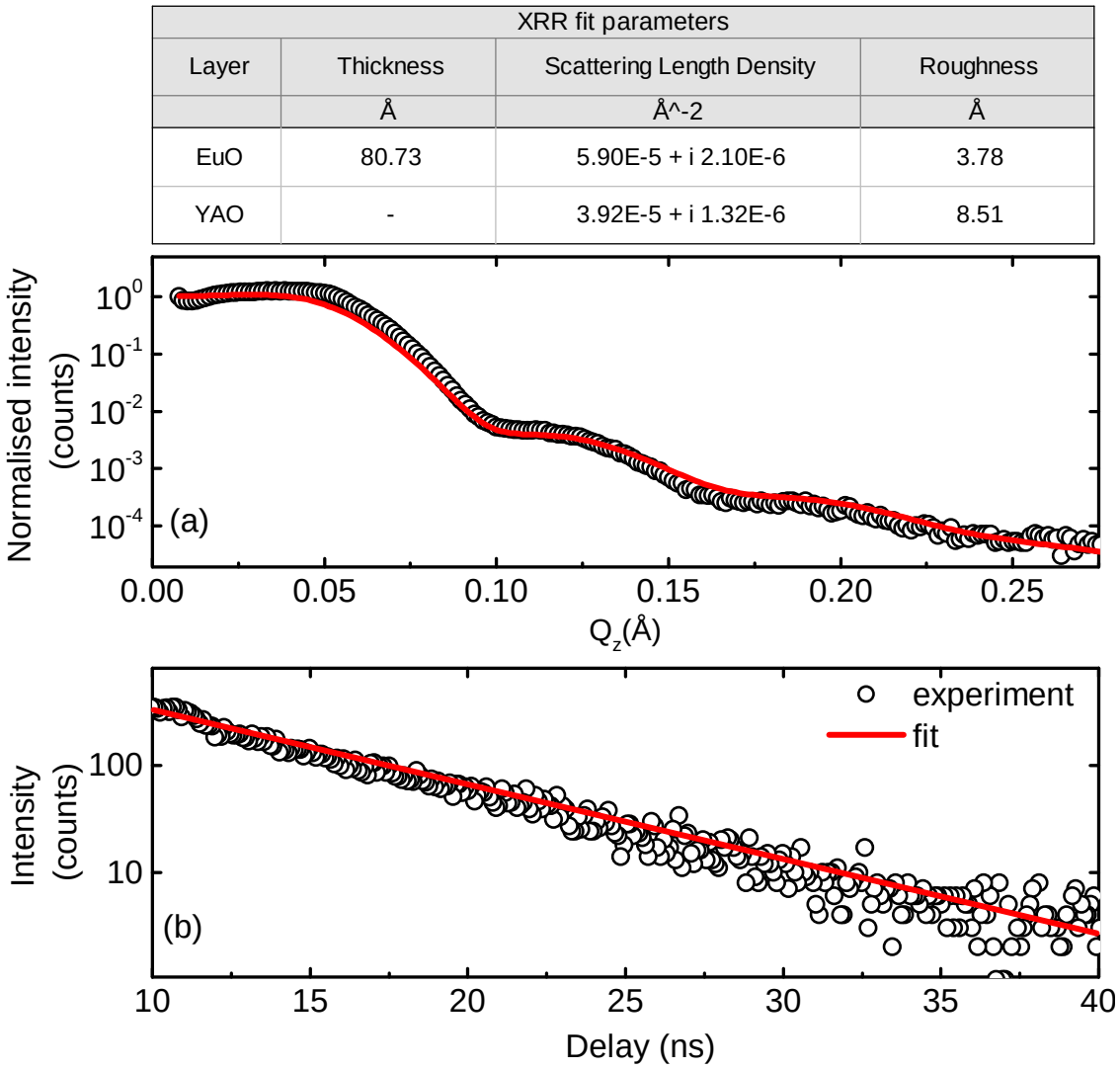

Figure 5.2: (a) XRR of the 45ML sample (circles) using photon energy of 21.54 keV and the fit (red/solid line). The results from fitting the XRR curve are shown in the table. (b) The experimental NFS spectrum (black/circles) of 45ML sample collected at room temperature and the fit (red/solid line).

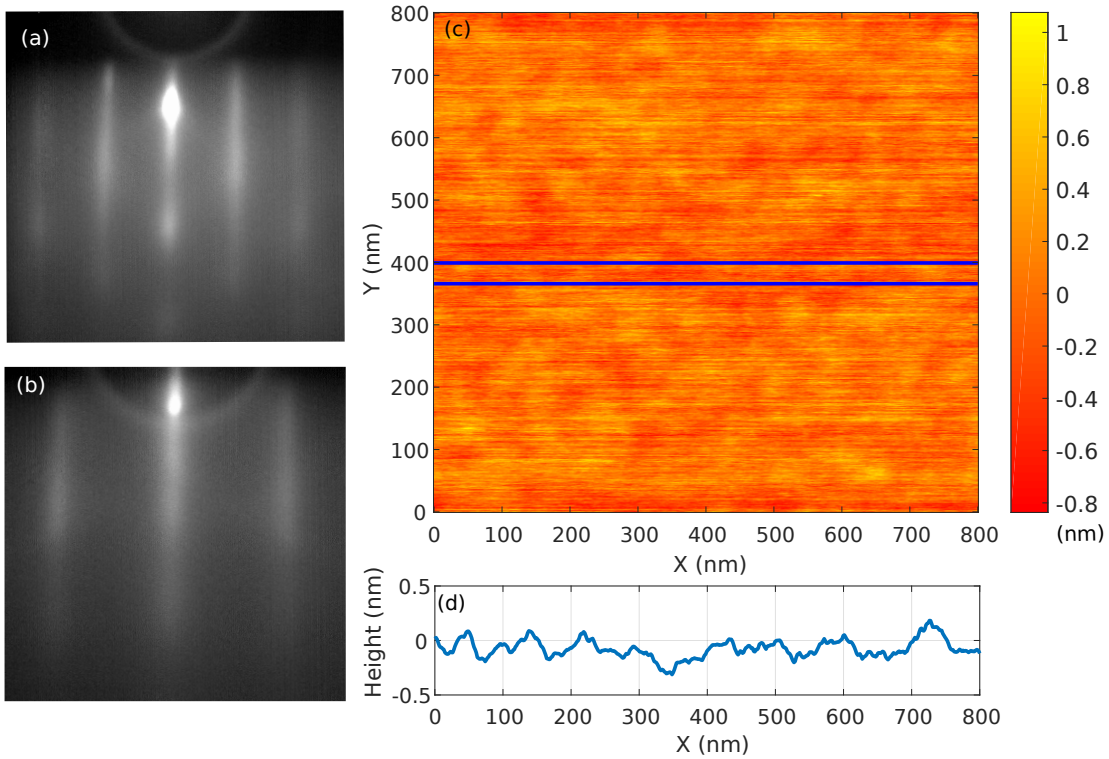

Figure 5.3: (a,b) RHEED images of the 3ML thick EuO sample along [1 1 0] and [1 0 0] azimuths, respectively. (c) AFM image of the 3ML thick EuO sample. (d) The height profile of the surface averaged in the area enclosed by the blue lines in the AFM image.

within the error limits and are similar to the published values [117]. A 50 °C higher growth temperature compared to the temperature used for the growth of EuO on YSZ substrate ensures the re-evaporation of the excess Eu atoms from the surface. Consequently, the film thickness does not correspond precisely to the amount of Eu deposited. In order to precisely caliberate the effective growth rate, the thickness of the bulk (45ML) sample was determined by x-ray reflectivity (XRR) measurement. The Kiessig fringes of the XRR curve were simulated using the Parratt formalism [146] and the experimental data was fitted using Parratt32 code [147], figure 5.2(a). The results of the fit are shown in figure 5.2. The scattering length density (SLD) of the substrate and film were kept constant during the fit. Assuming a linear relationship between rate of film formation and deposition time, the corresponding deposition time was calculated for the 1ML and 2ML thick films. Prior to the nuclear inelastic scattering experiment, the nuclear forward scattering signal of the 45ML sample was measured, figure 5.2(b). The featureless exponential decay of the time spectra reveals that all Eu atoms in the film are in an equivalent chemical state, confirming the chemical purity and stoichiometry of the EuO film.

In order to investigate the surface morphology, a 3ML thick film of EuO on

$YAlO_3$ was grown in the MBE chamber located in our home lab in ANKA, KIT and was investigated by *in situ* AFM. Vacuum out-gassed Eu metal supplied by the Ames Laboratory (USA) was sublimated from an effusion cell with pyrolytic boron nitride crucible for producing a steady flux of Eu atoms. The molecular oxygen of high purity (99.999%) was supplied via a leak valve attached to the chamber. The growth parameters of the sample were the same to the ones applied for growing the samples used for the NIS experiment at the ESRF. The RHEED images of a 3ML EuO film along EuO[1 1 0] and EuO[1 0 0] are shown in figure 5.3(a) and (b), respectively. The obtained interlayer distances and the features of the RHEED images are similar to the RHEED images of samples shown in figure 5.1(c-f). An AFM image of the 3ML thick EuO film is shown in figure 5.3(c). The flatness of the film surface is evidenced by the figure 5.3(d), which shows the height profile of the surface averaged between the blue lines that is indicated in figure 5.3(c).

5.2 Lattice dynamics

5.2.1 *Ab initio* approach

The first principles calculations reported here were performed by our collaborating partner Dr. habil. P. Piekarz from the Institute of Nuclear Physics in Krakow, Poland[1]. In order to investigate surface phonons, a computational model consisting of 5ML of EuO was assumed. The obtained phonon DOS and phonon dispersion curves of this 5ML thick slab are shown figure 5.4(a) and (b). The exclusive contribution of the surface layer to the phonon DOS of the slab is depicted in figure 5.5. The calculated phonon DOS of bulk EuO crystal is also shown for comparison.

[1]The computational model for calculating the phonon spectrum of ultrathin films of EuO was a five atomic layer thick slab. This structure was fully optimized using the projector-augmented wave method [45] and the generalized-gradient approximation [39] within the VASP program [44]. The strong electron interactions in the $4f$ states were treated with the GGA+U approach (U=8 meV). The ferromagnetic spin order of Eu atoms is assumed in all systems. The phonon spectra were calculated using the direct method implemented in the PHONON software [43]. The force constants and dynamical matrices were derived by displacing all non-equivalent atoms from equilibrium positions and calculating the Hellmann-Feynman forces. The phonon DOS was obtained by random sampling the k points in the first Brillouin zone.

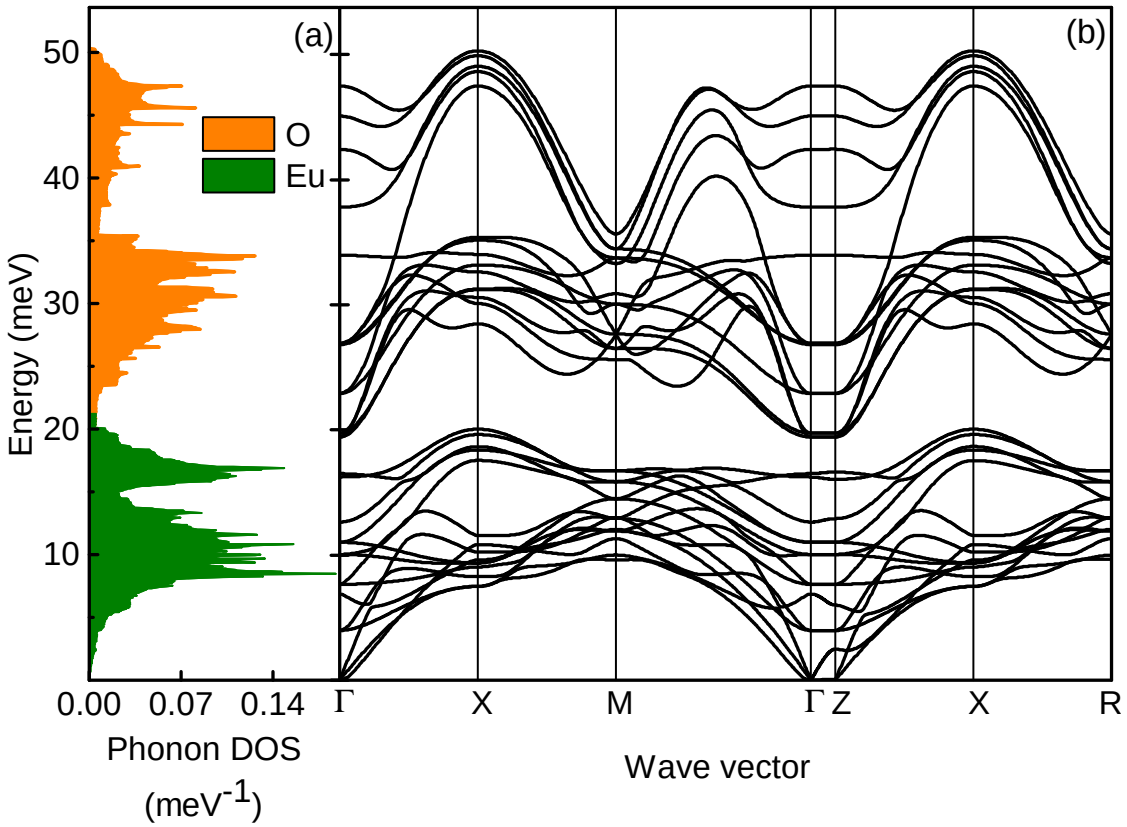

Figure 5.4: *Ab initio* calculated (a) phonon DOS and (b) dispersion curves of the 5ML thick EuO slab. The partial contributions of Eu and O atoms to the phonon DOS are indicated.

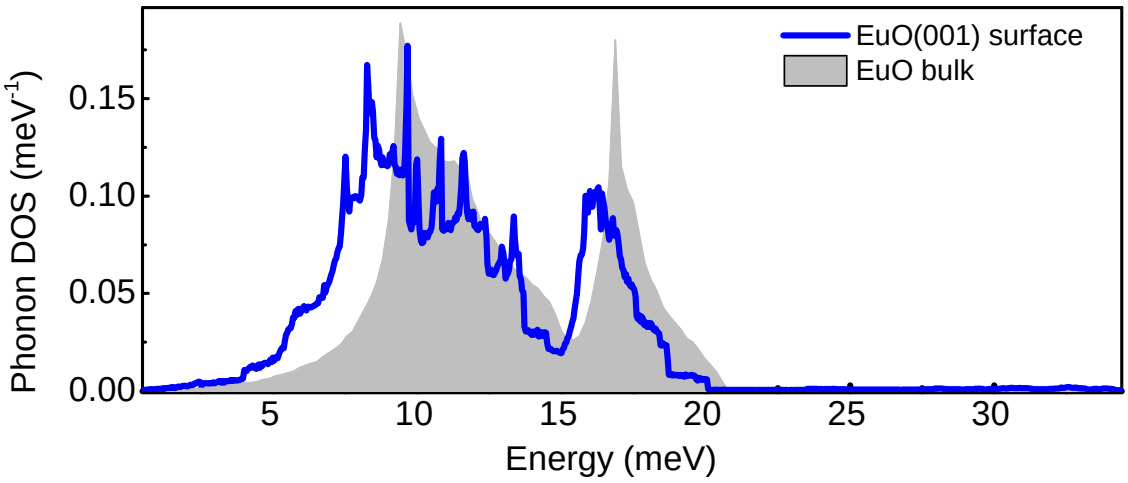

Figure 5.5: *Ab initio* calculated Eu-partial phonon DOS of EuO(001) surface that is obtained from the phonon DOS of the 5ML thick EuO slab. Eu-partial phonon DOS of the bulk EuO is shown for comparison (shaded area).

5.2.2 Nuclear inelastic scattering

The lattice dynamics of paramagnetic EuO ultrathin films of thickness 1ML, 2ML and 45ML were investigated by *in situ* nuclear inelastic scattering at the ID18 beamline of the ESRF. The samples were grown before the NIS experiment to exclude any contamination of the oxide surface by residual gases in the UHV chamber. All samples were measured at room temperature and additionally the 1ML and 45ML samples were measured at 130 K to reduce the multiphonon excitations. The extremely small scattering volume of the 1ML thick film required about 24 hours of measurement time to obtain NIS spectrum of reasonable statistics. Figure 5.6(a-c) shows the experimental spectra obtained as a sum over many short NIS scans and each of these scan was approximately 40 mins long. Figure 5.6(d-f) show the NIS

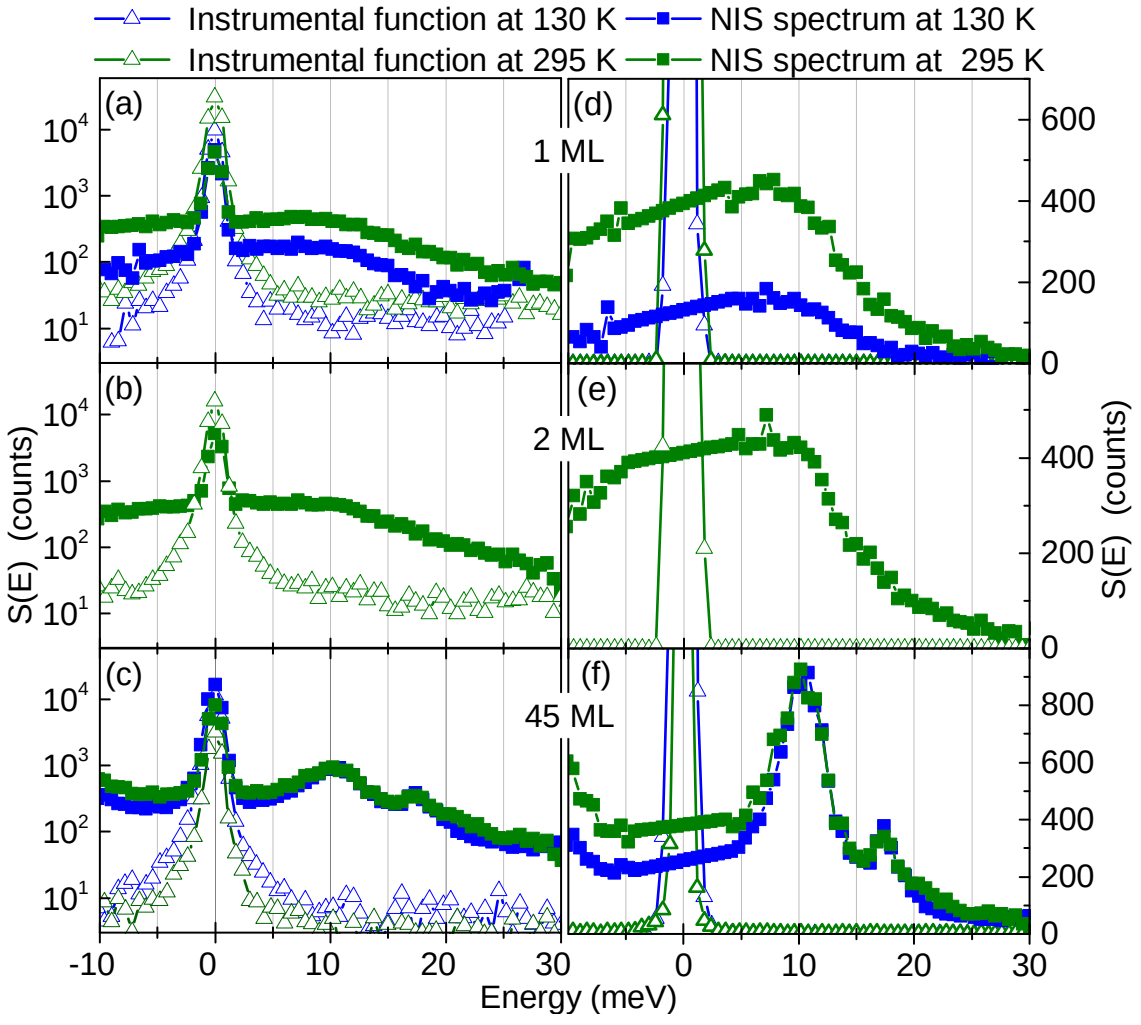

Figure 5.6: The experimentally obtained cumulative NIS spectra along EuO(1 0 0) (squares) and the simultaneously measured instrumental functions (open triangles) of the indicated samples at 295 (green) and 130 K (blue). (d)-(f) shows the NIS spectra after the first step of data processing to obtain phonon DOS, the elastic peaks were subtracted and the central part was approximated with a line segment.

spectra that have been corrected for the elastic line. All spectra are characterized by a central elastic peak (that is not directly proportional to the probability for recoilless absorption/emission of photons, or the Lamb-Mössbauer factor f_{LM} due to saturation effects of the detectors) and side bands corresponding to the phonon assisted nuclear resonant absorption/emission processes. In order to optimize the limited measurement time, only the central elastic peak and the signal to the positive energies, corresponding to the phonon creation processes were measured. The phonon signal towards negative energies was calculated at the temperature at which the experiment was performed by applying the detailed balance. The NIS spectra of the 1ML and 2ML samples (figure 5.6(a,b)) show drastic deviations from that of the 45ML sample. This already hints the changes in the lattice dynamics of ultrathin films compared to the bulk EuO crystal.

Figure 5.7 shows the Eu-partial phonon DOS of 1ML, 2ML and 45ML thick EuO thin films calculated from the corresponding NIS data (figure 5.6) following the procedure described in section 2.2.5. Phonon DOS of 1ML and 45ML samples shown in the figure were calculated from the NIS spectra obtained at 130 K, while the DOS of 2ML sample was obtained from the room temperature NIS spectrum. The shaded area corresponds to the *ab initio* calculated phonon DOS of bulk EuO convoluted with Gaussian function (FWHM=1.5 meV) to account for the instrumental broadening. Overall there is a very good agreement between the theoretical and experimental DOS of the 45ML sample. The absence of any systematic shift in the spectral features to lower energies shows the weak influence of epitaxial stain that is known to increase the lattice spacing by $\approx 2.5\%$ along EuO[1 0 0] [115].

Compared to 45ML sample, the phonon DOS of ultrathin samples (1ML and 2ML) show drastic changes. The spectral features are considerably shifted to lower energies due to changes in the force constants between the surface atoms as a result of reduced coordination at the surface [148, 149, 131]. In the case of 1ML phonon DOS, the peak at 17 meV that corresponds to longitudinal acoustic branch of bulk-like EuO is completely absent, while the 2ML thick film exhibits a few phonon states at this energy. This indicates that the phonon spectrum of 2ML sample can be considered as a combination of the surface and bulk phonon. The inset in figure 5.7 shows the relative change in phonon DOS of 1ML sample with respect to the bulk phonon DOS. The approximately 150% increase in the density of states at lower energies and lower cut-off energy compared to the bulk crystal are characteristic vibrational features arising from the broken translational symmetry at the surface [131].

The discovery of a giant anisotropic spin-phonon coupling in bulk EuO at temperatures less than 90 K is presented in the previous chapter. It was found that the coupling is stronger to the phonon modes that lie in the same energy range of the spin waves [**?**]. The enhancement of phonon DOS in the low-energy region, similar

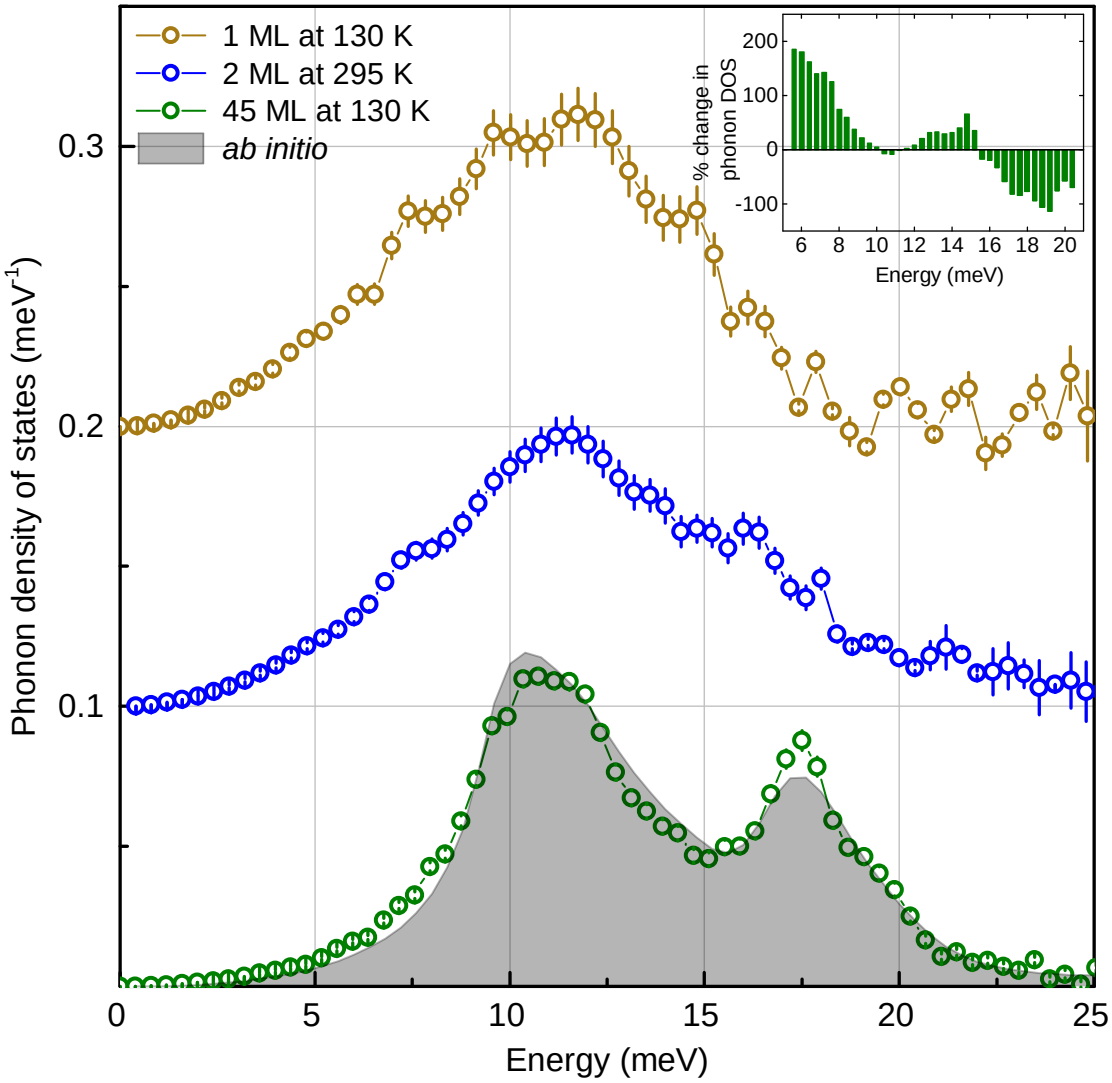

Figure 5.7: The experimentally obtained phonon DOS of 45ML, 2ML and 1ML samples at indicated temperatures. The shaded area corresponds to the *ab initio* calculated bulk phonon DOS convoluted with a Gaussian function of FWHM = 1.5 meV. The inset shows the relative change (in percentage) of phonon DOS of 1ML sample compared to the 45ML sample as a function of phonon energy.

to the energy range spanned by the spin waves in EuO could lead to an even stronger spin-phonon coupling in EuO ultrathin films near and below the Curie temperature. However, due to technical limitations this could not be verified within the frame work of this thesis.

The f_{LM} calculated from the experimentally determined phonon DOS and the corresponding relative contribution of various orders of n phonon excitations ($n > 1$) in the NIS spectra with respect to the single-phonon excitation are computed using equation 5.1 for all samples at the measured temperatures. The results are summarized in table 5.3.

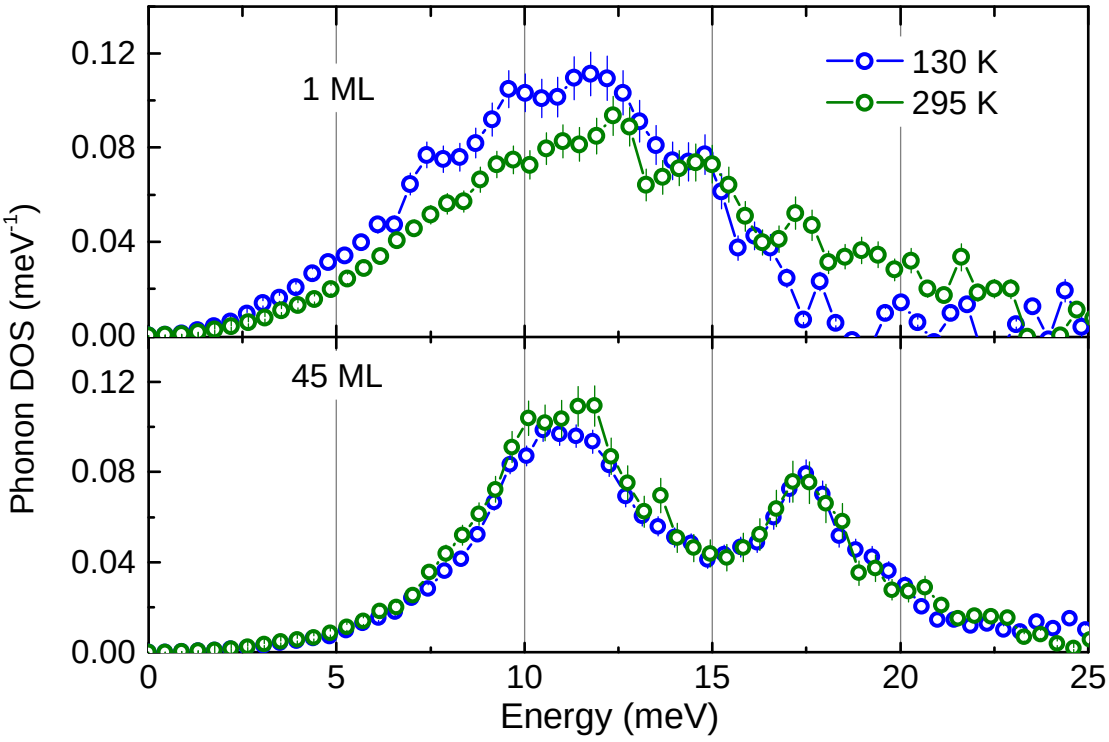

Figure 5.8: A comparison between the phonon DOS of 1ML and 45ML samples determined from the NIS spectra measured at room temperature (green circles) and at 130 K (blue circles).

$$\int S_n^m(E)dE = \frac{(-lnf_{LM}^m)^n}{n!}. \tag{5.1}$$

The table 5.3 shows that the Lamb-Mössbauer factor monotonously decreases with decreasing film thickness and increasing temperature. On the other hand, the contribution from higher order phonon excitations increases as the f_{LM} decreases. This makes the extraction of phonon DOS from the 1ML NIS spectrum measured at room temperature difficult, given the relatively high multiphonon contribution compared to the bulk-like 45ML sample. Figure 5.8 shows the phonon DOS of 1ML and 45ML sample extracted at 130 K and at room temperature. The rather high

Thickness	T=295 K			T=130 K		
	f_{LM}	$\frac{S_2}{S_1}$	$\frac{S_3}{S_1}$	f_{LM}	$\frac{S_2}{S_1}$	$\frac{S_3}{S_1}$
1ML	0.26	0.719	0.323	0.51	0.337	0.074
2ML	0.27	0.611	0.286			
45ML	0.54	0.179	0.055	0.68	0.194	0.025

Table 5.3: Calculated Lamb-Mössbauer factors for EuO films of different thickness at 295 and 130 K. The ratio of n^{th} order phonon excitation to the first order phonon excitation in the NIS spectrum is also indicated.

value of f_{LM} of the 45ML thick film results in minor influence of the multiphonons on the phonon DOS obtained at room temperature. The situation is quite different in the case of 1ML thick sample. The rather low f_{LM} leads to a substantial multiphonon contribution and this leads to discrepancies between the phonon DOS obtained at room temperature and at 130 K.

Lattice dynamics of two monolayer thick film

The phonon DOS of 2ML sample shown in figure 5.7 is obtained from the experimental NIS spectrum under the assumption that the Lamb-Mössbauer factors of the surface and the sub-surface layer are equal. However, in reality, the vibrations of the top layer of 2ML sample is expected to be similar to those in the 1ML sample and the second layer that is sandwiched between the surface and substrate is expected to be similar to the bulk (45ML). Therefore, lattice dynamics of 2ML thick film was modelled as a linear combination of bulk-like and surface phonon DOS using two different approaches. The first approach takes into account that the top and bottom layers have different Lamb-Mössbauer factors. In the second approach, the phonon DOS of 2ML sample is directly obtained from the NIS spectrum assuming an averaged Lamb-Mössbauer factor, is modelled using the phonon DOS of 1ML and 45ML samples.

Approach 1: The impact of a low f_{LM} value on the determination of the phonon DOS from NIS spectrum is demonstrated in figure 5.8. In such a scenario, the multiphonon contribution to the NIS spectrum of the 2ML film measured at room temperature is different for the top and the bottom layers due to their different f_{LM} values, see table 5.3. To disentangle the contributions from the two layers, the NIS spectrum S(E) of the 2ML sample has to be fitted with a model function which is a linear combination of NIS spectra of bulk (45ML) and surface (1ML) components. The relative contribution of the bulk and the surface components are obtained from the fit. Using the same relative contributions, the phonon DOS of the 2ML sample is obtained as a linear combination of the phonon DOS of the 45ML and 1ML samples. Prior to the fitting procedure, the Lipkin's sum rule (equation 2.58) is applied to normalise the NIS spectra. According to Lipkin's sum rule, the integral of the product of energy and NIS spectrum ($E.S(E)$) is equal to the recoil energy of the resonant nuclear transition. This recoil energy is identical for 1,2 and the 45ML samples. Therefore, instead of the NIS spectra, $E.S(E)$ curves are used for fitting. The model function is given by:

$$E.S^{2ML}(E) = a_{surface} \times E.S^{1ML}(E) + (1 - a_{surface}) \times E.S^{45ML}(E) * DHO(Q_{bulk}) \tag{5.2}$$

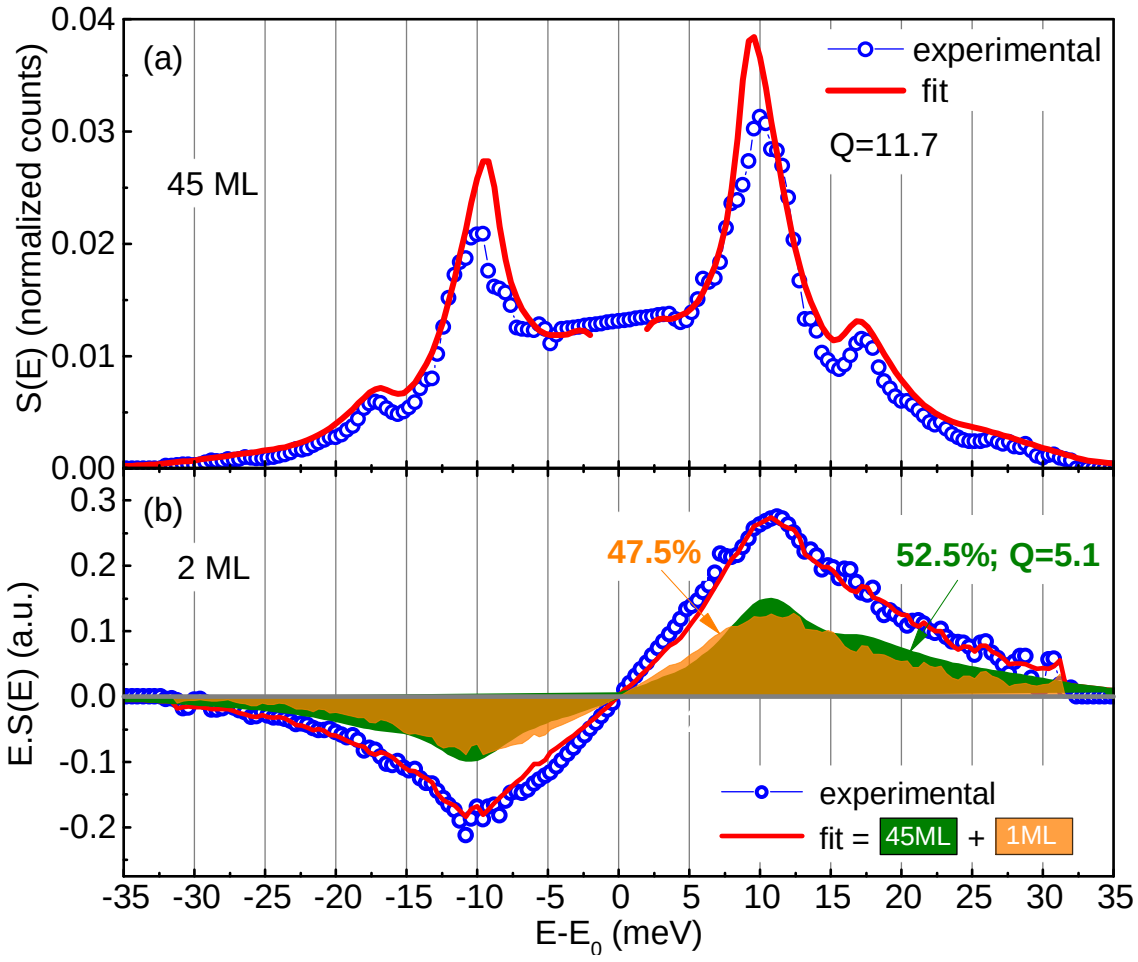

Figure 5.9: (a) Experimentally obtained NIS spectrum of 45ML EuO film (blue/circles) at room temperature and NIS spectrum simulated from the *ab initio* calculated DOS convoluted with damped harmonic oscillator function (red/solid line). (b) The $E.S(E)$ curve of the 2ML sample (blue/circles) and the fit (red/solid line) using the model function (equation 5.2) consisting of the E.NIS spectra of 1ML (green area) and 45ML sample (orange area). The obtained values of the fit parameters are also shown.

where,

$$E.S^{45ML}(E) * DHO(E, E', Q_{bulk}) = \int_0^\infty DHO(E, E', Q_{bulk}) E.S^{45ML}(E) dE \quad (5.3)$$

$$DHO(E, E', Q_{bulk}) = \frac{1}{\pi Q_{bulk} E'} \frac{1}{(E'/E - E/E')^2 + 1/Q_{bulk}^2}, \quad (5.4)$$

where $a_{surface}$ is the relative contribution of the surface phonons and the remaining $(1 - a_{surface})$ is the relative contribution of the bulk phonons. At each energy E', the $E.S(E)$ curve of 45ML sample is assumed to have an energy distribution given by the $DHO(E, E', Q_{bulk})$. The damped harmonic oscillator function was chosen to describe the phonon damping effect similar to the phonon investigations

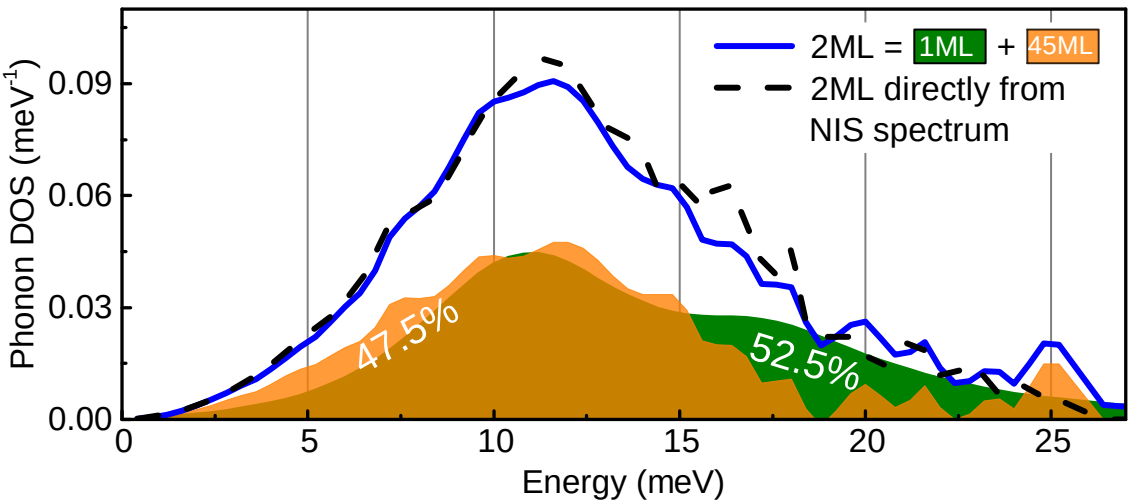

Figure 5.10: Phonon DOS of 2ML sample (blue/solid line) calculated as a linear combination of the DOS of 1ML (green area) and 45ML (orange area) samples using parameters obtained from the fit of equation 5.2 to the NIS spectrum (figure 5.9(b)). The phonon DOS of 2ML sample (black/dashed line) calculated directly from the NIS spectrum is shown for comparison. The obtained values of the fit parameters are also shown.

performed on Fe nanocrystals [150] and thin films [151]. Moreover, the DHO model reliably describes the elastic part of the dynamic structure factor of a system with anharmonic interactions [152]. The model function given by equation 5.2 contains two adjustable parameters namely the relative surface fraction $a_{surface}$ and quality factor Q_{bulk}. The function was numerically fitted to the $E.S(E)$ curve of the 2ML sample using a χ^2 minimization routine. The fits were performed in MATLAB®. Since the NIS spectrum of the 2ML system was only measured at room temperature, the NIS spectra of the components obtained at the same temperature were used for the fit. Prior to the fitting process, the NIS spectra were preconditioned in the following manner: First, the signal towards the negative energies of the NIS spectra that correspond to phonon annihilation processes were calculated according to the detailed balance and the multiphonon contribution at room temperature. Second, the central peaks of the NIS spectra that correspond to the elastic processes without involvement of phonon excitations were removed by using the instrumental functions measured simultenously with the NIS spectra. The part between ± 4 meV was approximated as a line segement. Finally, the corresponding $E.S(E)$ curve was computed and it normalized to the recoil energy ($E_R = 1.648$ meV) following the Lipkin sum rules [64].

Figure 5.9(a) shows the experimentally obtained NIS spectrum of the 45ML sample that is fitted with the NIS spectrum simulated from the *ab initio* calculated phonon DOS convoluted with a Gaussian function (FWHM=1.5 meV) and with a

DHO function with Q factor as a fit parameter. The quality factor obtained from the fit is 11.7, and serves as a reference to quantify the damping seen in the ultrathin films. The resulting fit of the NIS spectrum of 2ML sample is shown in figure 5.9(b). The fit reveals that the phonons in 2ML thin film of EuO could be modelled as a sum of 47.5% surface (1ML) and 52.5% bulk-like (45ML) phonons. The Q factor of the bulk phonons is 5.1 which is smaller than the Q value obtained for the 45ML sample, indicating the heavy damping of the bulk-like phonon modes in the second layer that lie at the film/substrate interface. The corresponding DOS of 2ML sample is calculated using the partial contributions and Q factor obtained from the fit to the NIS spectrum, see figure 5.10. Additionally, the phonon DOS computed directly from the NIS spectrum (assuming an averaged Lamb-Mössbauer factor for the surface and the bulk) is shown (black/dashed line) for comparison. In spite of the non-negligible difference in the Lamb-Mössbauer factors of the surface and the bulk components, the 2ML phonon DOS computed directly from the NIS spectrum reproduces the 2ML phonon DOS calculated by fitting the NIS spectrum to a large extend.

Approach 2: The alternative approach for modelling the lattice dynamics of the 2ML sample as a linear combination of surface and bulk phonons is by a direct fit of the phonon density of states extracted from the experimental NIS spectrum of this sample. Similar to the fitting procedure of the NIS spectrum, a model function $g(E)_{2ML}$ that is a linear combination of surface (1ML) phonon DOS and bulk (45ML) phonon DOS convoluted with a damped harmonic oscillator is fitted to the 2ML phonon DOS $g(E)$ that is obtained directly from the NIS spectrum:

$$g(E)_{2ML} = a_{surface} \times g(E)_{1ML} + (1 - a_{surface}) \times g(E)_{45ML} * DHO(Q_{bulk}) \quad (5.5)$$

The 1ML phonon DOS that was obtained at 130 K was used for the fitting procedure to avoid any effects of the multiphonons that could be still present in the phonon DOS extracted at room temperature. The results of the fitting procedure are plotted in figure 5.11. The figure shows that the DOS of the 2ML system consists of 48.1% surface and 51.9% bulk-like phonons. The quality factor obtained from the fit is 8.5. The phonon DOS of 45ML sample was fitted with *ab initio* calculated phonon DOS that is convoluted with a damped harmonic oscillator function with quality factor as a fit parameter, see figure 5.11(a). The obtained value of Q is 11.7, indicating the same magnitude of damping of the bulk-like phonons in the 2ML sample as derived from analysis of the NIS spectrum.

The ratio between the surface and the bulk components in 2ML sample obtained by fitting the $E.S(E)$ and DOS curves are summarized in table 5.4. Both results imply that the vibrations in the 2ML thick film could be described as two

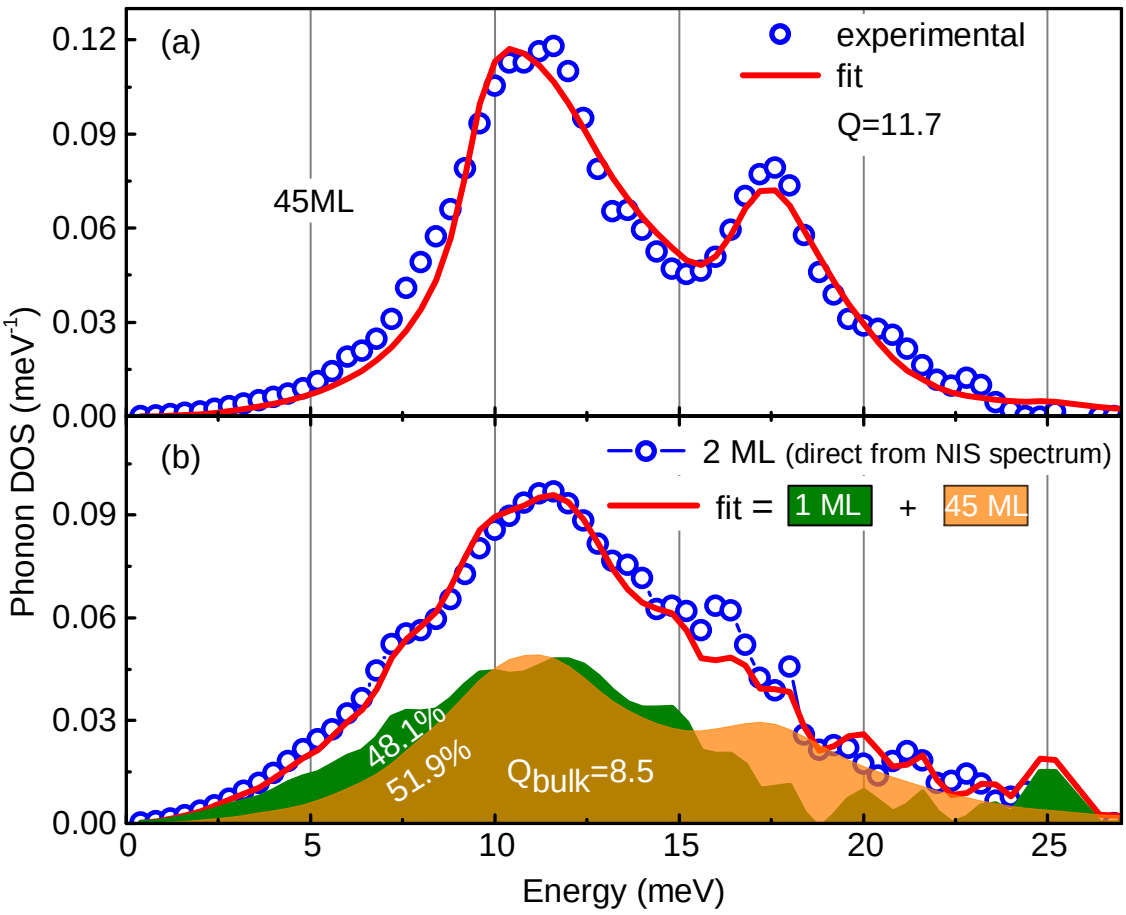

Figure 5.11: (a) Experimentally obtained phonon DOS of 45ML sample (blue/circles) and *ab initio* calculated DOS convoluted with a damped harmonic oscillator function (red/solid curve). (b) The phonon DOS of 2ML sample (blue/circles) determined from the experimental NIS spectrum assuming an averaged f_{LM} and the fit (red/solid line) using the model function (equation 5.5) that consists of phonon DOS of 1ML (green area) and 45ML samples (orange area). The obtained values of the fit parameters are also shown.

approximately equal contributions of the surface and bulk-like phonons. The bulk contribution seems to be heavily damped that is evidenced by the low Q factors compared to the bulk value of 11.7. The minor differences in the fit parameters arise from the difference between the 2ML phonon DOS curves that tends to in-

	$a_{surface}$	a_{bulk}	Q_{bulk}
NIS spectrum fit	47.5%	52.5%	5.1
DOS fit	48.1%	51.9%	8.5

Table 5.4: Summary of the fit parameters obtained by analysis of the NIS spectrum and phonon DOS of the 2ML sample.

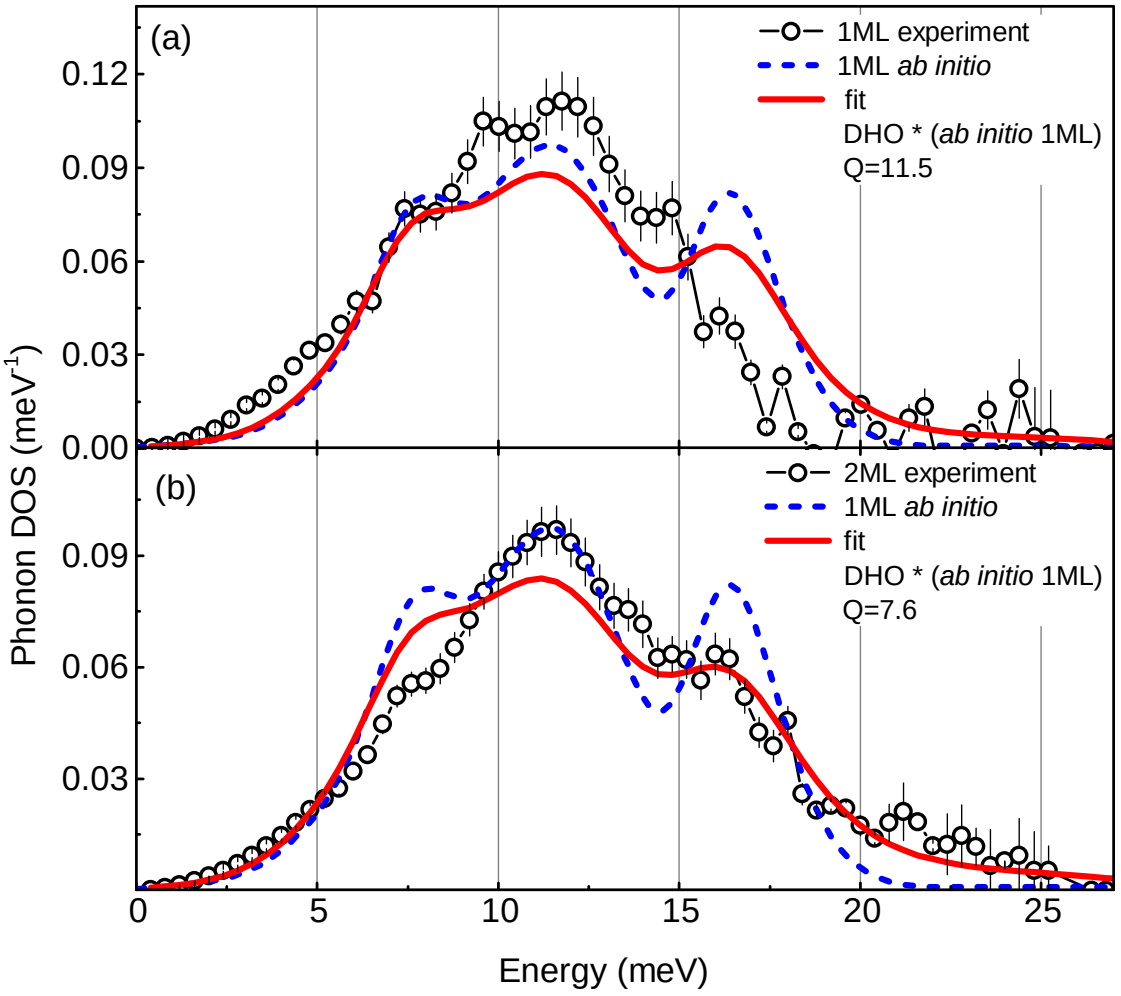

Figure 5.12: Comparison of *ab initio* calculated Eu-partial EuO(001) surface phonon DOS convoluted with a Gaussian function (blue/dashed line) with experimental (a) 1ML and (b) 2ML phonon DOS. The calculated 1ML phonon DOS was convoluted with damped harmonic oscillator function and was fitted to the experimental phonon DOS with Q being a fit parameter (red/solid line).

crease towards higher energies. Most likely the discrepancy towards higher energies originates from the incorrect multiphonon subtraction in the DOS that is directly obtained from the NIS spectrum at room temperature.

Deeper insights into the lattice dynamics of EuO ultrathin films are obtained with the aid of *ab initio* calculated surface phonon DOS. Figure 5.12 shows the comparison between calculated Eu-partial phonon DOS of the EuO(001) surface and the experimentally obtained phonon DOS of 1ML and 2ML samples. The calculated phonon DOS is convoluted with a Gaussian function of FWHM=1.5 meV to account for the instrumental broadening (blue/dashed lines). Additionally, the calculated phonon DOS was convoluted with damped harmonic oscillator function and was fitted to the experimental 1ML and 2ML phonon DOS with the quality factor Q

being a fit parameter (red/solid lines). Figure 5.12(a) shows an increasing disparity between the calculated and experimental phonon DOS of the 1ML sample towards higher energies. In the experimental spectrum the peak at 17 meV is suppressed and shows a lower cut-off energy than the calculated phonon DOS. On the other hand, the 2ML experimental phonon spectrum is in better agreement with the calculated surface phonon DOS, see figure 5.12(b). The convolution of the calculated spectrum with damped harmonic oscillator could reproduce the experimental data very well. The feature at 17 meV is damped but visible in the experimental 2ML phonon DOS unlike the 1ML spectrum. The Q factor obtained from the fit to the experimental 1ML and 2ML DOS are 11.5 and 7.6, respectively.

Ideally the atomic vibrations in the 1ML sample should be composed of surface phonons. However, the *ab initio* calculations were performed on a native EuO(0 0 1) surface, while in the experiment, the 1ML EuO is prepared on a substrate. It is known that EuO thin films grow coherently on $YAlO_3$ up to a film thickness of 8 nm [115]. The suppression of the high-energy feature at 17 meV is most likely the influence of the substrate on the 1ML EuO film. The striking similarity of the experimental 2ML phonon spectrum to the calculated phonon spectrum of the native EuO surface is most likely due to the sub-surface layer of the EuO film that screens the effect of the substrate on the surface layer. The damping in phonon DOS, which is evidenced by the Q factor of 7.6, arises from the cumulative effect of the substrate and from the imperfections in the film.

5.3 Thermodynamic and elastic properties

From the Eu-partial phonon density of states a variety of Eu-partial thermodynamic and elastic properties can be determined as discussed in section 2.2.5. Figure 5.13 shows selected thermoelastic properties, such as vibrational amplitude (A_{vib}), lattice specific heat (C_v), vibrational entropy (S_{vib}) and mean force constant (K), deduced from the phonon density of states as a function of film thickness at room temperature and at 130 K. The vibrational amplitude and entropy show an increase of approximately 28% and 10%, respectively, as the film thickness is reduced to 1ML. This behaviour is consistent with the 12% reduction in force constant in case of 1ML thick film, see figure 5.13(c). It imples that the surface is mechanically softer compared to the bulk crystal. Figure 5.13(d) plots the lattice specific heat that remains constant within the error limits for all thickness at a given temperature. As the temperature increases from 130 K to 295 K, it reaches the classical limit of $3k_B$/atom. The magnitude of the thermoelastic properties of the 2ML sample lie in between those of the bulk and the 1ML samples. The thermoelastic properties of the 2ML sample calculated from the phonon DOS obtained directly from the NIS spectrum as well as from the phonon DOS obtained from the fit to the E.NIS spec-

trum (represented with '★' marker) are shown seperately in figure 5.13. Except for the derived mean force constant, all other properties have a similar values within the error limits. The discrepancy in the force constants arises from the fact that K is calculated from the third moment of the phonon DOS that is weighted more to the high-energy part of the spectrum [36], where the phonon DOS obtained by the both approaches show some disagreement. The feature at 25 meV in 2ML phonon DOS obtained from the fit to the E.NIS spectrum is a contribution from the 1ML phonon DOS (surface component). Using the aid of *ab initio* calculations, the origin of this feature is confirmed to arise from the low statistics of the collected data and has no physical meaning. The calculation of K excluding this artificial feature around 25 meV gives a value of 39.93 Nm^{-1} (indicated with '☆' symbol) which is similar to the value of K determined from the DOS curve obtained directly from the NIS spectrum.

Additionally, the reduced phonon DOS ($\mathrm{g(E)/E^2}$) of the ultrathin films and bulk-like film are plotted in figure 5.14 to compare the Debye levels derived from the low energy region (E< 7 meV). The systematic increase in the Debye levels implies a reduction of the speed of sound as the thickness of the EuO film is reduced to a single monolayer. Since the acoustic branches are exclusively made up of vibrations of the Eu atoms, the Eu-partial phonon DOS could be safely used for calculating the average speed of sound v_s. v_s can be calculated from the Debye level obtained from the reduced phonon DOS according to the equation 5.6 [33] and, are shown in figure 5.14:

$$\lim_{E\to 0} \frac{g(E)}{E^2} = \frac{m_R}{2\pi^2\hbar^3\rho v_s}, \tag{5.6}$$

where m_R is the mass of the resonant nuclei and ρ is the mass density. The reduction of sound velocity in ultrathin films implies a reduced phonon group velocity. Consequently, this affects the macroscopic heat conduction in crystals, especially for insulators and semiconductors were the thermal conductivity is dominated by phonons. In a simple Debye solid, thermal conductivity λ is given as:

$$\lambda = \frac{1}{3} C\tau v_s^2, \tag{5.7}$$

where C is the specific heat capacity and τ is the average phonon relaxation time. The reduction of 35% in v_s in the 1ML thick film compared to the bulk-like film leads to 58% decrease in lattice thermal conductivity, assuming that the average phonon relaxation time remain constant.

5.4 Conclusions

Single crystalline and stoichiometric ultrathin EuO(0 0 1) films of thickness 1ML and 2MLs were grown on $\mathrm{YAlO_3}$(0 0 1). The lattice dynamics of these samples in para-

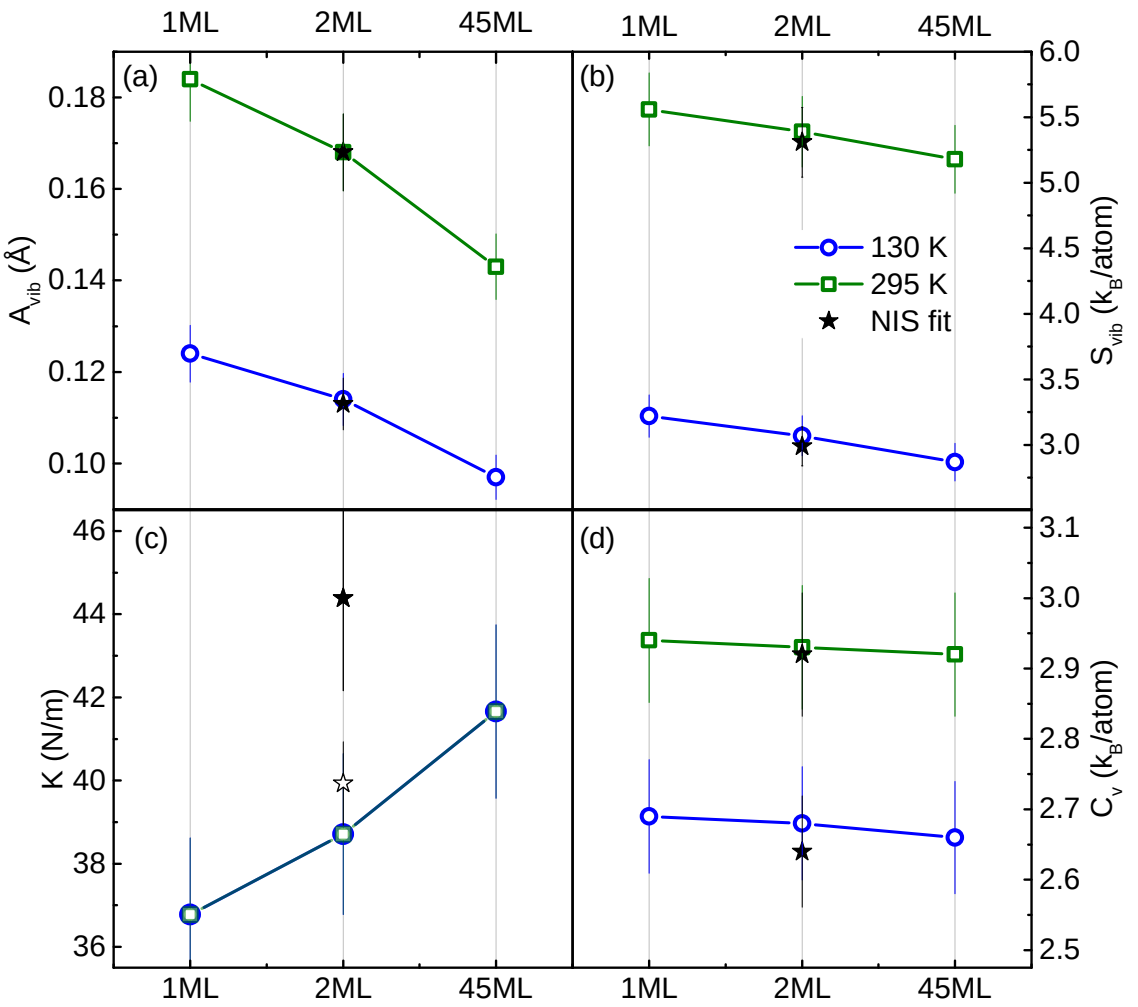

Figure 5.13: Selected thermoelastic properties - (a) vibrational amplitude, (b) vibrational entropy, (c) mean force constant and (d) lattice specific heat plotted as a function of film thickness at 295 (green squares) and 130 K (blue circles). The '★' symbol indicates the corresponding properties of the 2ML sample computed from the phonon DOS assuming different f_{LM} for the surface and the bulk. The similarly calculated force constant of the 2ML film that has been corrected for statistical errors is indicated by '☆' symbol (see text).

magnetic state was determined using nuclear inelastic scattering and is compared to the lattice dynamics of bulk-like film with a thickness of 45ML. The phonon DOS of the 1ML sample is dominated by the surface modes and exhibits a reduced cut-off energy and a higher number of states at low energies compared to the bulk phonon DOS. The lattice dynamics of the 2ML film was modelled as a combination of surface (1ML) and bulk-like (45ML) phonons by fitting the experimental $E.S(E)$ curve (NIS spectrum) and alternatively by fitting the directly extracted phonon DOS from the NIS spectrum. The surface contribution to the phonon DOS of the 2ML sample was found to be 47.5% and 48.1% as obtained from the fit to

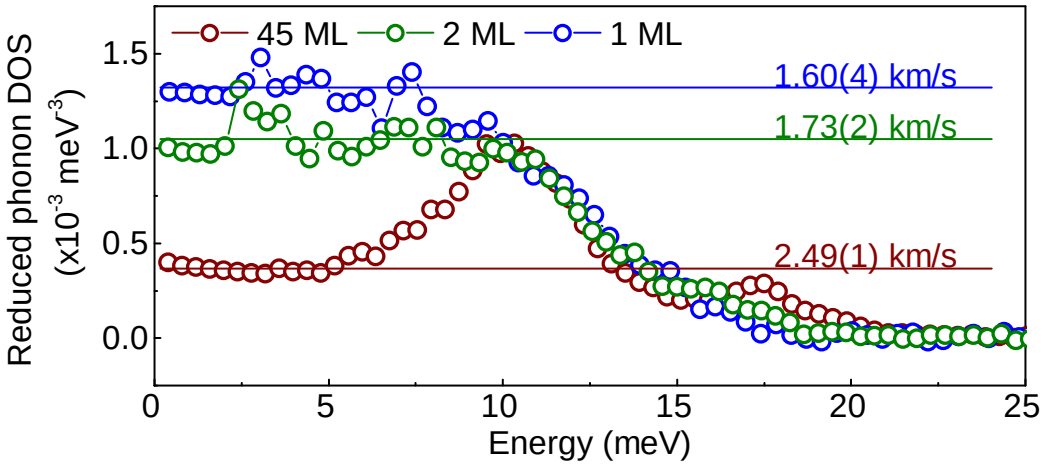

Figure 5.14: The experimentally obtained reduced phonon DOS of 1, 2 and 45 ML samples (circles) and the corresponding Debye levels (solid lines). The calculated speed of sound in the films are indicated.

the $E.S(E)$ curve and phonon DOS, respectively. The phonon DOS of the 45ML sample showed good agreement with the *ab initio* calculated phonon DOS convoluted with damped harmonic oscillator function with a Q factor of 11.7 to account for phonon lifetime broadening effects. This implies that in films with thickness of approximately 8 nm the lattice dynamics of EuO crystal is unaffected by size effects. The comparison of the experimental 1ML phonon DOS with the *ab initio* calculated surface phonon DOS showed differences towards higher energies, especially the predicted peak at 17 meV was not observed. Additionally, *ab initio* calculated phonon DOS was convoluted with DHO function to account for phonon damping effects and was fitted to the experimental phonon DOS with quality factor as a fit parameter. Surprisingly, the experimental 2ML phonon DOS was found to be in better agreement to the *ab initio* calculated surface phonon DOS, compared to the experimental 1ML phonon DOS. This behaviour is attributed to the damping of the atomic vibrations at the film/substrate interface by the infuence of the substrate. The thermoelastic properties of the ultrathin films showed deviation from the bulk values. The vibrational amplitude and vibrational entropy are increased by 28% and 10%, respectively, as the film thickness is reduced from 45ML to 1ML. This behaviour is consistent with the observed 12% reduction in the mean force constant of the 1ML sample compared to the 45ML sample. A systematic reduction in the lattice thermal conductivity with decreasing film thickess is observed, similar to the reported reduction in thermal conductivity upon nano-structuring in other material systems [30]. The weak influence of temperature on the mean force constant, similar to the bulk EuO, reveal the absence of pronounced anharmonicity in the ultrathin films. The most prominent effect on lattice dynamics of ultrathin films of EuO is the enhancement of the phonon DOS at lower energies (E<10 meV) similar to the

energies of the spin waves in EuO. The fact that bulk EuO exhibits a giant spin-phonon coupling makes it a perfect model system for studying this effect in thin films, surfaces and interfaces.

Chapter 6

Lattice dynamics of europium sesquioxide

This chapter describes the lattice dynamics of the cubic and monoclinic phases of Eu_2O_3 based on ab initio calculations. An attempt to experimentally verify the calculated phonon density of states of Eu_2O_3 using nuclear inelastic scattering on commercially available Eu_2O_3 powder is described. The relevant temperature dependent thermoelastic properties of cubic Eu_2O_3 are calculated and compared to those of EuO.

6.1 *Ab initio* approach

The first principles calculations reported here were performed by our collaborating partner Dr. habil. M. Sternik from the Polish Academy of Sciences, Kraków, Poland[1]. The obtained phonon DOS and dispersion curves of cubic Eu_2O_3 is shown in figure 6.1(a) and (b), respectively. The individual contributions to the phonon DOS by Eu and O atoms are indicated. The majority of the acoustic branches are made up of vibrations of Eu atoms and the optic branches with energies above 30 meV are entirely composed of vibrations of O atoms. There are also a few phonon modes of O atoms at lower energies (E $\leq$ 30 meV) that arise from coupling to the vibrations of the Eu atoms.

[1]Density functional theory was used to determine the lattice dynamics of cubic Eu_2O_3 (space group $Ia\bar{3}$). The electronic structure was optimized within the projector augmented-wave method [45] and the generalized-gradient approximation (GGA) [39] implemented in the VASP software [44]. The optimized lattice parameter a =10.89 Å corresponds well to the experimental value and the calculated electronic band gap of 4.5 eV agrees with the experimental value of 4.59 eV [122]. The phonon density of states and phonon dispersions were calculated using the direct method [43]. The Hellmann-Feynman forces were obtained by displacing non-equivalent atoms from their equilibrium positions to determine the force constants and dynamical matrices. Phonon energies and polarization vectors at a given wave vector follow from the exact diagonalization of the dynamical matrix.

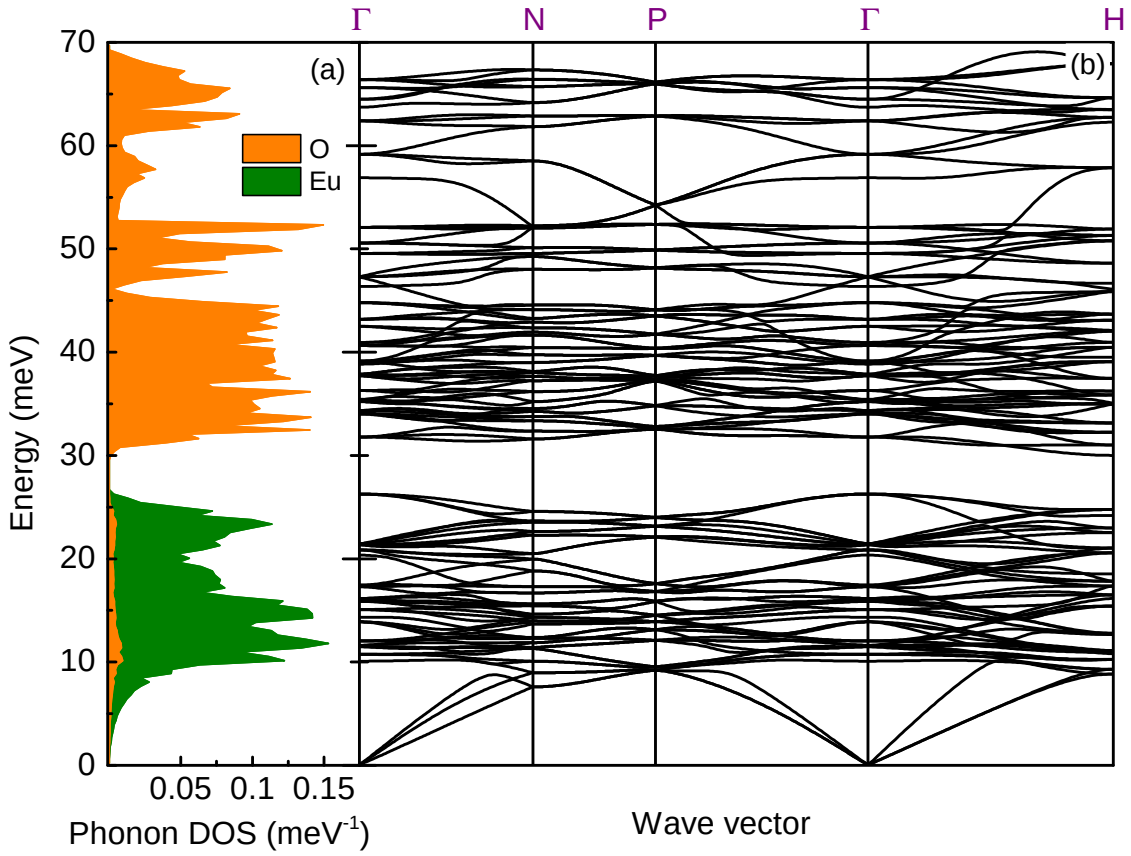

Figure 6.1: (a) *Ab initio* calculated phonon DOS of cubic Eu_2O_3, the partial contributions of Eu and O atoms are indicated. (b) *Ab initio* calculated phonon dispersion curves of cubic Eu_2O_3.

In addition to the cubic Eu_2O_3 phase, phonon dispersion curves and phonon DOS of the monoclinic phase of Eu_2O_3 (space group $C12/m$) were calculated and plotted in figure 6.2.However, the simulated system was unstable and resulted in soft phonon modes, i.e. phonons with imaginary energies. Figure 6.2(a) shows the soft modes plotted with negative energies extending up to -10 meV. Moreover, the non-Debye like behaviour of the low energy part (E 7 meV) of the phonon DOS implies that this phase is unstable in the conditions for which calculations are performed ($T = 0$, $p = 0$).

6.2 Nuclear inelastic scattering

The Eu-partial phonon DOS of commercially available Eu_2O_3 powder was measured using nuclear inelastic scattering at the Nuclear Resonance beamline ID18 of the ESRF. The Eu_2O_3 powder was made into an 8μm thick pellet and was sealed using kapton® foil. Although Eu_2O_3 is stable at ambient conditions prolonged exposure to moisture might result in contamination by $Eu(OH)_3$. The sealed pellet was char-

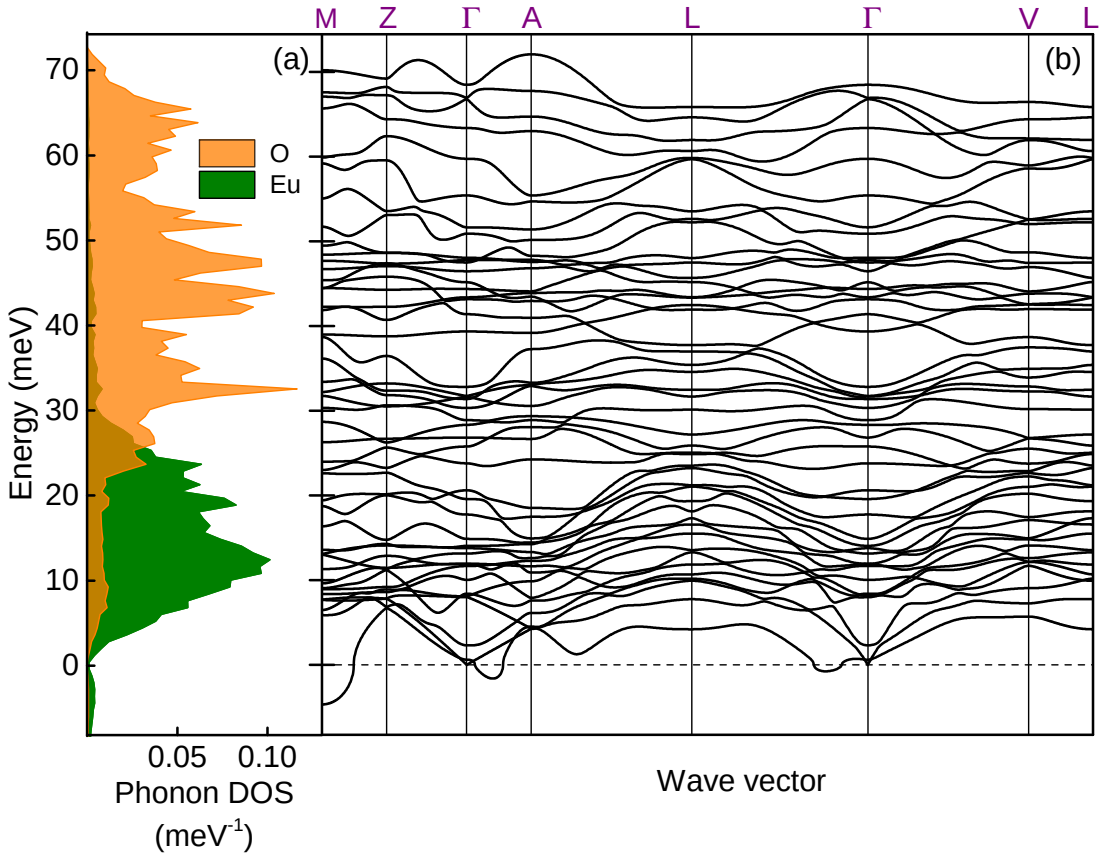

Figure 6.2: (a) *Ab initio* calculated phonon DOS of monoclinic Eu_2O_3, the partial contributions of Eu and O atoms are indicated. (b) *Ab initio* calculated phonon dispersion curves of monoclinic Eu_2O_3. The presence of soft modes plotted with negative energies are visible.

acterised by x-ray diffraction (XRD) and nuclear forward scattering (NFS). Figure 6.3(a) shows the XRD of the pellet obtained with a photon energy of 8.05 keV using Rigaku-SmartLab diffractometer. The irregular base of the sealed pellet caused x-ray scattering from the sample stage and also scattering from the kapton foil sealing induced additional background. Therefore, two XRD scans were performed to identify the signal from the pellet. The first one with maximum x-ray footprint on the sealed pellet and the second with the x-ray foot print completely on the sealing (shaded area). The x-ray diffraction peaks have been identified and are listed in the table 6.1 with their corresponding intensities.

The analysis revealed that the pellet consist of a mixture of cubic Eu_2O_3, monoclinic Eu_2O_3 and $Eu(OH)_3$. $Eu(OH)_3$ forms due to the hygroscopic nature of Eu_2O_3. Additionally, the pellet was characterised by nuclear forward scattering. Figure 6.3(b) shows nuclear forward scattering spectrum that indicates the chemical equivalence of all the Eu atoms. This equivalence is deduced from the *zero* isomer shift (IS) that is sensitive to the chemical coordination. However, the IS of $Eu(OH)_3$, cubic and monoclinic Eu_2O_3 have very similar values making them indistinguishable

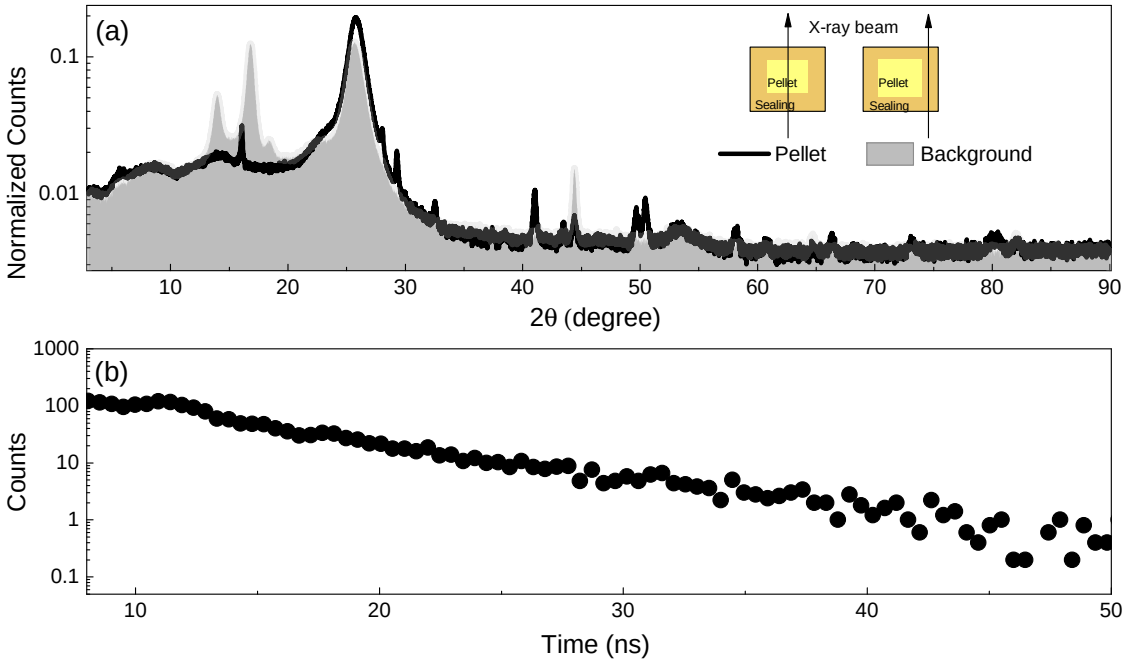

Figure 6.3: (a) The XRD scan of the Eu_2O_3 pellet (black/solid line) and a scan for the determination of background (shaded area). The position of the x-ray beam with respect to the sample is schematically presented. (b) NFS spectrum of the Eu_2O_3 pellet collected at room temperature.

in the NFS study. Nevertheless, the featureless decay excludes the presence of other oxides such as EuO, Eu_3O_4 and pure Eu metal.

The Eu-partial phonon DOS of the pellet was determined from the NIS spectrum that was measured at room temperature. The sample was measured in transmission geometry. The incident energy of the photons was tuned in the vicinity of the resonant transition energy (21.54 keV) of the ^{151}Eu nuclei with an energy resolution of 1.1 meV [123]. Figure 6.4(a) shows the cumulative NIS spectrum and the instrumental function. The fit to the instrumental function with a Voigt profile and the fit parameters are also shown in figure 6.4(a). The Gaussian width of the Voigt profile obtained from the fit is $\approx$1.1 meV. The phonon DOS obtained from the NIS spectrum and the *ab initio* calculated phonon DOS of the cubic Eu_2O_3 convoluted with a Gaussian curve of FWHM = 1.1 meV are shown in figure 6.4(b). Even though the differences between calculated and experimentally obtained phonon DOS are evident, the DOS curve of the pellet shows the main peaks at 13 meV and 22 meV, similar to the calculated phonon DOS. The phonon DOS of the pellet consist of the contributions from the monoclinic phase of Eu_2O_3 as well as from $Eu(OH)_3$, as evidenced from the XRD data. Since the phonon DOS of $Eu(OH)_3$ is not reported and our phonon calculations of the monoclinic phase of Eu_2O_3 were unstable, the calculated lattice dynamics is not fully validated by the experimental data. A more detailed experimental study on epitaxial Eu_2O_3 film with controlled phase and sto-

Peak position (deg)	Area	Structural phase	Reflection index
16.065	2.77×10^{-3}	Cubic	(2 0 0)
28.044	2.30×10^{-3}	$Eu(OH)_3$	(1 1 0)
29.294	2.11×10^{-3}	Monoclinic	(4 0 1)
32.497	8.39×10^{-4}	Monoclinic	$(\bar{1}\,1\,2)$
41.025	1.88×10^{-3}	$Eu(OH)_3$	(2 0 1)
43.475	4.56×10^{-4}	Monoclinic	$(5\,1\,\bar{2})$
49.708	1.24×10^{-3}	-	-
50.457	41.76×10^{-3}	Cubic	(4 2 2)
58.133	49.66×10^{-4}	-	-
66.350	44.28×10^{-4}	$Eu(OH)_3$	(3 1 1)

Table 6.1: Summary of the XRD peak positions, intensity and identified reflections.

ichiometry is in progress.

6.3 Thermodynamic and elastic properties

From the Eu-partial phonon DOS a variety of thermodynamic and elastic properties can be calculated as discussed in section 2.1.3. The temperature dependencies of selected thermoelastic properties of cubic Eu_2O_3 obtained from the *ab initio* calculated phonon DOS are shown in figure 6.5. The temperature dependent thermoelastic properties of EuO obtained from the *ab initio* calculated phonon DOS are also shown in the same figure for comparison. The thermoelastic properties of the monoclinic Eu_2O_3 are not discussed due to the observed imaginary phonon frequencies in the *ab initio* calculated phonon DOS.

Figure 6.5(a) plots the Lamb-Mössbauer factor of Eu_2O_3 and EuO as a function of temperature. Both oxides show an exponential decay of their f_{LM} as the temperature increases, with f_{LM} of the sesquioxide being larger than that of the monoxide in the entire temperature range. Classically, f_{LM} along wave vector $\vec{k}$ is given by $-exp[-\vec{k}^2 < A^2_{vib} >]$. The atomic vibrational amplitude A_{vib} as function of temperature is shown in figure 6.5(b). The vibrational amplitude of Eu atoms in EuO is larger than that in Eu_2O_3. This indicates that EuO lattice is relatively less rigid and more prone to multiphonon excitations compared to Eu_2O_3. The mean interatomic force constants obtained from the third moment of the Eu partial phonon DOS is $38.4\,Nm^{-1}$ and $78.5\,Nm^{-1}$ for EuO and Eu_2O_3, respectively. This parameter is similar to stiffness in mechanics, higher K of Eu_2O_3 implies its greater lattice stiffness. The vibrational entropy as a function of temperature is presented in figure 6.5(c), the relatively higher vibrational amplitude of Eu atoms in EuO lattice compare to Eu_2O_3 lattice results in larger values of the vibrational entropy of EuO in the entire temperature range. Figure 6.5(d) shows the lattice specific heat as a

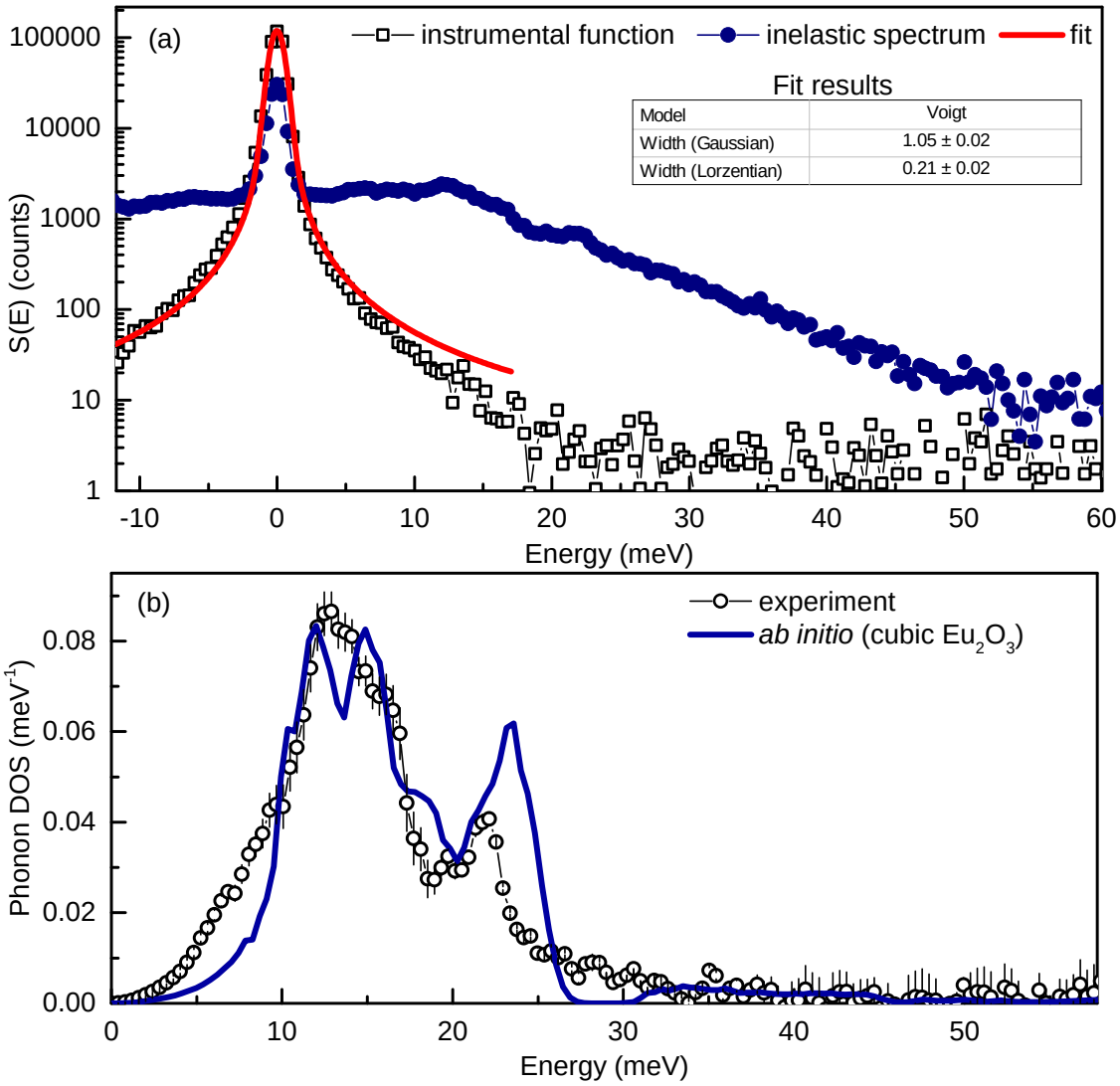

Figure 6.4: (a) NIS spectrum (blue/circles) of the pellet and instrumental function (black/squares) collected at room temperature. The fit to the instrumental function (red/solid line) and the obtained values of the fit parameters are shown.(b) The Eu-partial phonon DOS of the Eu_2O_3 pellet (black/circles) and *ab initio* calculated phonon DOS (blue/solid line) of cubic Eu_2O_3 convoluted with a Gaussian curve of FWHM=1.5 meV.

function of temperature. Regardless of the difference in stoichiometry and structure, C_v of both oxides saturates around 450 K to the limit of $3k_B$ per atom as suggested by the equipartition principle. In the low temperature limit, for $T \leq 50K$, the C_v varies proportionally to T^3 indicated by the black/dashed curve. Additionally, the internal energy and the kinetic energy of the Eu atoms were calculated as a function of temperature and are depicted in figure 6.5(e) and (f), respectively. Both parameters show a monotonous linear increase with increasing temperature and have approximately the same values for both the oxides.

Figure 6.6(a) compares the *ab initio* calculated Eu-partial and O-partial phonon

DOS of cubic Eu_2O_3 and EuO. The phonon DOS of EuO is shifted to lower energies compared to Eu_2O_3 that extends up to 70 meV. The figure clearly shows that in the case of Eu_2O_3 vibrational states of O atoms extend well below 30 meV, this indicates the weak coupling of the vibrations O atoms to that of Eu atoms. On the other hand this behaviour is absent in EuO. Figure 6.6(b) compares the reduced Eu-partial phonon DOS ($g(E)/E^2$) of the cubic sesquioxide and the monoxide. The speed of sound v_s is calculated from the Debye level, the low energy ($E < 7$ meV) region, according to equation 6.1 [33]:

$$\lim_{E\to 0} \frac{g(E)}{E^2} = \frac{m_R}{2\pi^2\hbar^3\rho v_s}, \tag{6.1}$$

where m_R is the mass of the resonant nuclei and ρ is the mass density. The speed of sound calculated for EuO and Eu_2O_3 are 2.46 km/s and 2.89 km/s, respectively. In a simple Debye solid, thermal conductivity λ is given as:

$$\lambda = \frac{1}{3} C_v \tau v_s^2, \tag{6.2}$$

where C_v is specific heat capacity and τ is average phonon relaxation time. The v_s of Eu_2O_3 is 17% greater than that of EuO, this implies that the lattice thermal conductivity of Eu_2O_3 is approximately 37% larger than that of EuO, assuming that the average phonon relaxation times are similar for both oxides.

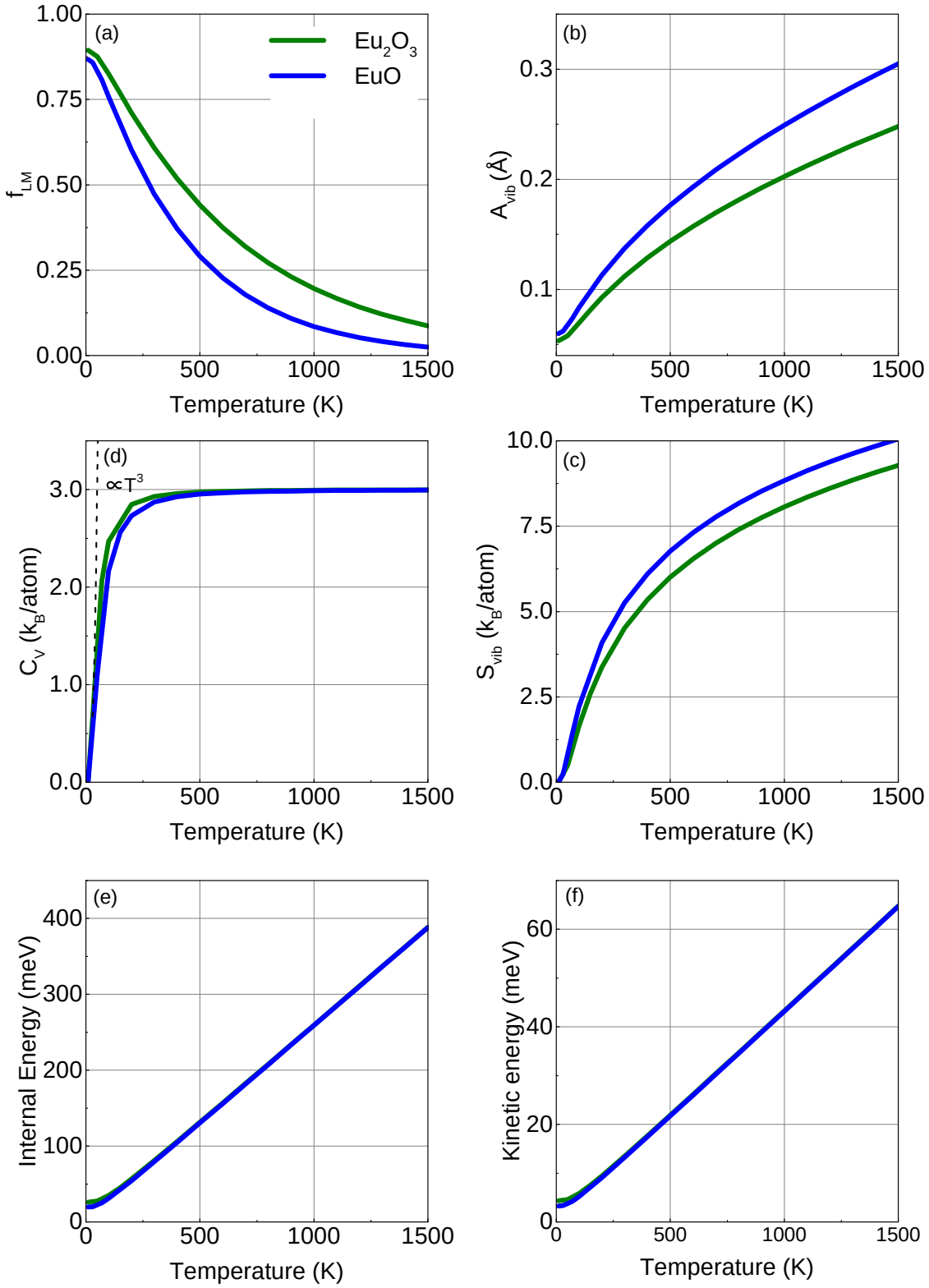

Figure 6.5: Temperature dependence of selected thermodynamic and elastic properties of EuO and Eu_2O_3.

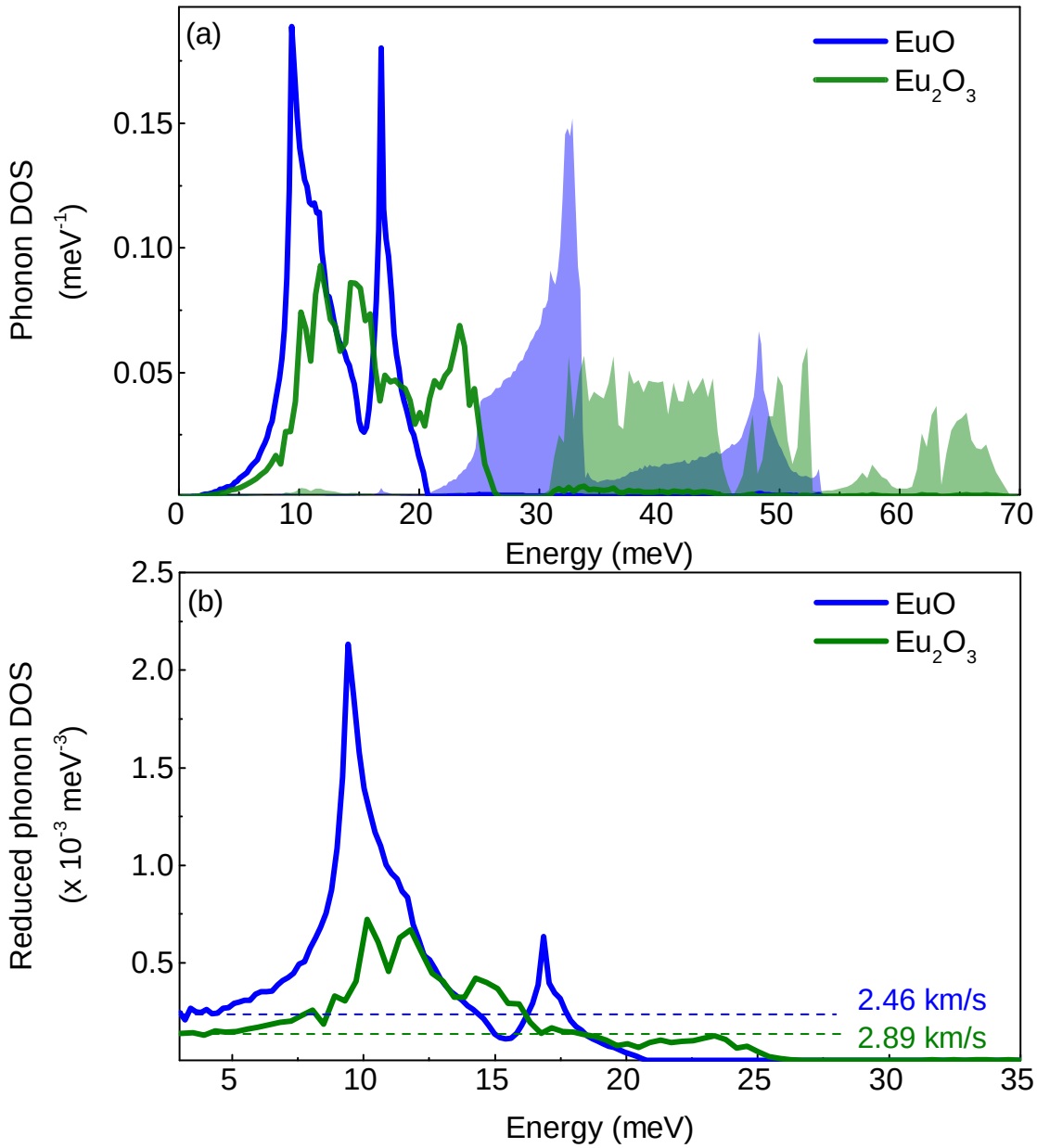

Figure 6.6: (a) Comparison between *ab initio* calculated phonon DOS of cubic Eu_2O_3 and EuO. The Eu-partial phonon DOS are indicated by solid lines and the corresponding O-partial phonon DOS by shaded areas. (b) *Ab initio* calculated reduced phonon DOS of Eu_2O_3 and EuO. The horizontal dashed lines indicate the corresponding Debye levels. The calculated speed of sound of both oxides from their respective Debye levels are shown.

6.4 Conclusions

The lattice dynamics of cubic Eu_2O_3 was determined using *ab initio* calculations. Several temperature dependent Eu-partial thermodynamic and elastic properties of Eu_2O_3 were calculated. The *ab initio* calculations for the monoclinic phase of Eu_2O_3 resulted in soft phonon modes and was found to be unstable in the calculations. A comparative study of the lattice dynamics of Eu_2O_3 and EuO was performed. The Eu-partial phonon spectrum of Eu_2O_3 extends over a larger energy range compared to EuO. The crystal lattice of cubic Eu_2O_3 was found to be more rigid compared to EuO which is evidenced by the higher value of mean force constant and lower mean squared atomic displacement of Eu atoms in Eu_2O_3. An attempt to experimentally obtain the phonon DOS of Eu_2O_3 using nuclear inelastic scattering on a commercially available Eu_2O_3 powder sample was made. However, the sample had contaminations from $Eu(OH)_3$ and monoclinic phase of Eu_2O_3. This hindered the experimental validation of the *ab initio* calculated phonon DOS. Even though Eu_2O_3 is considered stable at ambient condition, the hygroscopic nature of Eu_2O_3 resulted in the formation of $Eu(OH)_3$, implying that ultra high vacuum condition is required for the preparation of high quality stoichiometric single crystalline Eu_2O_3 for further experiments.

Chapter 7

Conclusions

The thesis presents a combined experimental and theoretical study of the lattice dynamics of epitaxial bulk-like film and ultrathin films of EuO, and a powder sample of Eu_2O_3.

EuO is a rare semiconducting ferromagnet with a Curie temperature of 69 K and a model system for Heisenberg ferromagnets. Even though it was discovered in the early 60s and has been extensively investigated, its lattice dynamics remained to a large extend unknown. The main difficulty is related with obtaining single crystalline and stoichiometric samples of high purity that are necessary for the lattice dynamics investigations. Another obstacle is the very high absorption cross section of Eu for thermal neutrons that makes the inelastic neutron scattering inapplicable for lattice dynamics studies of this material. To overcome these difficulties, epitaxial EuO(001) films were grown by reactive molecular epitaxy under ultrahigh vacuum condition and covered with a protective layer to prevent further oxidation. The lattice dynamics was investigated by a combination of state of the art x-ray scattering techniques and first-principles theory. A 100 nm thick EuO(0 0 1) film was grown on yttrium stabilised zirconia YSZ(0 0 1) using an optimized procedure reported by Sutarto *et. al.* [48] and covered with a 10 nm thick Nb layer to prevent further oxidation. The sample was structurally characterized using RHEED and XRD, while the chemical composition and stoichiometry were confirmed with x-ray photoelectron spectroscopy and nuclear forward scattering. Phonon dispersion curves along Γ-X and Γ-K-X directions at 295 K and 30 K were measured using inelastic x-ray scattering at ID28 of the ESRF-The European Synchrotron. Additionally, the Γ-X branch was measured at 90 K. The phonon energies determined in the IXS experiment were found to be in excellent agreement with the results from *ab initio* calculations, except for a softening near the X point at 90 K and below. Surprisingly, the phonon linewidths of the TA modes along Γ-X direction showed a five-fold increase towards the X point at T≤90 K, and the phonon linewidths of the LA modes along Γ-K-X showed an increase by a factor of 1.6. At the same time the widths of the TA phonons along Γ-K-X and of LA phonons along Γ-X directions

remained temperature independent. With the aid of *ab initio* calculations, the observed phenomenon was attributed to a giant and anisotropic spin-phonon coupling in EuO in the vicinity and below the Curie temperature. The estimated value of the spin-phonon coupling constant of about 10 is among the largest ever reported spin-phonon coupling constants in literature. The presence of this phenomenon is further evidenced by the broadening of the phonon peak related to the TA phonons in the Eu-partial phonon DOS measured at 295 K, 90 K, 70 K, 50 K and 30 K by nuclear inelastic scattering at ID18 of the ESRF. The discovered effect implies that at temperatures near the Curie temperature and below, phonons in EuO could excite spin waves and vice versa. The anisotropic nature of the spin-phonon coupling suggests that spin relaxations along the Γ-K-X direction is less probable compared to the Γ-X direction. This might have important implications for the design of EuO based spintronic devices.

The lattice dynamics of paramagnetic EuO(001) ultrathin films of thickness 1, 2 and 45 MLs grown on yttrium aluminate YAO(0 0 1) were studied by *in situ* nuclear inelastic scattering. The single crystalline quality and chemical purity of the films were confirmed by RHEED and nuclear forward scattering. The Eu-partial DOS was measured by *in situ* nuclear inelastic scattering. Similarly to the results on the Fe(110) surface [149] and Fe(110) thin films [131], the broken translation symmetry at the surface has drastic impact on the lattice dynamics of the EuO(001) films. A pronounced enhancement of the phonon states at low energies and suppression of the high-energy phonon modes were clearly observed in the phonon DOS of 1ML sample with the features approaching the bulk-like phonon DOS with increasing film thickness. The phonon DOS of 2 ML thick film was reliably reproduced by a combination of phonon DOS of the Eu(001) surface, represented by the 1 ML sample and the bulk EuO, represented by the 45 ML sample and including phonon lifetime broadening by the damped harmonic oscillator function. In addition to the standard way of phonon DOS decomposition to the surface and bulk components, in the case of the 2ML sample, an alternative approach that accounts for the differences in the Lamb-Mössbauer factors of the surface and sub-surface layers of the film was introduced. Although the obtained phonon DOS showed similar features, the obtained relative contribution of surface phonons with respect to the bulk phonons was higher by 12% for the latter approach. The difference most likely originates from the erroneous estimation of multiphonon excitations in the standard approach and also the relatively low statistics of the experimental data of the 1ML and 2ML samples. The experimental data of the ultrathin EuO films were comprehensively understood by the help of *ab initio* calculated phonon DOS of the Eu(001) surface. The direct comparison of the DOS of 1ML sample with the *ab initio* calculated DOS of the native EuO(001) surface revealed a certain level of discrepancy. This is attributed to the fact that the EuO monolayer was deposited on a substrate of

different material, which effects the atomic vibrations of the film. This assumption is further supported by the fact that the features of the DOS of the 2 ML sample, in which the influence of the substrate is shielded by the sub-surface layer, correspond closely to that of the calculated EuO(001) surface. The experimentally observed overall shift of the phonon DOS to lower energies is expected to increase the spin-phonon coupling in ultrathin EuO films, since the spin waves in EuO span up to approximately 6 meV. This coupling of spin waves to surface phonons in EuO films and in particular in ultrathin interfaces that are of technological importance is a topic that deserves further investigation.

The thermoelastic properties of the ultrathin films showed deviation from the bulk values. The vibrational amplitude and vibrational entropy are increased by 28% and 10%, respectively, as the film thickness is reduced from 45ML to 1ML. This decrease in lattice rigidity is consistent with the observed 12% reduction in the mean force constant of the 1ML sample compared to the 45ML sample. Unlike other thermoelastic properties, lattice specific heat capacity remained constant within error limits with respect to the film thickness. The magnitude of the thermoelastic properties of the 2ML sample calculated from the phonon DOS obtained via the both approaches were found to be similar and were between that of the 1ML and bulk-like samples.

Lattice dynamics of the technologically important material Eu_2O_3 was investigated using a combination of *ab initio* calculations and nuclear inelastic scattering. The sample used for the experiment was a Eu_2O_3 pellet that was made out of a commercially available Eu_2O_3 powder. The structural characterization of the pellet using XRD revealed the presence of a mixture of monoclinic and cubic phase of Eu_2O_3. In addition, the XRD data evidenced the presence of $Eu(OH)_3$ formed due the hygroscopic nature of Eu_2O_3. Phonon dispersions and phonon DOS of the monoclinic and cubic phases of Eu_2O_3 were calculated by our collaboration partner. The monoclinic phase was found to be unstable in calculations due to the observed soft phonon modes. Even though the main features of the experimentally obtained phonon DOS were reproduced by the calculated DOS of the cubic Eu_2O_3, a reliable agreement between experiment and theory was not obtained mainly due to impurities in the powder sample. A comparative study of the phonon DOS and temperature-dependent thermoelastic properties of cubic Eu_2O_3 and EuO was performed in the range 0-1500 K. The Eu-partial phonon DOS of Eu_2O_3 extends over a larger energy range compared to that of EuO. The lattice of Eu_2O_3 was found to be stiffer, evidenced by the mean force constant that is approximately twice in magnitude compared to that of EuO. This results in lower vibrational entropy and vibrational amplitude of Eu atoms in Eu_2O_3. On the other hand, the lattice specific heat and the internal energy remained similar for both oxides in the temperature range.

The results presented in this thesis uncovered a giant coupling between lattice vibrations and spin waves in EuO, which is regarded as a model system for Heisenberg ferromagnets. Such interplay between several degrees of freedom in a crystal provides handles to tailor physical properties of materials. The phonon DOS of ultrathin films reveals changes in the lattice dynamics of the EuO surface. This opens up a very interesting question about the magnitude of spin-phonon coupling in functional EuO ultrathin films and interfaces. The presented results also demonstrate that *in situ* nuclear inelastic scattering is an ideal experimental technique to probe spin-phonon interactions in materials from bulk to a single atomic layer.

Bibliography

[1] Lindenberg, A. M., Kang, I., Johnson, S. L., Missalla, T., Heimann, P. A., Chang, Z., Larsson, J., Bucksbaum, P. H., Kapteyn, H. C., Padmore, H. A., Lee, R. W., Wark, J. S., and Falcone, R. W. *Physical Review Letters* **84**, 111 (2000).

[2] Cavalleri, A., Wall, S., Simpson, C., Statz, E., Ward, D. W., Nelson, K. A., Rini, M., and Schoenlein, R. W. *Nature* **442**, 664 (2006).

[3] Mook, H. A., Chakoumakos, B. C., Mostoller, M., Boothroyd, A. T., and Paul, D. M. *Physical Review Letters* **69**, 2272 (1992).

[4] Snyder, G. J. and Toberer, E. S. *Nature Materials* **7**, 105 (2008).

[5] Biswas, K., He, J., Blum, I. D., Wu, C.-I., Hogan, T. P., Seidman, D. N., Dravid, V. P., and Kanatzidis, M. G. *Nature* **489**, 414 (2012).

[6] Maldovan, M. *Nature* **503**, 209 (2013).

[7] Maldovan, M. *Physical Review Letters* **110**, 025902 (2013).

[8] Maldovan, M. *Nature Materials* **14**, 667 (2015).

[9] Balandin, A. A. *Journal of Nanoscience and Nanotechnology* **5**, 1015 (2005).

[10] Wang, L. and Li, B. *Physical Review Letters* **99**, 177208 (2007).

[11] Wachter, P. *Hand book on the Physics and Chemistry of Rare Earths*. Elsevier, (1972).

[12] Greiner, J. H. and Fan, G. J. *Applied Physics Letters* **9**(1), 27 (1966).

[13] Ahn, K. *Journal of Applied Physics* **39**, 5061 (1968).

[14] Shapira, Y., Foner, S., and Aggarwal, R. *Physical Review B* **8**, 2316 (1973).

[15] Torrance, J. B., Shafer, M. W., and McGuire, T. R. *Physical Review Letters* **29**, 1168 (1972).

[16] Melville, A., Mairoser, T., Schmehl, A., Birol, T., Heeg, T., Hollander, B., Schubert, J., Fennie, C. J., and Schlom, D. G. *Applied Physics Letters* **102**, 062404 (2013).

[17] Yamasaki, T., Ueno, K., Tsukazaki, A., Fukumura, T., and Kawasaki, M. *Applied Physics Letters* **98**, 4 (2011).

[18] Steeneken, P. G., Tjeng, L. H., Elfimov, I., Sawatzky, G. a., Ghiringhelli, G., Brookes, N. B., and Huang, D.-J. *Physical Review Letters* **88**, 047201 (2002).

[19] Caspers, C., Gloskovskii, A., Gorgoi, M., Besson, C., Luysberg, M., Rushchanskii, K. Z., Ležaić, M., Fadley, C. S., Drube, W., and Müller, M. *Scientific Reports* **6**, 22912 (2016).

[20] Grünberg, P., Güntherodt, G., Frey, A., and Kress, W. *Physica B+C* **89**, 225 (1977).

[21] Güntherodt, G., Merlin, R., and Grünberg, P. *Physical Review B* **20**, 2834 (1979).

[22] Zeyher, R. and Kress, W. *Physical Review B* **20**, 2850 (1979).

[23] Wallace, R. M. and Wilk, G. *MRS Bulletin* **27**, 186 (2002).

[24] Fischetti, M. V., Neumayer, D. A., and Cartier, E. A. *Journal of Applied Physics* **90**, 4587 (2001).

[25] Chen, Y.-L. and Yang, D.-P. *Mössbauer Effect in Lattice Dynamics: Experimental Techniques and Applications*. John Wiley and Sons Inc, (2007).

[26] Fultz, B. *Progress in Materials Science* **55**, 247 (2010).

[27] Fultz, B., Stephens, T. A., Alp, E. E., Hu, M. Y., Sutter, J. P., Toellner, T. S., and Sturhahn, W. *Physical Review B* **61**, 14517 (2000).

[28] Vela, S., Mota, F., Deumal, M., Suizu, R., Shuku, Y., Mizuno, A., Awaga, K., Shiga, M., Novoa, J. J., and Ribas-Arino, J. *Nature Communications* **5** (2014).

[29] Kürpick, U., Kara, A., and Rahman, T. S. *Physical Review Letters* **78**, 1086 (1997).

[30] Claudio, T., Bessas, D., Birke, C. S., Kieslich, G., Panthöfer, M., Sergueev, I., Tremel, W., and Hermann, R. P. *Physica Status Solidi (B) Basic Research* **251**, 919 (2014).

[31] Bessas, D., Winkler, M., Sergueev, I., König, J. D., Böttner, H., and Hermann, R. P. *Physica Status Solidi (A)* **213**, 694 (2016).

[32] Kittel, C. *Introduction To Solid State Physics.* John Wiley and Sons Inc, 8th edition, (1966).

[33] Hu, M., Sinn, H., Alatas, A., Sturhahn, W., Alp, E., Willie, H.-C., Shvyd'ko, Y., Sutter, J., Bandaru, J., Haller, E., Ozhogin, V., Rodriguez, S., Colella, R., Kartheuser, E., and Villeret, M. *Physical Review B* **69**, 113306 (2004).

[34] Pop, E., Sinha, S., and Goodson, K. *Proceedings of the IEEE* **94**, 1587 (2006).

[35] Sharma, V. K. *Mössbauer spectroscopy : Applications in chemistry, biology, and nanotechnology.* Wiley, Hoboken, New Jersey, (2013).

[36] Hu, M. Y., Toellner, T. S., Dauphas, N., Alp, E. E., and Zhao, J. *Physical Review B* **87**, 064301 feb (2013).

[37] Hohenberg, P. and Kohn, W. *Physical Review* **136**, 864 (1964).

[38] Jones, R. O. and Gunnarsson, O. *Review of Modern Physics* **61**, 689 (1989).

[39] Perdew, J. P., Burke, K., and Ernzerhof, M. *Physical Review Letters* **77**, 3865 (1996).

[40] Kohn, W., Becke, A. D., and Parr, R. G. *The Journal of Physical Chemistry* **100**, 12974 (1996).

[41] Perdew, J. P., Burke, K., and Ernzerhof, M. *Physical Review Letters* **78**, 1396 (1997).

[42] Kohn, W. and Sham, L. J. *Physical Review* **140**, A1133 (1965).

[43] Parlinski, K., Li, Z. Q., and Kawazoe, Y. *Physical Review Letters* **78**, 4063 may (1997).

[44] Kresse, G. and Furthmüller, J. *Computational Materials Science* **6**, 15 (1996).

[45] Blöchl, P. E. *Physical Review B* **50**, 17953 (1994).

[46] Jäger, R. *Surface Science* **500**, 189 (2002).

[47] Herman, M. A., Richter, W., and Sitter, H. *Epitaxy : physical principles and technical implementation.* Springer Berlin, (2004).

[48] Sutarto, R., Altendorf, S. G., Coloru, B., Moretti Sala, M., Haupricht, T., Chang, C. F., Hu, Z., Schüßler-Langeheine, C., Hollmann, N., Kierspel, H., Hsieh, H. H., Lin, H.-J., Chen, C. T., and Tjeng, L. H. *Physical Review B* **79**, 205318 (2009).

[49] Lüth, H. *Surfaces and Interfaces of Solid Materials*. Springer Berlin-Heidelberg, (1995).

[50] Stankov, S., Ruffer, R., Sladecek, M., Rennhofer, M., Sepiol, B., Vogl, G., Spiridis, N., Slezak, T., and Korecki, J. *Review of Scientific Instruments* **79**(4), 045108 (2008).

[51] Lin Wang, Z. *Reflection Electron Microscopy and Spectroscopy*. Cambridge University Press, (1996).

[52] Watts, J. F. *Vacuum* **45**, 653 (1994).

[53] Briggs, D. and Grant, J. *Surface analysis by Auger and X-ray photoelectron spectroscopy*. IM Publications, (2003).

[54] Mössbauer, R. L. *Zeitschrift für Physik* **151**, 124 (1958).

[55] Röhlsberger, R. *Nuclear condensed matter physics with synchrotron radiation basic principles, methodology and applications*. Springer, (2004).

[56] Barb, D. and Meisel, W. *Grundlagen und Anwendungen der Mössbauerspektroskopie / von Dnil Barb. Bearb. u. hrsg. von Werner Meisel. [Aus d. Rumän. übertr. von Günter Glanz]*. Ed. Acad. Republicii Socialiste Romania, (1980).

[57] Andreeva, M. A. *Hyperfine Interactions* **185**, 17 (2008).

[58] Sturhahn, W., Toellner, T. S., Alp, E. E., Zhang, X., Ando, M., Yoda, Y., Kikuta, S., Seto, M., Kimball, C. W., and Dabrowski, B. *Physical Review Letters* **74**, 3832 (1995).

[59] Seto, M., Yoda, Y., Kikuta, S., Zhang, X. W., and Ando, M. *Physical Review Letters* **74**, 3828 (1995).

[60] Chumakov, A. I., Rüffer, R., Baron, A. Q. R., Grünsteudel, H., Grünsteudel, H. F., and Kohn, V. G. *Physical Review B* **56**, 10758 (1997).

[61] Kohn, V. G., Chumakov, A. I., and Rüffer, R. *Physical Review B* **58**, 8437 (1998).

[62] Singwi, K. S. and Sjölander, A. *Physical Review* **120**, 1093 (1960).

[63] Marshall, W. and Lovesey, S. W. *Theory of thermal neutron scattering: the use of neutrons for the investigation of condensed matter*. Oxford University Press, 1st edition, (1971).

[64] Lipkin, H. J. *Annals of Physics* **9**, 332 (1960).

[65] Lipkin, H. J. *Physical Review B* **52**, 10073 (1995).

[66] Toellner, T. S., Hu, M. Y., Sturhahn, W., Quast, K., and Alp, E. E. *Applied Physics Letters* **71**(15), 2112 (1997).

[67] Kohn, V. G. and Chumakov, A. I. *Hyperfine Interactions* **125**, 205 (2000).

[68] Leupold, O., Pollmann, J., Gerdau, E., Rüter, H. D., Faigel, G., Tegze, M., Bortel, G., Rüffer, R., Chumakov, a. I., and Baron, a. Q. R. *Europhysics Letters* **35**, 671 (1996).

[69] Krisch, M., Sette, F., Cardona, M., and Merlin, R. *Light Scattering in Solid IX*, volume 108 of *Topics in Applied Physics*. Springer Berlin-Heidelberg, (2006).

[70] Okada, Y. and Tokumaru, Y. *Journal of Applied Physics* **56**, 314 (1984).

[71] Shafer, M. W. *Journal of Applied Physics* **39**, 588 (1968).

[72] Melville, A., Mairoser, T., Schmehl, A., Fischer, M., Gsell, S., Schreck, M., Awschalom, D. D., Heeg, T., Hollander, B., Schubert, J., and Schlom, D. G. *Applied Physics Letters* **103**, 222402 (2013).

[73] Lee, K. *Journal of Applied Physics* **41**, 954 (1970).

[74] Jutong, N., Eckern, U., Mairoser, T., and Schwingenschlögl, U. *Scientific Reports* **5**, 8038 (2015).

[75] Shafer, M. W. *Journal of Applied Physics* **36**, 1145 (1965).

[76] Shafer, M., Torrance, J., and Penney, T. *Journal of Physics and Chemistry of Solids* **33**, 2251 (1972).

[77] Paparoditis, C., Suryanarayanan, R., Llinares, C., Monteil, E., and Bordure, G. *Solid State Communications* **9**, 1871 (1971).

[78] Kie Ahn and Suits, J. *IEEE Transactions on Magnetics* **3**, 453 (1967).

[79] Massenet, O. *Journal of Applied Physics* **45**, 3593 (1974).

[80] Steeneken, P. *New light on EuO thin films*. PhD thesis, (2002).

[81] Caspers, C., Müller, M., Gray, A., Kaiser, A. M., Gloskovskii, A., Fadley, C. S., Drube, W., and Schneider, C. M. *Physical Review B* **84**, 205217 (2011).

[82] Schmehl, A., Vaithyanathan, V., Herrnberger, A., Thiel, S., Richter, C., Liberati, M., Heeg, T., Röckerath, M., Kourkoutis, L. F., Mühlbauer, S., Böni, P., Muller, D. a., Barash, Y., Schubert, J., Idzerda, Y., Mannhart, J., and Schlom, D. G. *Nature Materials* **6**, 882 (2007).

[83] Ghosh, D. B., De, M., and De, S. K. *Physical Review B* **70**, 115211 (2004).

[84] Santos, T. S., Moodera, J. S., Raman, K. V., Negusse, E., Holroyd, J., Dvorak, J., Liberati, M., Idzerda, Y. U., and Arenholz, E. *Physical Review Letters* **101**, 147201 (2008).

[85] Dionne, G. F. *Magnetic oxides*. Springer Verlag, (2005).

[86] Chaikin, P. M. and Lubensky, C. *Principles of condensed matter physics*. Cambridge University Press, (2000).

[87] Huang, C.-C. and Ho, J. T. *Physical Review B* **12**, 5255 (1975).

[88] Menyuk, N., Dwight, K., and Reed, T. B. *Physical Review B* **3**, 1689 (1971).

[89] Mauger, A. and Godart, C. *Physics Reports* **141**, 51 (1986).

[90] Mook, H. A. *Physical Review Letters* **46**, 508 (1981).

[91] Kasuya, T. *Journal of Alloys and Compounds* **192**, 11 (1993).

[92] Schiller, R. and Nolting, W. *Physical Review Letters* **86**, 3847 (2001).

[93] Muller, M., Miao, G.-X., and Moodera, J. S. *Journal of Applied Physics* **105**, 07C917 (2009).

[94] Peters, V., Petermann, K., Huber, G., Larionov, M., Speiser, J., and Giesen, A. In *Advanced Solid-State Lasers*, 150 (OSA, Washington, D.C., 2002).

[95] Fornasiero, L., Mix, E., Peters, V., Petermann, K., and Huber, G. *Crystal Research and Technology* **34**, 255 (1999).

[96] Saiki, A., Ishizawa, N., Mizutani, N., and Kato, M. *Journal of the Ceramic Association of Japan* **93**, 649 (1985).

[97] Chen, G., Peterson, J., and Brister, K. *Journal of Solid State Chemistry* **111**(2), 437 (1994).

[98] Brauer, G. *Structural and solid state chemistry of pure rare earth oxides*, volume 2. Pergamon Press, 1st edition, (1966).

[99] Foex, M. *Zeitschrift für Anorganische und Allgemeine Chemie* **333**, 313 (1965).

[100] Adachi, G., Imanaka, N., and Kang, Z. C. *Binary rare earth oxides*. Kluwer Academic Publishers, Dordrecht, (2005).

[101] Mahanti, H. and Barnes, R. *Applied Spectroscopy* **37**, 261 (1983).

[102] Zhang, T., Ou, X., Zhang, W., Yin, J., Xia, Y., and Liu, Z. *Journal of Physics D: Applied Physics* **47**, 065302 (2014).

[103] Lin, Y., Wang, H., Hawley, M. E., Foltyn, S. R., Jia, Q. X., Collis, G. E., Burrell, A. K., and McCleskey, T. M. *Applied Physics Letters* **85**, 3426 (2004).

[104] Yen, L.-C., Hu, C.-W., Chiang, T.-Y., Chao, T.-S., and Pan, T.-M. *Applied Physics Letters* **100**, 173509 (2012).

[105] Concas, G., Dewhurst, J. K., Sanna, A., Sharma, S., and Massidda, S. *Physical Review B* **84**, 014427 (2011).

[106] Fanciulli, M. and Scarel, G., editors. *Rare Earth Oxide Thin Films*. Topics in Applied Physics. Springer Berlin Heidelberg, (2006).

[107] Prokofiev, A., Shelykh, A., and Melekh, B. *Journal of Alloys and Compounds* **242**, 41 (1996).

[108] Rao, G., Ramdas, S., Mehrotra, P., and Rao, C. *Journal of Solid State Chemistry* **2**, 377 (1970).

[109] Nakane, H., Noya, A., Kuriki, S., and Matsumoto, G. *Thin Solid Films* **59**, 291 (1979).

[110] Ohmi, S., Kobayashi, C., Kashiwagi, I., Ohshima, C., and Iwai, H. *Journal of Electrochemical Society* **150**, 134 (2005).

[111] Yamada, H., Shimizu, T., Kurokawa, A., Ishii, K., and Suzuki, E. *Journal of Electrochemical Society* **150**, 429 (2003).

[112] Nishikawa, Y., Yamaguchi, T., Yoshiki, M., Satake, H., and Fukushima, N. *Applied Physics Letters* **81**, 4386 (2002).

[113] Xue, D., Betzler, K., and Hesse, H. *Journal of Physics: Condensed Matter* **12**, 3113 (2000).

[114] Tsang, J. C., Dresselhaus, M. S., Aggarwal, R. L., and Reed, T. B. *Physical Review B* **9**, 984 (1974).

[115] Ulbricht, R. W., Schmehl, A., Heeg, T., Schubert, J., and Schlom, D. G. *Applied Physics Letters* **93**, 102105 (2008).

[116] Itoh, T., Mori, M., Inukai, M., Nitani, H., Yamamoto, T., Miyanaga, T., Igawa, N., Kitamura, N., Ishida, N., and Idemoto, Y. *Journal of Physical Chemistry C* **119**, 8447 (2015).

[117] Cunningham, G. *Reactor Materials* **6**, 63 (1963).

[118] Pradip, R., Piekarz, P., Bosak, A., Merkel, D. G., Waller, O., Seiler, A., Chumakov, A. I., Rüffer, R., Oleś, A. M., Parlinski, K., Krisch, M., Baumbach, T., and Stankov, S. *Physical Review Letters* **116**, 185501 (2016).

[119] Wickman, H. H. *Journal of Applied Physics* **39**, 1248 (1968).

[120] Ingle, N. J. C. and Elfimov, I. S. *Physical Review B* **77**, 121202 (2008).

[121] Anisimov, V. I., Zaanen, J., and Andersen, O. K. *Physical Review B* **44**, 94 (1991).

[122] Busch, G., Güntherodt, G., and Wachter, P. *Le Journal de Physique Colloques* **32**, 928 (1971).

[123] Rüffer, R. and Chumakov, A. I. *Hyperfine Interactions* **97**, 589 (1996).

[124] Kornblit, A. and Ahlers, G. *Physical Review B* **11**, 2678 (1975).

[125] Ahn, K., Pecharsky, A. O., Gschneidner, K. A., and Pecharsky, V. K. *Journal of Applied Physics* **97**, 063901 (2005).

[126] Argyle, B. E., Miyata, N., and Schultz, T. D. *Physical Review* **160**, 413 (1967).

[127] Martin, J. J. and Dixon, G. S. *Physica Status Solidi (B)* **54**, 707 (1972).

[128] Cason, R. G. and John, L. *Helvetica Physica Acta* **41**, 1045 (1968).

[129] Ulrich, C., Khaliullin, G., Guennou, M., Roth, H., Lorenz, T., and Keimer, B. *Physical Review Letters* **115**, 156403 (2015).

[130] Bosak, A., Schmalzl, K., Krisch, M., van Beek, W., and Kolobanov, V. *Physical Review B* **77**, 224303 (2008).

[131] Stankov, S., Röhlsberger, R., Ślęzak, T., Sladecek, M., Sepiol, B., Vogl, G., Chumakov, A. I., Rüffer, R., Spiridis, N., Łażewski, J., Parliński, K., and Korecki, J. *Physical Review Letters* **99**, 185501 (2007).

[132] Böni, P. and Shirane, G. *Physical Review B* **33**, 3012 (1986).

[133] Chaudhury, R. and Shastry, B. S. *Physical Review B* **37**, 5216 (1988).

[134] Young, a. P. and Shastry, B. S. *Journal of Physics C: Solid State Physics* **15**, 4547 (1982).

[135] Tao, X., Landau, D. P., Schulthess, T. C., and Stocks, G. M. *Physical Review Letters* **95**, 087207 (2005).

[136] Antropov, V. *Physical Review B* **72**, 140406 (2005).

[137] Zhou, S. M., Guo, Y. Q., Zhao, J. Y., Zhao, S. Y., and Shi, L. *Applied Physics Letters* **96**, 262507 (2010).

[138] Dietrich, O. W., Als-Nielsen, J., and Passell, L. *Physical Review B* **14**, 4923 (1976).

[139] Lüthi, B. and Pollina, R. J. *Physical Review Letters* **22**, 717 (1969).

[140] Cheng, T. M. and Li, L. *Journal of Magnetism and Magnetic Materials* **320**, 1 (2008).

[141] Passell, L., Dietrich, O. W., and Als-Nielsen, J. *Physical Review B* **14**, 4897 (1976).

[142] Normand, B., Kohno, H., and Fukuyama, H. *Physical Review B* **53**, 856 (1996).

[143] Werner, R., Gros, C., and Braden, M. *Physical Review B* **59**, 14356 (1999).

[144] Calder, S., Lee, J. H., Stone, M. B., Lumsden, M. D., Lang, J. C., Feygenson, M., Zhao, Z., Yan, J.-Q., Shi, Y. G., Sun, Y. S., Tsujimoto, Y., Yamaura, K., and Christianson, A. D. *Nature Communications* **6**, 8916 (2015).

[145] Baltensperger, W. and Helman, J. S. *Helvetica Physica Acta* **41**, 668 (1968).

[146] Parratt, L. G. *Physical Review* **95**, 359 (1954).

[147] Braun, C. *Paratt32 [computer program] retrived from http://www.hmi.de/bensc/software/index2.html* .

[148] Kara, A. and Rahman, T. S. *Surface Science Reports* **56**, 159 (2005).

[149] Ślęzak, T., Łażewski, J., Stankov, S., Parlinski, K., Reitinger, R., Rennhofer, M., Rüffer, R., Sepiol, B., Ślęzak, M., Spiridis, N., Zając, M., Chumakov, A. I., and Korecki, J. *Physical Review Letters* **99**, 066103 (2007).

[150] Fultz, B., Ahn, C., Alp, E. E., Sturhahn, W., and Toellner, T. S. *Physical Review Letters* **79**, 937 (1997).

[151] Röhlsberger, R., Sturhahn, W., Toellner, T. S., Quast, K. W., Hession, P., Hu, M., Sutter, J., and Alp, E. E. *Journal of Applied Physics* **86**, 584 (1999).

[152] Glyde, H. R. and Svensson, E. C. In *Methods in Experimental Physics: Neutron Scattering,* David, P. L. and Sköld, K., editors, 303. (1987).

Appendix

Matlab script for fitting phonon DOS curves

The script fits a phonon DOS curve with 2 component curves. One of the components can be convoluted with a damped harmonic oscillator function. The relative ratio between the two components 'a' and the quality factor 'Q' are fit parameters.

fit.m is the main script that performs the least square minimisation routine and calls the function (dosfit) which convolutes the phonon DOS curve (given by the user as component 1) with damped harmonic oscillator function. The input files are expected to have a step size of 0.4 meV.

```
------------------------------fit.m-----------------------------------
$\%######################Initialization###################$
global dos_2ML_RT
global monolayerdos
global bulkdos
global fitrange

$\%########################Data import#####################$
temp=importdata('<name of the file containing phonon DOS that has to be
     fitted>');
dos_2ML_RT(:,1)=temp(2:size(temp,1),1);
dos_2ML_RT(:,2)=temp(2:size(temp,1),2);
xdata=dos_2ML_RT(:,1);

temp=importdata('<name of the file containing component phonon DOS 1>');
monolayerdos(:,2)=temp(2:size(temp,1),2);
monolayerdos(:,1)=xdata;

temp=importdata('<name of the file containing component phonon DOS 2>');
bulkdos(:,2)=temp(2:size(temp,1),2);
```

```
bulkdos(:,1)=xdata;


$\%#######################Parameters#######################$
fitrange=[5,65]; \%index of xdata to fit
param0=[10,0.1]; \%initial [Q,a]
lb=[1,0.0001];      \%lowerbounds of Q,a
ub=[80,0.0001];    \%upperbounds of Q,a


$\%#######################Fitting#######################$
fun=@(param)abs(dos_2ML_RT(fitrange(1):fitrange(2),2)
-dosfiter([param(1),param(2)]));
\% function to minimize
options=optimoptions('lsqnonlin','OptimalityTolerance',1e-15,
'MaxIterations',10000,'FunctionTolerance',1e-12) \% Optimisation parameters
param=lsqnonlin(fun,param0,lb,ub,options)
res=sum(abs(dos_2ML_RT(fitrange(1):fitrange(2),2)-dosfiter([param(1),
param(2)])))  \% minimum value

dosfiter is a function that convolutes the component one with a specified
Q factor (given separately)


$\%#######################plotting#################################$

figure
fit=dosfit([param(1),param(2)]);
plot(xdata,dos_2ML_RT(:,2),'ko',xdata,fit,'r',xdata,param(2)
.*monolayerdos(:,2),'--',xdata,(fit-(param(2).*monolayerdos(:,2))),
'--','LineWidth',2);
xlim([0 30])
legend('2ML=expt LT ML + expt Bulk LT','Fit','ML contribution','bulk')
annotation('textbox',[0.750 0.62 0.7 0.1],'String',{'ML fraction ='
 num2str(param(2))},'FitBoxToText','on','linestyle','none')
annotation('textbox',[0.750 0.50 0.7 0.1],'String',{'Q Bulk      ='
 num2str(param(1))},'FitBoxToText','on','linestyle','none')
annotation('textbox',[0.750 0.38 0.7 0.1],'String',{'Residue     ='
 num2str(res)},'FitBoxToText','on','linestyle','none')
grid on;
```

```
line([xdata(fitrange(2)) xdata(fitrange(2))], get(gca, 'ylim'));
line([xdata(fitrange(1)) xdata(fitrange(1))], get(gca, 'ylim'));
title(' RT 2ML DOS FIT with LT 1ML and LT Bulk DOS- measured bkd')


---------------sub routine "dosfitter.m" used by fit.m ----------------


function [output] = dosfiter(ini)\%use lsqnonfunction
global dos_2ML_RT
global monolayerdos
global bulkdos
global fitrange

$\%initialize Q, dummy counters$
i=1;j=1;Q=ini(1,1);

$\%DHO function $
counter=size(bulkdos,1);
counter=counter+1;
while i<counter(1,1)
    j=1;
    while j<counter(1,1)
        h(j,i)=((1/(pi*Q*bulkdos(j,1)))*1/((bulkdos(j,1)./bulkdos(i,1)
         - bulkdos(i,1)./bulkdos(j,1)).^2 + 1/Q.^2));
        j=j+1;
    end
    k(i)=sum(h(:,i))*0.435;
    h(:,i)=h(:,i)./k(i);
    i=i+1;
end
i=1;sum1=zeros(counter(1,1)-1,1);
\%integration
while i<(counter(1,1))
    j=1;
    while j<counter(1,1)
        sum1(i,1)=h(j,i).*bulkdos(j,2).*0.4+sum1(i);
        j=j+1;
    end
    i=i+1;
```

```
end
$\normalisation$

area=trapz(bulkdos(:,1),sum1);
cbulkdos=sum1(:,1)./area;

output=(1-ini(1,2)).*cbulkdos(:,1)+ini(1,2).*monolayerdos(:,2);
output=output(fitrange(1):fitrange(2));
end
```

List of publications

Publications related to the thesis:

1. Lattice dynamics of EuO: An evidence for gaint spin-phonon coupling
   R. Pradip, P. Piekarz, A. Bosak, D. G Merkel, O. Waller, A. Seiler, A. I. Chumakov, R. Rüffer, A. M. Oleś, K. Parlinski, M. Krisch, T. Baumbach, and S. Stankov
   Physics Review Letters **116**, 185501(2016)

2. Lattice dynamics of paramagnetic EuO ultrathin films and surfaces
   R. Pradip, P. Piekarz, D. G. Merkel, O. Waller, A. Seiler, A. I. Chumakov, R. Rüffer, K. Parlinski, T. Baumbach, and S. Stankov
   In preparation

3. Lattice dynamics of Eu_2O_3
   R. Pradip, P. Piekarz, D. G. Merkel, O. Waller, A. Seiler, A. I. Chumakov, R. Rüffer, K. Parlinski, T. Baumbach, and S. Stankov
   In preparation

Other publications:

1. Anomalous Lattice Dynamics of $EuSi_2$ Nanoislands: Role of Interfaces Unveiled
   A. Seiler, P. Piekarz, S. Ibrahimkutty, D. G. Merkel, O. Waller, **R. Pradip**, A. I. Chumakov, R. Rüffer, T. Baumbach, K. Parlinski, M. Fiederle and S. Stankov
   Physics Review Letters (accepted)

2. Thermal stability studies of $DySi_2$ nanowires and nanoislands by *in situ* GISAXS
   A. Seiler, S. Ibrahimkutty, P. Wochner, **R. Pradip**, O. Waller, A. Plech, T. Baumbach, M. Fiederle , and S. Stankov
   Journal of Physical Chemistry C **120**, 7365 (2016)

3. A portable ultrahigh-vacuum system for advanced synchrotron radiation studies of thin films and nanostructures: $EuSi_2$ nano-islands
   S. Ibrahimkutty, A. Seiler, T. Prüßmann, T.Vitova, **R. Pradip**, O. Bauder, P. Wochner, A. Plech, T. Baumbach, and S. Stankov
   Journal of Synchrotron Radiation **22**, 91 (2015)

4. Growth and structure characterization of $EuSi_2$ films and nanoislands on vicinal Si(001) surface
   A. Seiler, O. Bauder, S. Ibrahimkutty, **R. Pradip**, T. Prüßmann, T. Vitova, M. Fiederle, T. Baumbach, and S. Stankov
   Journal of Crystal Growth **407**, 74 (2014)

Lattice Dynamics of EuO: Evidence for Giant Spin-Phonon Coupling

R. Pradip,[1,2] P. Piekarz,[3] A. Bosak,[4] D. G. Merkel,[4,*] O. Waller,[1,2] A. Seiler,[1,2] A. I. Chumakov,[4] R. Rüffer,[4] A. M. Oleś,[5,6] K. Parlinski,[3] M. Krisch,[4] T. Baumbach,[1,2,7] and S. Stankov[2,1,†]

[1]*Laboratory for Applications of Synchrotron Radiation, Karlsruhe Institute of Technology, D-76131 Karlsruhe, Germany*
[2]*Institute for Photon Science and Synchrotron Radiation, Karlsruhe Institute of Technology, D-76344 Eggenstein-Leopoldshafen, Germany*
[3]*Institute of Nuclear Physics, Polish Academy of Sciences, PL-31342 Kraków, Poland*
[4]*ESRF–The European Synchrotron, F-38000 Grenoble, France*
[5]*Max-Planck-Institut für Festkörperforschung, D-70569 Stuttgart, Germany*
[6]*Marian Smoluchowski Institute of Physics, Jagiellonian University, PL-30348 Kraków, Poland*
[7]*ANKA, Karlsruhe Institute of Technology, D-76344 Eggenstein-Leopoldshafen, Germany*

(Received 30 November 2015; published 2 May 2016)

Comprehensive studies of lattice dynamics in the ferromagnetic semiconductor EuO have been performed by a combination of inelastic x-ray scattering, nuclear inelastic scattering, and *ab initio* calculations. A remarkably large broadening of the transverse acoustic phonons was discovered at temperatures above and below the Curie temperature $T_C = 69$ K. This result indicates a surprisingly strong momentum-dependent spin-phonon coupling induced by the spin dynamics in EuO.

DOI: 10.1103/PhysRevLett.116.185501

Discovered in the early 1960s as the first rare-earth semiconducting oxide, EuO has remained an archetypal system for a Heisenberg ferromagnet (Curie temperature $T_C = 69$ K) until now. Initially known for its giant magneto-optic Kerr [1] and Faraday [2] effects, this fascinating oxide revealed a rich variety of other physical phenomena, such as metal-insulator transition with colossal magnetoresistance under doping [3], strain-induced manipulation of the T_C [4], and anomalous Hall effect [5]. Presently, it is one of the favored candidates for applications as a spin filter in future spintronic devices due to the large exchange splitting of its conduction band [6]. Indeed, EuO-based tunnel junctions have already demonstrated very high spin polarization efficiency [7] that, along with the recent integration on Si [8–10], classifies EuO as a potential workhorse in the Si-based spintronics.

It is surprising that the lattice dynamics of EuO, which is of fundamental importance for the proposed applications, is much less known, with only few early Raman studies [11,12]. Spin waves (magnons) in EuO and their linewidths ($\propto$ lifetime^{-1}) have been investigated in a broad temperature and momentum range [13–17]. Inelastic neutron scattering (INS) studies reported an anomaly in the spin-wave linewidth estimated from dynamical scaling arguments at T_C [15] and at larger wave vectors [16]. The spin-wave energy and linewidth dependence on the wave vector and temperature were studied within several theories [18–20], but the origin of the experimental linewidths and shapes remained to a certain extent unexplained. Other physical phenomena related to the lattice dynamics, such as a reduction of both the sound velocity [21] and thermal conductivity [22] at T_C, have been observed and attributed to spin-phonon coupling. Nevertheless, a direct experimental evidence for this coupling and its magnitude is still missing.

In this Letter we report the lattice dynamics study of EuO across its ferromagnetic transition employing modern synchrotron x-ray scattering techniques and first-principles calculations. We observed a large broadening of the transverse acoustic (TA) phonon branch along the Γ-X direction and a weak broadening of the longitudinal acoustic (LA) branch along the Γ-K-X direction slightly above and well below the Curie temperature. The obtained results uncover a remarkably strong and anisotropic spin-phonon interaction in EuO.

A 100 nm thick single crystalline EuO(001) film was grown on epipolished yttria stabilized zirconia YSZ(001) by reactive molecular beam epitaxy. Details on the sample growth and characterization are given in the Supplemental Material [23], see also Refs. [24–28]. Temperature-dependent momentum resolved spectra of inelastic x-ray scattering (IXS) were collected in grazing incidence geometry along Γ-X and Γ-K-X directions of the Brillouin zone at the beamline ID28 of the European Synchrotron (ESRF) using photons with an incident energy of 17.794 keV and an energy resolution of 3 meV [29]. The sample was measured under vacuum ($\approx 10^{-6}$ mbar) in a helium flow cryostat equipped with kapton foil windows for the x-ray beam. The phonon energies in Fig. 1 and linewidths were precisely determined by employing a model function consisting of a superposition of damped harmonic oscillator functions, convoluted with the predetermined resolution function, and numerically fitted to the IXS spectra [23]. Additionally, a temperature-dependent nuclear inelastic scattering (NIS) experiment on the EuO(001) film was performed at the Nuclear Resonance Beamline ID18 [30] of

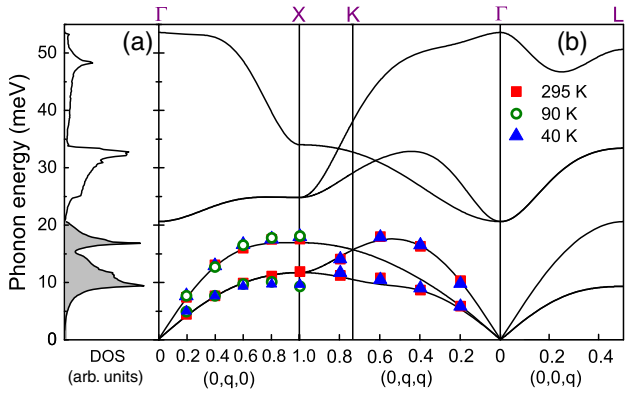

FIG. 1. (a) The *ab initio* calculated phonon DOS of EuO. The shaded area corresponds to the Eu-partial DOS. (b) Phonon dispersion relations from *ab initio* calculations (lines) and IXS experiments (points) at 295, 90, and 40 K.

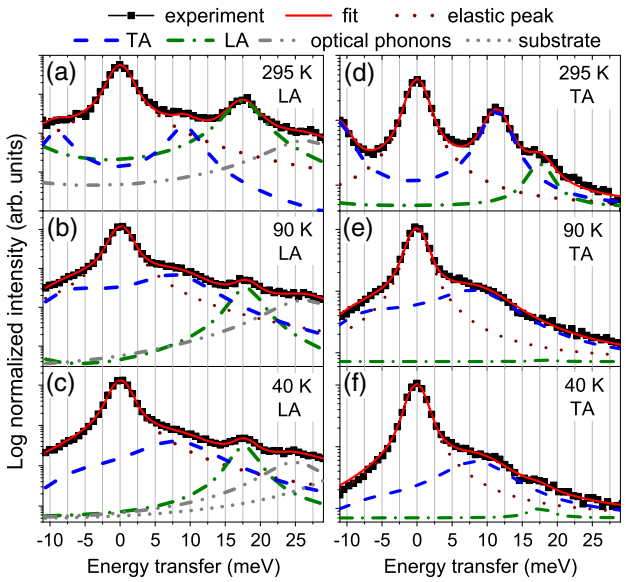

FIG. 2. Selected energy IXS scans for $q = 0.8$ along the Γ-X direction at the indicated temperatures. In (a)–(c) both the LA and TA phonons were excited, while in (d)–(f) mostly the TA excitations were probed. The complete data set and a detailed description of the fitting procedure are given in the Supplemental Material [23].

the ESRF to obtain the Eu-partial phonon DOS. The incident photon energy was tuned in the vicinity of the resonant transition energy (21.54 keV) of the ^{151}Eu nuclei with an energy resolution of 1.1 meV [31]. The sample was measured under vacuum ($\approx 10^{-6}$ mbar) in a helium flow cryostat equipped with kapton foil windows for the x-ray beam. The grazing incidence NIS data were collected with the wave vector of the incident photons parallel to the [010] direction of the EuO(001) film, corresponding to the Γ-X direction in the Brillouin zone. A standard procedure [32] was used to obtain the Eu-partial phonon DOS from the NIS spectra measured at several temperatures in the range 30–295 K.

Density functional theory was used to determine the lattice dynamics of EuO. The electronic structure was optimized within the projector augmented-wave method [33] and the generalized-gradient approximation (GGA) [34] implemented in the VASP software [35]. We have included a strong local Hubbard interaction ($U_f = 8.3$ eV, $U_p = 4.6$ eV) and Hund's exchange ($J_f = 0.77$ eV, $J_p = 1.2$ eV) [36] for the Eu($4f$) and O($2p$) states using the GGA + U method [37]. The optimized lattice parameter $a = 5.16$ Å corresponds well to the measured value 5.14 Å, and the calculated $4f$-$5d$ band gap of 1.05 eV agrees with the experimental value of 1.12 eV [38]. The phonon density of states and phonon dispersions (Fig. 1) were calculated using the direct method [39]. The Hellmann-Feynman forces were obtained by displacing nonequivalent atoms from their equilibrium positions to determine the force constants and dynamical matrices. Phonon energies and polarization vectors at a given wave vector follow from the exact diagonalization of the dynamical matrix.

Figure 1(b) reveals an excellent agreement between the experimental points obtained at the indicated temperatures and the *ab initio* calculated phonon dispersion relations. Compared to Eu metal [40], the energies of acoustic branches are increased by a few meV due to larger force constants in EuO. The weak scattering cross section of the oxygen atoms deterred us from tracing the optical branches at higher energies. The phonon energies remain fairly temperature independent, except an evident softening of the TA mode at low temperatures near the X point along the Γ-X direction ($\Delta E \approx 21\%$) that may arise from spin-phonon coupling.

Selected energy scans of IXS measured at a momentum transfer $q = 0.8$ along the Γ-X direction and at the indicated temperatures are shown in Fig. 2. Since the IXS intensity depends on the scattering vector and polarization of phonons, the scans plotted in Figs. 2(a)–2(c) and Figs. 2(d)–2(f) were measured in two different scattering geometries favoring the excitation of the LA and TA modes, respectively (for more details, see Supplemental Material [23]). At room temperature both the LA and TA peaks are well pronounced, exhibiting rather narrow linewidths. Reducing the temperature to 90 K leads to a drastic broadening of the TA mode, Figs. 2(d) and 2(e), while the width of the LA peak remains unaffected; see Figs. 2(a) and 2(b). The same phenomenon is observed for $T = 40$ K that is well below T_C; see Figs. 2(c) and 2(f).

The full widths at half maximum (FWHMs) derived from the fit to the experimental data [23] are plotted as functions of momentum transfer for the TA and LA branches along the Γ-X and Γ-K-X directions in Figs. 3(a) and 3(b) and Figs. 3(c) and 3(d), respectively. The FWHMs of the TA and LA modes along all the measured directions at room temperature remain weakly q

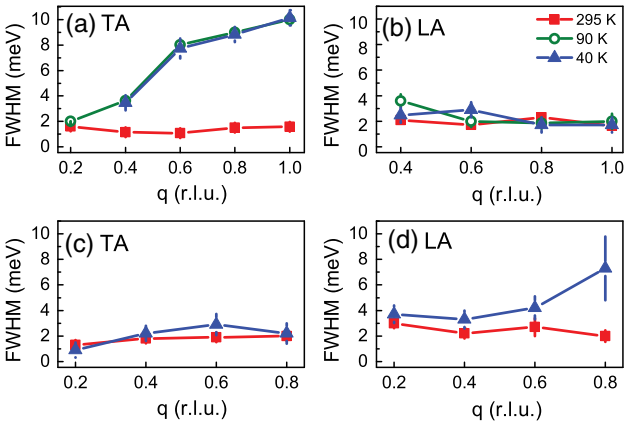

FIG. 3. (a),(b) FWHMs as a function of momentum transfer for the TA and LA branches along the Γ-X direction at 295, 90, and 40 K. (c),(d) FWHMs for the TA and LA branches along Γ-K-X direction at 295 and 40 K.

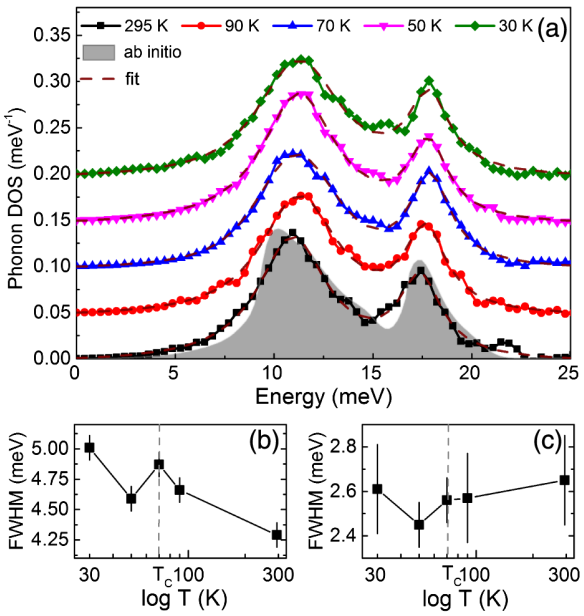

FIG. 4. (a) The Eu-partial phonon DOS in EuO obtained from the NIS experiment at the indicated temperatures. The spectra are up-shifted by 0.05 meV^{-1} for clarity. The *ab initio* calculated Eu-partial phonon DOS, convoluted with the instrumental resolution function, is depicted as shaded area. The dashed line stands for the fit of the experimental data with a combination of two Voigt profiles. The FWHM for increasing temperature for phonons at (b) 11 meV and (c) 17 meV. The solid lines are guides to the eye.

dependent throughout the entire Brillouin zone. We emphasize the remarkable q-dependent broadening of the TA modes along the Γ-X direction at $T = 90$ K and below; see Fig. 3(a). In fact, the phonon linewidth at the zone boundary increases by a factor of 5 from that measured at room temperature. Additionally, a weakly q-dependent broadening of the LA phonon modes along Γ-K-X is observed; see Fig. 3(d). In contrast to the Γ-X direction, the increase of the FWHMs for $q \leq 0.6$ is only a factor of 1.6 with respect to that measured at room temperature, with a clear tendency to increase towards the X point. At the same time, the widths of the LA and TA branches along Γ-X and Γ-K-X, respectively, remain temperature independent within the error bars; see Figs. 3(b) and 3(c).

Figure 4(a) shows the Eu-partial phonon DOS obtained at the indicated temperatures and reveals a good agreement with the *ab initio* calculated DOS convoluted with the instrumental function. A noticeable broadening of the TA peak at 11 meV with decreasing temperature is clearly visible. In order to estimate the width of the peaks at 11 and 17 meV, the DOS curves were approximated [dashed line in Fig. 4(a)] by a combination of two Voigt profiles. Figure 4(b) reveals an increase of the FWHMs of the TA modes with decreasing temperature, reaching about 17% at 30 K. The width of the second peak, which stems from the LA modes, however, is independent of temperature; see Fig. 4(c). These observations are in a qualitative agreement with the results from the IXS experiment. However, a direct quantitative comparison of the phonon linewidths obtained by IXS and NIS will be erroneous since the latter gives the momentum averaged and combined contributions from the LA and TA branches.

The observed phenomenon by both IXS and NIS experimental methods is surprising and in contrast to the usual decrease of phonon linewidths with decreasing T [41]. It demonstrates that a new type of coupling is activated by the spin dynamics. The inverse temperature dependence of the phonon broadening suggests that it is induced neither by scattering from defects nor by phonon-phonon interactions. In order to exclude anharmonic effects, the phonon energies were calculated assuming various atomic displacements, similarly to the previous studies on magnetite [42] (see also Supplemental Material [23]). The calculations show a negligible change in the phonon dispersions. The YSZ substrate with its matching crystal structure and lattice constant provides a strain-free template for the epitaxial growth of EuO films [23]. Consequently, anharmonicity and substrate-induced epitaxial strain are ruled out as the origin of the observed enormous increase of the TA phonon linewidths with decreasing T.

INS investigations of the spin dynamics in EuO have undoubtedly proven the presence of finite spin correlations above T_C up to 115 K [16,17,43]. Well-defined but heavily damped spin waves above T_C at the zone boundaries, mediated by exchange between nearest (NN) and next-nearest neighbor (NNN) Eu ions, have been experimentally observed [16,17] and theoretically confirmed [20], similar to Fe [44], Ni [45], and double perovskites [46]. The measured spin waves in EuO showed also an increasing linewidth towards the zone boundaries and were not accurately described most likely because their scattering from phonons was not considered. Following the Raman scattering experiments that reported a coupling of optical

phonons to spin waves [11,12], we attribute the observed increase of phonon linewidths towards the zone boundary at $T > T_C$ to an enhanced scattering of phonons by short-range spin excitations. Figure 3 reveals that phonon broadening is observed for the TA and LA modes along the Γ-X and Γ-K-X directions, in the ferromagnetic sample at 40 K. We recall the anomalous reduction of the sound velocity below T_C, which is believed to originate from strong coupling of spin fluctuations to acoustic phonons [21]. Thus, also for $T < T_C$, the spin-phonon coupling can be regarded as the mechanism behind the reduced phonon lifetimes obtained in our experiments.

A theoretical study of magnon-phonon coupling in a Heisenberg ferromagnet unveiled that the force constants acting between the NN and NNN play a decisive role in the spin-phonon coupling process [28]. Namely, for the TA modes the coupling is stronger towards the X point along Γ-X, while the LA modes couple more tightly to spin waves along Γ-K-X, provided that the force constants between the NNN are comparable to those acting between the NN. Our *ab initio* calculations indeed revealed that this condition is fulfilled for EuO (for details, see Supplemental Material [23]). In addition, the energies of the TA modes are closer to those of the spin waves (up to 6 meV [13]) compared to the LA modes. Even though the energies do not match exactly, they span a comparable range such that the momentum and energy conservation of the spin-phonon coupling process could be fulfilled. This explains the linewidth broadening observed in the TA modes along the Γ-X direction [Fig. 3(a)]. Contrary to the TA modes, the LA phonons show a pronounced broadening along the Γ-K-X direction [Fig. 3(d)]. We attribute this observation to the fact that these LA modes modulate the shortest Eu-Eu distance, thus affecting the magnetic exchange interaction between the localized $4f$ electrons. This effect is particularly strong at the zone boundary, where the NN atoms vibrate with opposite phases, which explains the increase of the phonon widths towards the X point.

Studies performed within the s-f model [47] revealed a large contribution of spin-phonon coupling to the phonon damping below and above T_C [48]. In order to estimate the spin-phonon coupling constant α, we use $\Gamma \approx \hbar\omega(zJ'^2/K)\chi_s''(\hbar\omega)$ [41], where Γ is the phonon width induced by spin fluctuations, $\hbar\omega$ is the phonon energy, z is the coordination number, J is the exchange coupling constant, K is the normalized force constant, and $J' = \alpha J/\text{Å}$ is the change of the exchange coupling constant J due to atomic displacement. We use $\chi_s''(\hbar\omega) \approx \hbar\omega(S/zJ)^2$ valid for a paramagnet. With $\Gamma \approx 8$ meV, $S = 7/2$, $z = 6$, $\hbar\omega = 10$ meV, and $K = 2.5$ eV/Å^2, we obtain $\alpha \approx 10$. This value is among the largest spin-phonon coupling constants observed [49,50]. Considering that the spin-phonon coupling in EuO arises from the Heisenberg and s-f exchange interactions and assuming a value of $\alpha_H \approx 4$ for the Heisenberg term [51], we deduce that $\alpha_{s\text{-}f} \approx 6$.

Furthermore, we have found an overall very good agreement in the temperature dependence of the Eu-projected vibrational entropy S_{vib} and lattice specific heat C_V of EuO, derived from the NIS experiment and the *ab initio* theory; see Supplemental Material [23]. However, we have detected neither an anomalous increase nor a critical behavior of the C_V at T_C. This is in agreement with the weak critical phonon scattering deduced from the thermal conductivity [52] and implies that the anomaly observed by calorimetric experiments [53,54] is not connected with the lattice excitations, but it arises from the magnetic contribution to the specific heat [55]. The normalized mean force constant K remains unchanged within the error bars for the entire temperature range that is consistent with the weak anharmonicity in EuO.

In conclusion, we have determined the lattice dynamics of EuO in a broad temperature range across the T_C by IXS, NIS, and first-principles calculations. The experiments unambiguously reveal a remarkable broadening of the phonons at low temperatures, especially pronounced for the TA modes along the Γ-X direction. This is unexpected and implies a surprisingly strong spin-phonon coupling activated by spin fluctuations, which influences the electronic states and the lattice dynamics. The large spin-phonon coupling reported here seems to be the missing component for the accurate interpretation of the spin-wave linewidth dependence on temperature and momentum obtained by INS experiments [15,16,20]. Moreover, such noticeable anisotropic coupling is of relevance for the proposed application of EuO in spintronics. Our results show that the magnitude of the spin-phonon coupling in EuO is smaller along the Γ-K-X than along the Γ-X direction, implying that the choice of crystal orientation could be crucial for reducing the undesired spin flips.

We thank Giniyat Khaliullin and Paweł T. Jochym for valuable discussions. We are grateful to B. Krause, A. Weißhardt, and H. H. Gräfe for the support in the UHV-Analysis Lab. We acknowledge ESRF–The European Synchrotron for provision of synchrotron radiation facilities, the Materials Preparation Center at Ames Laboratory, which is supported by the U.S. DOE Basic Energy Sciences, for providing the Eu source material, and the Excellence Initiative for the financial support of the UHV-Analysis Lab via the project KIT-Nanolab@ANKA. S. S. acknowledges the financial support by the Initiative and Networking funds of the President of the Helmholtz Association and the Karlsruhe Institute of Technology (KIT) for the Helmholtz-University Young Investigators Group "Interplay between structure and dynamics in epitaxial rare earth nanostructures" Contract No. VH-NG-625. P. P. and A. M. O. kindly acknowledge support by Narodowe Centrum Nauki (NCN) under Projects No. 2011/01/M/ST3/00738 and No. 2012/04/A/ST3/00331.

*On leave from Institute for Particle and Nuclear Physics, Wigner Research Centre for Physics, Hungarian Academy of Sciences, H-1525 Budapest, Hungary.
†Corresponding author.
Svetoslav.Stankov@kit.edu

[1] J. H. Greiner and G. J. Fan, Appl. Phys. Lett. **9**, 27 (1966).
[2] K. Y. Ahn, J. Appl. Phys. **41**, 1260 (1970).
[3] Y. Shapira, S. Foner, and R. Aggarwal, Phys. Rev. B **8**, 2316 (1973).
[4] A. Melville, T. Mairoser, A. Schmehl, T. Birol, T. Heeg, B. Holländer, J. Schubert, C. J. Fennie, and D. G. Schlom, Appl. Phys. Lett. **102**, 062404 (2013).
[5] T. Yamasaki, K. Ueno, A. Tsukazaki, T. Fukumura, and M. Kawasaki, Appl. Phys. Lett. **98**, 082116 (2011).
[6] P. G. Steeneken, L. H. Tjeng, I. Elfimov, G. A. Sawatzky, G. Ghiringhelli, N. B. Brookes, and D. J. Huang, Phys. Rev. Lett. **88**, 047201 (2002).
[7] T. S. Santos, J. S. Moodera, K. V. Raman, E. Negusse, J. Holroyd, J. Dvorak, M. Liberati, Y. U. Idzerda, and E. Arenholz, Phys. Rev. Lett. **101**, 147201 (2008).
[8] A. Schmehl *et al.*, Nat. Mater. **6**, 882 (2007).
[9] R. P. Panguluri, T. S. Santos, E. Negusse, J. Dvorak, Y. Idzerda, J. S. Moodera, and B. Nadgorny, Phys. Rev. B **78**, 125307 (2008).
[10] C. Caspers, M. Müller, A. X. Gray, A. M. Kaiser, A. Gloskovskii, C. S. Fadley, W. Drube, and C. M. Schneider, Phys. Rev. B **84**, 205217 (2011).
[11] J. C. Tsang, M. S. Dresselhaus, R. L. Aggarwal, and T. B. Reed, Phys. Rev. B **9**, 984 (1974).
[12] P. Grünberg, G. Güntherodt, A. Frey, and W. Kress, Physica B (Amsterdam) **89**, 225 (1977); G. Güntherodt, R. Merlin, and W. Grünberg, Phys. Rev. B **20**, 2834 (1979); R. Zeyher and W. Kress, Phys. Rev. B **20**, 2850 (1979).
[13] L. Passell, O. W. Dietrich, and J. Als-Nielsen, Phys. Rev. B **14**, 4897 (1976).
[14] J. Als-Nielsen, O. W. Dietrich, and L. Passell, Phys. Rev. B **14**, 4908 (1976).
[15] O. W. Dietrich, J. Als-Nielsen, and L. Passell, Phys. Rev. B **14**, 4923 (1976).
[16] H. A. Mook, Phys. Rev. Lett. **46**, 508 (1981).
[17] P. Böni and G. Shirane, Phys. Rev. B **33**, 3012 (1986).
[18] V. Vaks, A. Larkin, and S. Pikin, Sov. Phys. JETP **26**, 188 (1968).
[19] R. Raghavan and D. L. Huber, Phys. Rev. B **14**, 1185 (1976).
[20] A. P. Young and B. S. Shastry, J. Phys. C **15**, 4547 (1982).
[21] B. Lüthi and R. J. Pollina, Phys. Rev. Lett. **22**, 717 (1969).
[22] R. G. Morris and J. L. Cason, Helv. Phys. Acta **41**, 1045 (1968).
[23] See Supplemental Material at http://link.aps.org/supplemental/10.1103/PhysRevLett.116.185501, for sample preparation and characterization, evaluation of inelastic x-ray scattering data, *ab initio* calculations and thermoelastic properties.
[24] R. Sutarto *et al.*, Phys. Rev. B **79**, 205318 (2009).
[25] R. W. Ulbricht, A. Schmehl, T. Heeg, J. Schubert, and D. G. Schlom, Appl. Phys. Lett. **93**, 102105 (2008).
[26] M. A. Andreeva, Hyperfine Interact. **185**, 17 (2008).
[27] H. H. Wickman, J. Appl. Phys. **39**, 1248 (1968).
[28] T. M. Cheng and L. Li, J. Magn. Magn. Mater. **320**, 1 (2008).
[29] M. Krisch and F. Sette, *Light Scattering in Solid IX*, edited by M. Cardona and R. Merlin, Topics in Applied Physics Vol. 108 (Springer, Berlin, 2007), pp. 317–370.
[30] R. Rüffer and A. I. Chumakov, Hyperfine Interact. **97–98**, 589 (1996).
[31] O. Leupold, J. Pollmann, E. Gerdau, H. D. Rüter, G. Faigel, M. Tegze, G. Bortel, R. Rüffer, A. I. Chumakov, and A. Q. R. Baron, Europhys. Lett. **35**, 671 (1996).
[32] V. Kohn and A. I Chumakov, Hyperfine Interact. **125**, 205 (2000).
[33] P. E. Blöchl, Phys. Rev. B **50**, 17953 (1994).
[34] J. P. Perdew, K. Burke, and M. Ernzerhof, Phys. Rev. Lett. **77**, 3865 (1996).
[35] G. Kresse and J. Furthmüller, Comput. Mater. Sci. **6**, 15 (1996).
[36] N. J. C. Ingle and I. S. Elfimov, Phys. Rev. B **77**, 121202 (2008).
[37] V. I. Anisimov, J. Zaanen, and O. K. Andersen, Phys. Rev. B **44**, 943 (1991).
[38] G. Busch, G. Güntherodt, and P. Wachter, J. Phys. (Paris), Colloq. **32**, 928 (1971).
[39] K. Parlinski, Z-. Q. Li, and Y. Kawazoe, Phys. Rev. Lett. **78**, 4063 (1997).
[40] S. Stankov, P. Piekarz, A. M. Oleś, K. Parlinski, and R. Rüffer, Phys. Rev. B **78**, 180301 (2008).
[41] C. Ulrich, G. Khaliullin, M. Guennou, H. Roth, T. Lorenz, and B. Keimer, Phys. Rev. Lett. **115**, 156403 (2015).
[42] M. Hoesch, P. Piekarz, A. Bosak, M. Le Tacon, M. Krisch, A. Kozłowski, A. M. Oleś, and K. Parlinski, Phys. Rev. Lett. **110**, 207204 (2013).
[43] R. Chaudhury and B. S. Shastry, Phys. Rev. B **37**, 5216 (1988).
[44] X. Tao, D. P. Landau, T. C. Schulthess, and G. M. Stocks, Phys. Rev. Lett. **95**, 087207 (2005).
[45] V. Antropov, Phys. Rev. B **72**, 140406(R) (2005).
[46] S. M. Zhou, Y. Q. Guo, J. Y. Zhao, S. Y. Zhao, and L. Shi, Appl. Phys. Lett. **96**, 262507 (2010).
[47] W. Nolting and A. M. Oleś, Phys. Rev. B **22**, 6184 (1980); **23**, 4122 (1981).
[48] J. M. Wesselinowa and A. T. Apostolov, J. Phys. Condens. Matter **5**, 3555 (1993).
[49] B. Normand, H. Kohno, and H. Fukuyama, Phys. Rev. B **53**, 856 (1996).
[50] R. Werner, C. Gros, and M. Braden, Phys. Rev. B **59**, 14356 (1999).
[51] W. Baltensperger and J. S. Helman, Helv. Phys. Acta **41**, 668 (1968).
[52] J. J. Martin and G. S. Dixon, Phys. Status Solidi B **54**, 707 (1972).
[53] A. Kornblit and G. Ahlers, Phys. Rev. B **11**, 2678 (1975).
[54] K. Ahn, A. O. Pecharsky, K. A. Gschneidner, and V. K. Pecharsky, J. Appl. Phys. **97**, 063901 (2005).
[55] B. E. Argyle, N. Miyata, and T. D. Schultz, Phys. Rev. **160**, 413 (1967).

SUPPLEMENTAL MATERIAL

1. Sample preparation and characterization

Europium monoxide crystallizes in a rock salt structure with a lattice parameter 5.14 Å (space group $Fm\bar{3}m$). The europium and oxygen atoms occupy alternating lattice points in all three dimensions. The crystal structure, main crystallographic directions and interatomic distances in EuO are shown in figure S1.

A 100 nm thick single crystalline EuO(001) film was grown on epi-polished yttria stabilised zirconia YSZ(001) by reactive molecular beam epitaxy in a UHV chamber with a base pressure of 3.0×10^{-11} mbar located in the UHV-Analysis laboratory at ANKA, KIT. The growth procedure described by Sutarto et al. [24] was slightly modified by delaying the admission of molecular oxygen (purity $\geq 99.999\%$) until a few monolayers of EuO were formed using the oxygen supplied by the substrate. The substrate temperature was maintained around 673 K to be in the adsorption controlled regime [25]. The fluxes of Eu metal and molecular oxygen were carefully tuned to avoid the formation of other stoichiometries. The sample was *in situ* characterised with reflection high energy electron diffraction (RHEED) and x-ray photoemission spectroscopy (XPS). The sharp streaks visible in the RHEED image, see figure S2(a), confirmed the formation of a flat single crystalline surface, while the XPS study (figure S2(b)) revealed that the Eu atoms exhibit an oxidation state of 2+. After

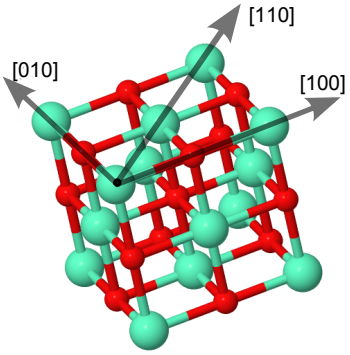

Direction	Atoms	Distance
[010] or Γ-X	Eu-O	2.57 Å
[110] or Γ-K-X	Eu-Eu	3.64 Å

FIG. S1. The crystal structure, main crystallographic directions in EuO. The Eu and O atoms are represented by green/larger and red/smaller spheres, respectively. The inset table shows interatomic distances along the investigated crystallographic directions (Source: adapted from www.icsd.fiz-karlsruhe.de).

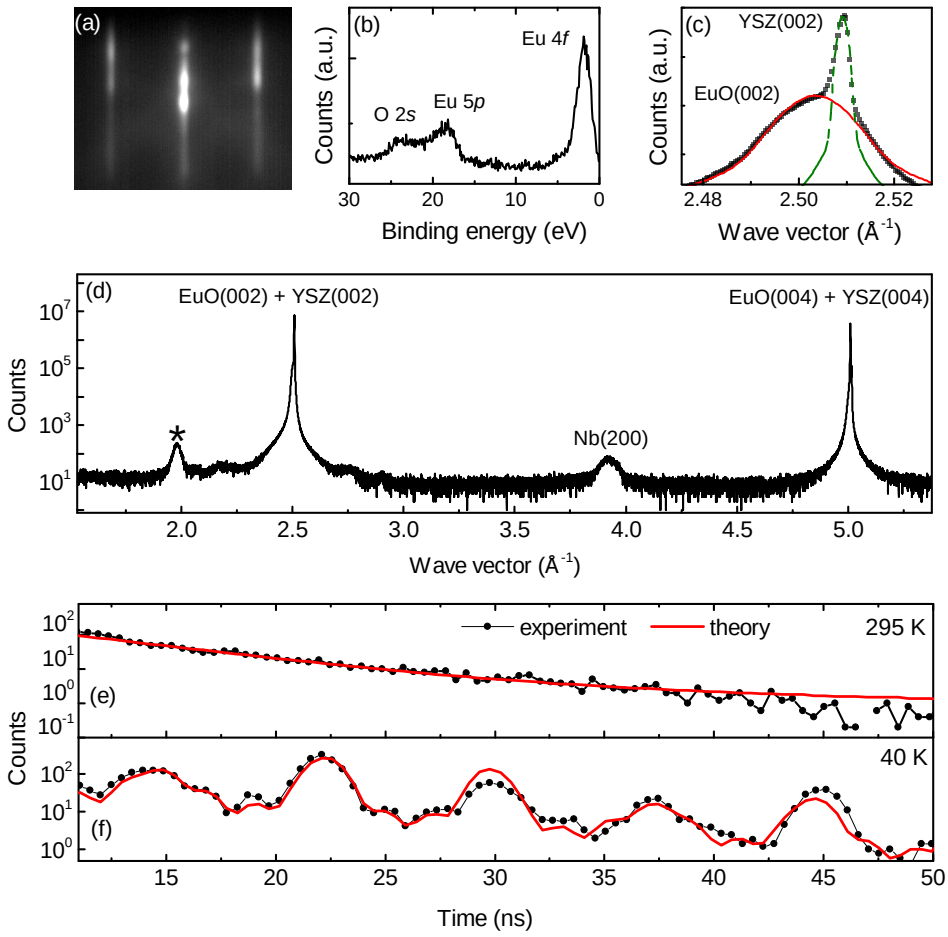

FIG. S2. (color online). (a) RHEED image of the EuO(001) film measured along [110]. (b) Eu $4f$ valence band XPS scan of the EuO film. (c) High resolution XRD scan performed around the EuO(002) peak. The contributions from the EuO film and the YSZ substrate are plotted with dotted/red and dashed/green lines, respectively. (d) XRD scan on the Nb capped 100 nm thick EuO(001) film on YSZ(001). (*) indicates another europium oxide phase (for details see text). (e,f) NFS spectra and the fits (solid/red lines) at the indicated temperatures.

capping with a 10 nm thick Nb layer the film was characterised by *ex situ* x-ray diffraction using Cu K-alpha x-rays. Figure S2(d) confirmed the epitaxial quality and purity of the EuO film. In addition to the EuO(002) and YSZ(002) reflections, peaks originating from the Nb capping layer as well as from another europium oxide phase (*) formed at the film/substrate interface are visible. This ultrathin polycrystalline layer forms at a later stage of the growth due to the excess oxygen supplied by the substrate during the extended deposition time

that is necessary for the formation of the thick EuO film. It constitutes only ≈ 0.3 % of the EuO(002) peak area that makes its contribution to the experimental data negligible. However, this layer of higher oxide practically shields the EuO film from epi-strain propagating from the substrate at low temperatures that could possibly arise from the difference in lattice thermal expansion coefficients of the EuO film and the YSZ substrate. Furthermore, the phase purity and stoichiometry of the EuO film were confirmed by grazing incidence nuclear forward scattering (NFS). Figures S2(e) and (f) show NFS spectra collected at room temperature and at 30 K, respectively. The fits (red/solid lines) were performed using the REFTIM code [26]. The room temperature spectrum confirmed that all Eu atoms in the sample have an equivalent chemical state, while the characteristic quantum beats visible in the NFS spectrum measured at 30 K demonstrated the ferromagnetic order with a net magnetic field of 27.3 T that is characteristic for EuO at this temperature [27].

2. Evaluation of inelastic x-ray scattering data

Momentum resolved spectra of inelastic x-ray scattering (IXS) were collected in grazing incidence geometry along the Γ-X and Γ-K-X directions of the Brillouin zone. The incident grazing angle (0.2°) was larger than the critical angle (0.16°) in order to reduce the contribution of the Nb capping layer to the IXS signal. The direction and size of the momentum transfer (q) were selected by an appropriate choice of the scattering angle and sample orientation in the horizontal scattering plane. The x-ray beam was focused by a combination of two cylindrical mirrors to a spot size of 250×12 μm^2 (horizontal $\times$ vertical, full width at half maximum (FWHM)). The energy of the scattered photons was analyzed by nine Si analyzers mounted in a pseudo Rowland geometry. From the scattered photons, the phonon energies and linewidths (FWHM) were precisely determined by using a model function consisting of the superposition of damped harmonic oscillator profiles (identical results were obtained using Lorentzian profiles). The detailed balance of the model was taken into account by the Bose factor. This function was then convoluted with the experimentally determined resolution function and numerically fitted to the IXS spectra using a χ^2 minimisation routine. A linear background with zero slope was assumed.

The inelastic x-ray scattering spectra were collected in two different grazing incidence sample orientations optimized for excitation of predominantly either the transverse acoustic

(TA) or the longitudinal acoustic (LA) phonon modes in the EuO(001) film. However, due to the unavoidable offset in the q_z direction ($\approx$ 0.1 r.l.u.), a contribution of the LA and TA phonons were observed in both cases. The energy IXS scans for probing the TA excitations along the Γ-X direction, that revealed the largest temperature and momentum dependent effects on FWHMs, are shown in figure S3, while the IXS measurements of the LA modes along the same direction are shown in figure S4. For a precise disentanglement and determination of the positions and linewidths of the phonon excitations at low temperatures, the following strategy was employed. The IXS spectra for LA phonon modes, see figure S4, were first fitted using the procedure described above, keeping all the fit parameters of the excitations unconstrained. The obtained values of the peak position and FWHM of the LA phonon modes were included as fixed parameters in the model for fitting the IXS spectra of the TA modes at corresponding temperature and q values, see figure S3. The final values of the peak positions and the FWHMs are listed in the tables below. An exception from this fitting procedure was made for the transverse phonons at $q = 0.8$ and 1 at 90 K. The FWHMs were limited to 9.0 meV and 10.0 meV, respectively, to obtain the best fit of the phonon excitation, see figure S3(g) and (h). In IXS spectra with energy transfer larger than 25 meV, contributions from the optic phonons in the EuO(001) film and the acoustic phonons in the YSZ(001) substrate are visible, see figure S4(h-l).

Direction	Mode	Momentum transfer
$\Gamma \rightarrow X$	LA	$[4-\zeta, 0, 0.1]$ $(0.2 \leq \zeta \leq 1)$
$\Gamma \rightarrow$ X	TA	$[4, -\zeta, 0.1]$ $(0.2 \leq \zeta \leq 1)$
$\Gamma \rightarrow$ K $\rightarrow$ X	LA & TA	$[4+\zeta, -\zeta, 0.1]$ $(0.2 \leq \zeta \leq 1)$

TABLE S1. A summary of the investigated phonon branches along with the direction, polarization and total momentum transfer.

q	0.4	0.6	0.8	1
T= 295 K	7.62 ± 0.02	9.95 ± 0.02	11.39 ± 0.03	11.89 ± 0.04
T= 90 K	7.68 ± 0.07	9.47 ± 0.07	10.1 ± 0.07	9.34 ± 0.08
T= 40 K	7.62 ± 0.24	9.34 ± 0.16	9.71 ± 0.13	9.63 ± 0.15

TABLE S2. Energies in meV of the TA phonon excitations along the Γ-X direction obtained from the fit to the IXS spectra shown in fig. S3 at the indicated temperatures and momentum transfers.

q	0.4	0.6	0.8	1
T= 295 K	1.15 ± 0.10	1.07 ± 0.10	1.50 ± 0.20	1.57 ± 0.20
T= 90 K	3.62 ± 0.24	8.03 ± 0.28	9.0 (fixed)	10.0 (fixed)
T= 40 K	3.47 ± 0.33	7.73 ± 0.78	8.84 ± 0.48	10.14 ± 0.59

TABLE S3. FWHMs in meV of the TA phonons along the Γ-X direction obtained from the fit to the IXS spectra shown in fig. S3 at the indicated temperatures and momentum transfers.

q		0.4	0.6	0.8	1
T= 295 K	LA	13.14 ± 0.08	16.18 ± 0.09	17.54 ± 0.09	17.62 ± 0.10
T= 90 K	LA	12.73 ± 0.13	16.46 ± 0.11	17.87 ± 0.11	18.07 ± 0.13
	TA	7.52 ± 0.13	8.78 ± 0.12	9.03 ± 0.16	9.26 ± 0.15
T= 40 K	LA	12.96 ± 0.12	16.56 ± 0.09	17.61 ± 0.10	18.01 ± 0.11
	TA	7.48 ± 0.22	8.50 ± 0.50	9.12 ± 0.20	9.06 ± 0.17

TABLE S4. Energies in meV of the LA and TA phonons along the Γ-X direction obtained from the fit to the IXS spectra shown in fig. S4 at the indicated temperatures and momentum transfers.

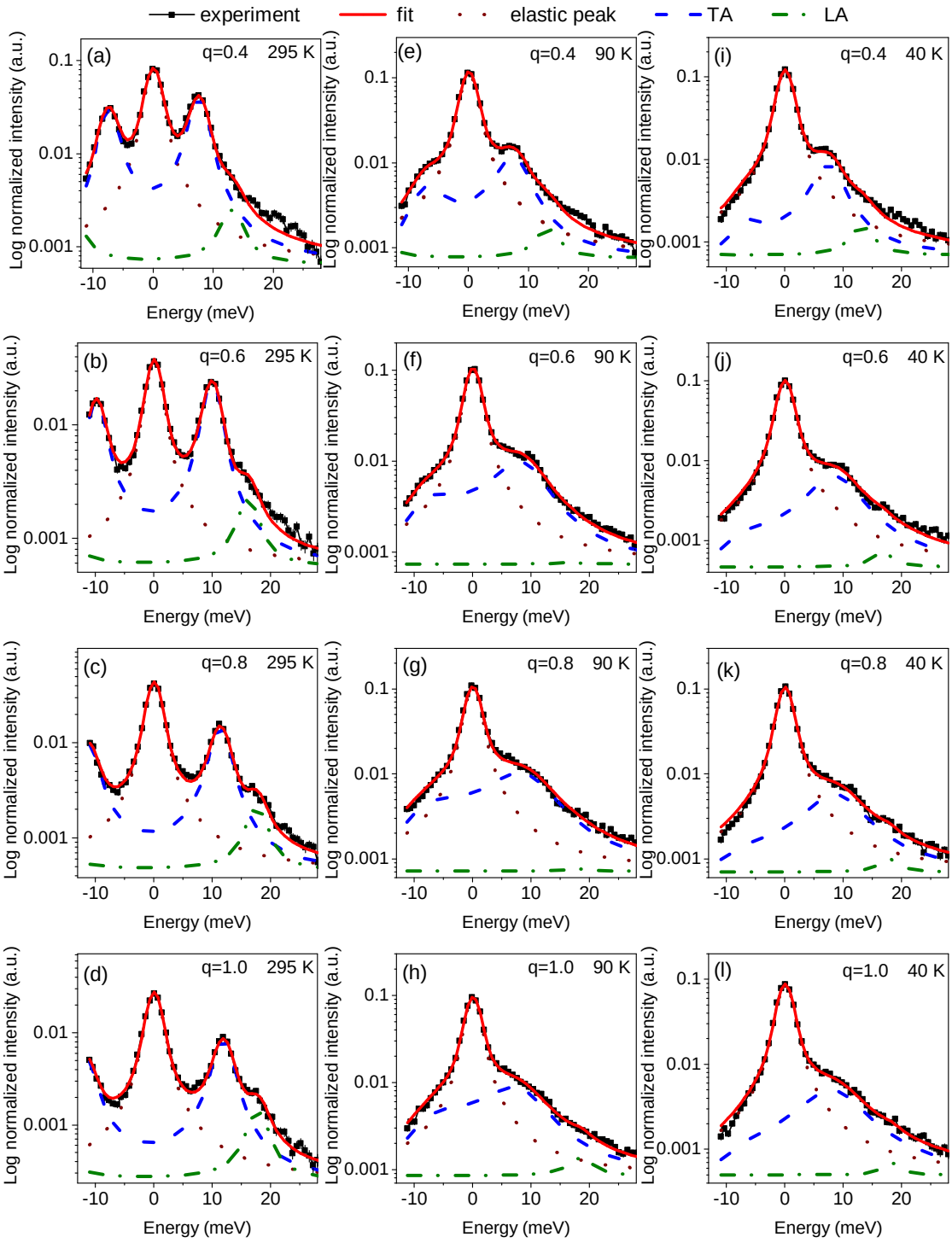

FIG. S3. IXS spectra obtained in a scattering geometry that is optimized for measuring the TA phonon modes with momentum transfer values along Γ-X direction at 295 K (a-d), 90 K (e-h) and 40 K (i-l). The momentum transfer and the temperature are indicated in each plot.

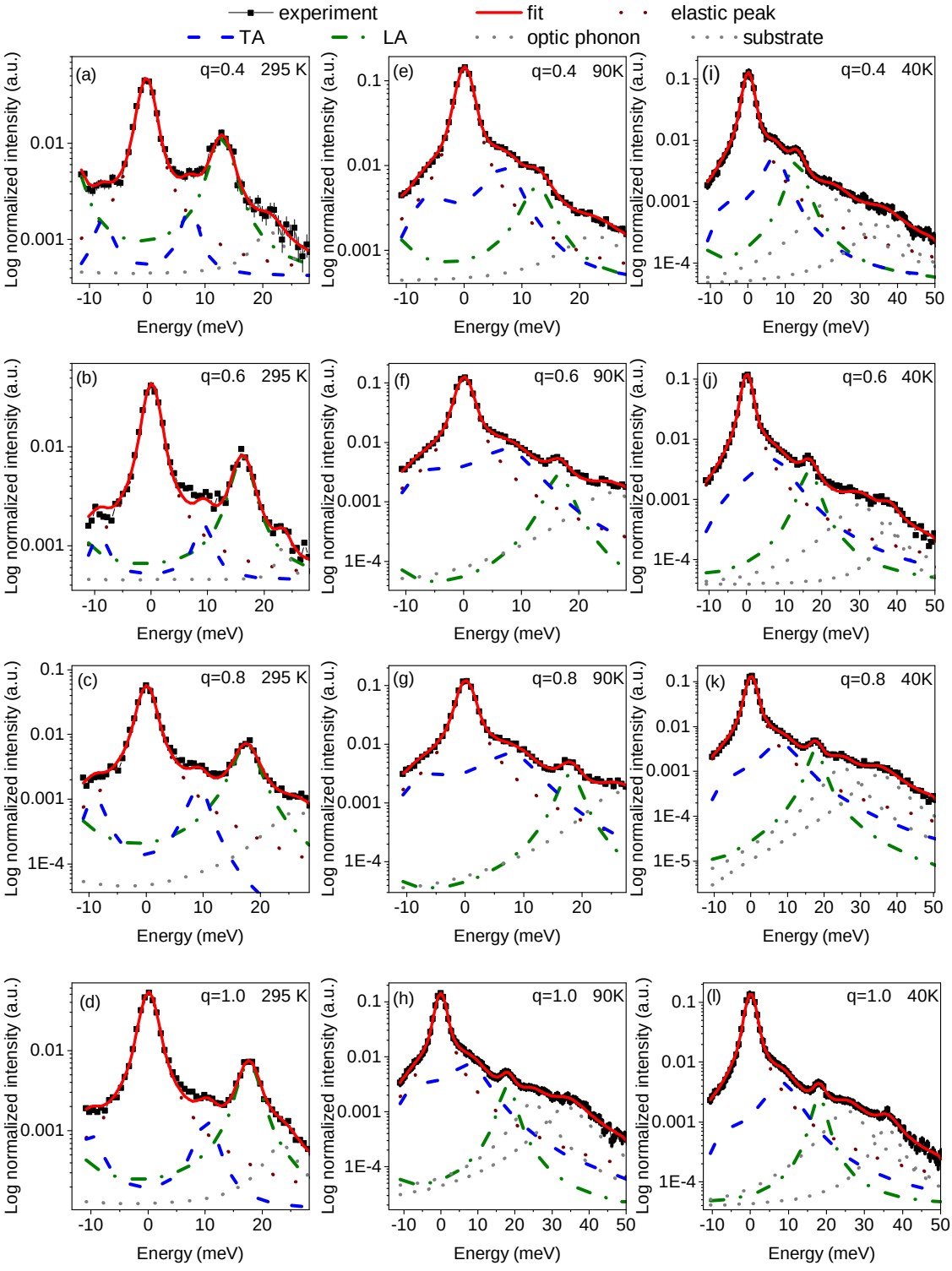

FIG. S4. IXS spectra obtained in a scattering geometry that is optimized for measuring the LA phonon modes with momentum transfer values along Γ-X direction at 295 K (a-d), 90 K (e-h) and 40 K (i-l). The momentum transfer and the temperature are indicated in each plot.

q		0.4	0.6	0.8	1
T= 295 K	LA	1.89 ± 0.25	1.75 ± 0.27	2.26 ± 0.71	1.66 ± 0.27
T= 90 K	LA	3.63 ± 0.52	2.07 ± 0.45	1.86 ± 0.46	2.01 ± 0.59
	TA	5.16 ± 0.22	8.09 ± 0.65	7.80 ± 0.56	8.72 ± 0.53
T= 40 K	LA	2.68 ± 0.45	2.94 ± 0.39	1.72 ± 0.44	1.71 ± 0.54
	TA	4.21 ± 0.79	9.50 ± 0.11	8.34 ± 0.81	7.08 ± 0.67

TABLE S5. FWHMs in meV of the LA and TA phonon excitations along the Γ-X direction obtained from the fit to the IXS spectra shown in fig. S4 at the indicated temperatures and momentum transfers.

3. *Ab initio* calculations

Force constant matrices

The manuscript refers to force constants to explain the phonon polarization and direction dependences of the observed spin-phonon coupling, therefore the *ab initio* calculated force constant matrices are presented below (in units amuTHz^2).

Force constants matrix between the nearest-neighbor (NN) atoms along [010] direction(Γ-X), i.e. between Eu and O atoms:

$$VV_{NN} = \begin{bmatrix} -6507.83 & 0.00 & 0.00 \\ 0.00 & -1955.71 & 0.00 \\ 0.00 & 0.00 & -6507.83 \end{bmatrix}$$

Force constants matrix between next-nearest-neighbors (NNN) along [110] direction(Γ-K-X), i.e. between the two Eu atoms:

$$VV_{NNN} = \begin{bmatrix} -5587.65 & -10287.46 & 0.00 \\ -10287.46 & -5587.65 & 0.00 \\ 0.00 & 0.00 & 3070.31 \end{bmatrix}$$

There are off-diagonal elements in the NNN force constant matrix representing the x and y components. On average the matrix elements are larger than the NN Eu-O elements. Especially, the diagonal (V_{xx} and V_{yy}) and off-diagonal (V_{xy} and V_{yx}) are much larger than

the force constant V_{yy} for Eu-O. The LA phonon modes directly modulate the shortest Eu-Eu distance inducing stronger spin-phonon coupling in the LA modes compared to the TA modes. This explains the broadening in the linewidths of LA modes along Γ-K-X as the magnetic ordering sets in.

Calculations that treat magnon-phonon coupling in a Heisenberg ferromagnet showed that when the NNN force constants are non negligible in magnitude compared to NN force constants, the TA phonons are strongly coupled near the X point along Γ-X direction and LA phonons are strongly coupled along Γ-K-X direction [28]. These calculations are in agreement with our experimental observations.

Check for anharmonicity

The Hellmann-Feynman forces and phonon dispersion relations were calculated assuming two independent sets of displacements with amplitudes $u = 0.03$ Å and $u = 0.06$ Å. Figure S5 demonstrates that the calculated phonon energies vary negligibly with respect to the assumed atomic displacements indicating the absence of significant anharmonicity in the EuO crystal.

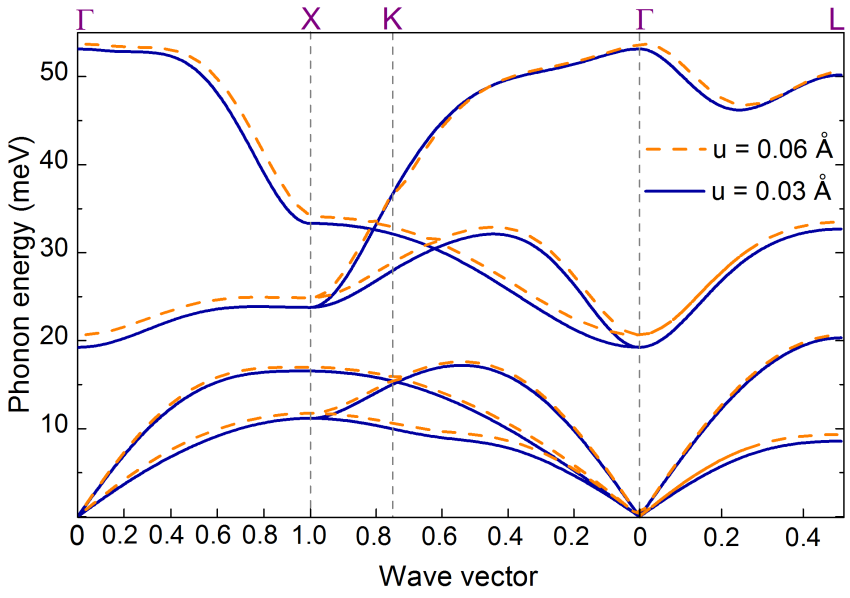

FIG. S5. *Ab initio* calculated phonon dispersion relations of EuO for the indicated atomic displacements.

4. Thermoelastic properties

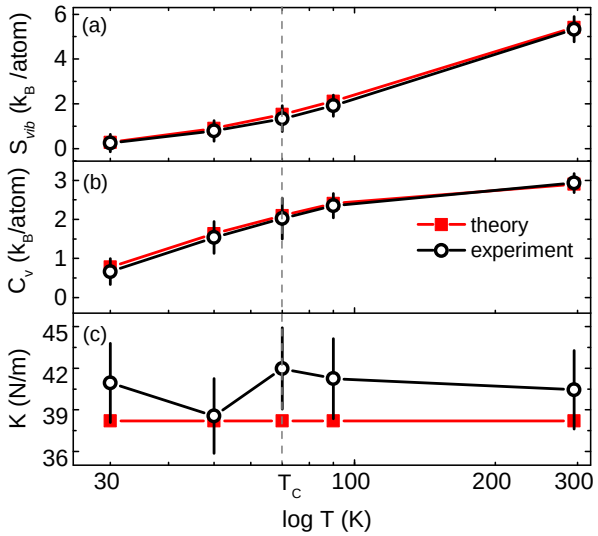

FIG. S6. The experimental and theoretical temperature dependence of the Eu-partial: (a) vibrational entropy S_{vib}, (b) lattice specific heat C_V, and (c) normalized force constant K.

The temperature evolution of selected thermoelastic properties deduced from the *ab initio* calculated and measured Eu-partial phonon DOS of EuO is shown in figure S6. An excellent agreement between theory and experiment for the vibrational entropy S_{vib} and lattice specific heat C_V as well as the absence of any critical phenomenon at the Curie temperature T_C are clearly visible. The normalised force constant K remains temperature independent within the error bars that complies with the established weak anharmonicity in EuO (Fig. S5).

Acknowledgement

I would like to thank everybody who influenced and helped me during my life as a PhD student at the Karlsruhe Institute of Technology.

I am very grateful to Prof. Tilo Baumbach for his support and the opportunity to work in his institute.

I would like to thank Prof. Wulf Wulfhekel for his efforts to read and evaluate my PhD thesis.

I owe my deepest gratitude to Dr. Svetoslav Stankov for giving me an opportunity to work in his Young Investigator Group 'Nanodynamics'. This thesis would not have been possible without his constant guidance and optimism. He found time to patiently introduce me to the field of ultra high vacuum systems and beam line operation. I will always fondly remember our beam times. I also thank him for his efforts and patience to improve this thesis.

I would like to show my greatest appreciation to Dr. Hab. Przemysław Piekarz for performing *ab initio* calculations that are presented in this thesis and his support during the beam time at ID28 of the ESRF. The *ab initio* calculations were crucial to reach the conclusions presented in the thesis.

I thank all my colleagues who work at the UHV Analysis laboratory of ANKA for patiently sharing knowledge and instruments. Many thanks to Dr. Bärbel Krause for her efforts to keep the UHV laboratory in its full glory, which helped me efficiently prepare and characterise my samples. Many thanks to Annette Wießhardt and Hans Gräfe for all kinds of technical support in the chemistry lab and in the UHV Analysis laboratory.

I would like to thank all former and current members of the Nanodynamics group - Shyjumon Ibrahimkutty, Jochen Kalt, Anja Seiler, Evgeny Smekalin, Olga Waller and Honting Wu. It was a pleasure to work with you all. Many thanks to Olga Waller and Anja Seiler for the continuous help with daily chores at the UHV Analysis lab, and of course I will always cherish our happening beam times. I would like to thank Evgeny Smekalin, I will remember our efforts to setup the MOKE spectrometer.

Special thanks to Dr. Shyjumon Ibrahimkutty for his friendship and continuous support in many aspects of my life, especially in the x-ray department and for helping me think in the reciprocal space.

I would like to express my deepest appreciation to my girl friend, Jibi John for her perceptual support, encouragement and patience throughout the last decade of my life.

My heartfelt gratitude to my father (P. Predeep), mother (S. Sheela), and my brother (Ravi Pradip) for all their support and guidance throughout my life.

Erklärung

Hiermit erkläre ich, dass ich die vorliegende Arbeit selbstständig angefertigt und keine anderen als die angegebenen Quellen und Hilfsmittel verwendet habe.

Karlsruhe, 07.11.2016

Ramu Pradip